POLITECNICO DI MILANO

Scuola di Ingegneria Industriale e dell'Informazione

Corso di Laurea in Materials Engineering and Nanotechnology

Monolithic Dye-Sensitized Solar Cells for Building Integrated Photovoltaics

Relatore: Prof. Andrea Li Bassi

Correlatore: Dr. Fabio Di Fonzo

Marco Monti

n. 787392

Anno Accademico 2013-2014

Abstract

One of the most investigated source of energy in the last half century is the conversion of solar energy directly into electricity. At present the silicon-based technology is the most popular on the market and has achieved power conversion efficiencies of about 22-28%. The high cost of production, the required purity of materials and sophisticated technological steps have prompted the researchers to develop solution-processable solar cells. In 1991, Grätzel et O′Regan introduced dye-sensitized solar cell (DSSC), which has then been widely studied for being a potentially easy and economical way to produce a solar energy conversion device. DSSCs are attractive for the variety and the low cost of materials employed for their fabrication. They are inspired by natural photosynthesis, i.e. they transform sunlight in energy using a dye (like chlorophyll). A DSSC consists in a sensitizing dye anchored on a transparent wide-bandgap semiconductor, a counter electrode and an electrolyte between these two. Grätzel's devices achieved a maximum power conversion efficiency of about 7.12%. At now, the maximum power conversion efficiency reached with DSSC is over 13%.

This work aims to fabricate a monolithic DSSC, a particular kind of DSSC in which the two electrodes are deposited on only one substrate instead than on two. The fabrication happened after a characterization of the different deposited components (photo-anode and counter electrode). This device is the starting point to develop a new Building Integrated Photo-Voltaics (BIPV) in the framework of TIFAIN (Tessere integrate di vetro fotovoltaico per applicazioni innovative) project. This project wants to substitute the traditional building components (windows, facades , brise soleils) with a new photovoltaics component that connects a new concentrator at low intensity (patent MI2010A00061A) with the DSSC technology, in order to take advantage of the overall surface to produce energy. Moreover, these devices provide new ideas and opportunity to designers thanks to their variety of shapes and colors.

Estratto

Nella seconda metà del ventesimo secolo, uno dei metodi più studiati per produrre energia è stato la conversione dell'energia solare in elettricità. In questo momento, la tecnologia basata sul silicio è la più popolare sul mercato e ha raggiunto efficienze di conversione del 22-28%.

I sofisticati processi di produzione, che prevedono costi elevati, e la necessità di usare materiali con elevata purezza, ha indirizzato i ricercatori nello sviluppo di nuove soluzioni più convenienti per la produzione di celle solari.

Nel 1991, Grätzel e O'Regan hanno introdotto le dye-sensitized solar cell (DSCC), incontrando un immediato e ottimo riscontro e divenendo oggetto di ampi studi, perché promettono un modo potenzialmente semplice e poco costoso di produrre dispositivi per la conversione dell'energia solare. Il loro funzionamento si ispira alla fotosintesi clorofilliana presente in natura, nel senso che sfruttano un colorante (come la clorofilla) per trasformare la luce solare in energia. Una DSSC è formata da un colorante ancorato su di un semiconduttore trasparente (foto-anodo), un controelettrodo e un elettrolita racchiuso tra i due. Grätzel aveva ottenuto un'efficienza di conversione del 7.12%. In questo momento il record di efficienza è di oltre il 13%.

L'obiettivo di questa tesi è la fabbricazione di un particolare tipo di DSSC, chiamato monolitica, che prevede la presenza dei due elettrodi su di un solo substrato. La fabbricazione del dispositivo è avvenuta dopo la caratterizzazione degli elettrodi. La m-DSSC prodotta è il punto di partenza per sviluppare un nuovo dispositivo da integrare sulle facciate degli edifici (BIPV – Building Integrated Photo-Voltaics) all'interno del progetto TIFAIN (Tessere integrate di vetro fotovoltaico per applicazioni innovative). Questo progetto si ripromette di sostituire le tradizionali componenti degli edifici (finestre, facciate) con un componente fotovoltaico, il quale unisce un nuovo concentratore a bassa intensità con la tecnologia delle DSSC. In questo modo si potrebbe utilizzare l'intera superficie degli edifici per lo sfruttamento dell'energia solare e si produrrebbero anche moduli fotovoltaici, con forme e colori variabili, che offrono nuove possibilità alla creatività e al senso estetico dei progettisti.

Index

Index of Figures

Index of Tables

1 Introduction

In the “Oil & Greenhouse gas Era”, the enviromental challenge is to improve the clean and sustainable energy sources, trying to replace, at least in part, the use of fossil fuels[1-3]. One of the most investigated sources in the last half century is the conversion of solar energy directly into electricity. By now the silicon-based technology is the most popular in the market and has achieved power conversion efficiencies of about 22-28%[4, 5]. The high cost of production, the required purity of materials and the sophisticated technological steps[6] have prompted the researchers to develop solution-processable solar cells[7-10]. In 1991, Grätzel et al.[11] introduced the dye-sensitized solar cell (DSSC), which has then been widely studied for being a potential easy and economical way to produce a solar energy conversion device[12]. DSSCs are attractive for the variety and low cost of materials used to fabricate them. They are inspired by photosynthesis in nature, i.e. they transform sunlight in energy using a dye (like chlorophyll)[13]. A DSSC consists of a sensitizing dye anchored on a transparent wide-bandgap semiconductor. Grätzel’s devices achieved a maximum power conversion efficiency of about 7.12%[11]. At now, the maximum power conversion efficiency reached with DSSC is over 12% [14-16].

This thesis is divided into two parts; the first one is the description of the working principles, of the different kind of devices and of the fabrication methods of semiconductor films. In the second part, we want to explain the results obtained with our devices. This work aims to fabricate a monolithic DSSC, after a characterization of the different deposited components (photo-anode and counter electrode). This device is the first step to develop a new Building Integrated Photo-Voltaics (BIPV) in range of TIFAIN (Tessere integrate di vetro fotovoltaico per applicazioni innovative) project. This project is funded by Regione Lombardia through Fondo Europeo di Sviluppo Regionale (FESR) and by Ministero dell’Istruzione, dell’Università e della Ricerca. There is a partnership between different partners: Industria e Innovazione, Energyglass, Flame Spray, Politecnico di Milano - Dipartimento di Architettura, Ingegneria delle Costruzioni e Ambiente Costruito, Università degli Studi di Milano-Bicocca and Istituto Italiano di Tecnologia (IIT), in particular the branch Center of Nanoscience and Technology (CNST) in Milan. The developmnet of BIPV provides for the possibility to substitute the traditional building components (windows, facades , brise soleils) with a new photovoltaics component that connects a new concentrator at low intensity (patent MI2010A00061A) to the DSSC technology. In this way, it is possible to overcome two problems that affect the silicon photovoltaic development in this field. The first one is the position of photovoltaic panels: being part of the building façade or fenestration, the devices are not positioned horizontally on the roof, but they have to stay in vertical position. In this way, the solar light has a low angle of incidence and most of it is reflected and not absorbed. The new concentrator is designed to enhance the light harvesting efficiency in this particular situation. The use of DSSCs is dictated by a necessity from an aesthetics point of view. Silicon panels are totally black, for this reason they are not suitable to be employed as windows, while DSSCs, which are very versatile from chromatic point of view, can offer a good solution, giving a wide choice of colours. Moreover, they can be fabricated in different shapes and dimensions, at a lower cost respect to silicon technology.

My work is to begin a study of fabrication of monolithic DSSC on the solar concentrator. Monolithic DSSC is a device with a particular structure, it does not present two different electrodes, deposited on two glass substrates, but it is fabricated on a single substrate. In this way, there is a saving in terms of material costs and weight, that in the building field has an important role. I make a characterization of the different parts that compose the device, exluded the electrolyte and the dye because I use commercial materials instead. I fabricate the sample to characterize with three different deposition methods: Pulsed Laser Deposition (PLD), magnetron sputtering and Plasma Assisted Super-Sonic Jet Deposition (PA-SSJD). While for the first two, I use the previous optimization works carried out by other people of the group where I work; PA-SSJD is performed with a new prototype, which I help to develop. I perform a deep analysis of the different specimens (photo-anode, counter electrode) to assess their optical, structural, electrical and morphological characteristics: SEM images, Raman spectroscopy, UV-Vis spectrophotometry and Hall effect measurements. The fabricated m-DSSC is tested by Solar Simulator analysis to characterize its performance via J-V curve.

2 DSSCs for building integrated photovoltaics

During the last decades, with the advent of silicon photovoltaic panels, the attempt to make energetically independent buildings has begun and, promoted in Europe by the Directive 2002/91/EC and with government incentives, is leading to an increasing integration of photovoltaic devices in architectonic field[17, 18]. Usually, silicon panels are installed on roofs for a higher exposure to sunlight. Instead, the new frontier is to produce electric energy using windows. Nowadays, more and more skyscrapers and buildings are built with large windows to take advantage of sunlight during the day. Combining DSSCs and fenestration, it could be possible to produce energy from windows and have transparent or coloured windows. A DSSC consists of a sensitizing dye anchored on a transparent wide-bandgap semiconductor deposited on an FTO glass (photo-anode) and a platinum loaded glass that acts as counter electrode. In DSSCs, basically, the colour is given by the dye and in what region of the visible spectrum it absorbs. Yoon et al. (2011)[19] showed the possibility to create transparent devices with efficiencies of about 6%, but changing the dye-sensitizer, you can obtain cells with different colours, this is an attractive feature for architects and designers to build coloured and energetically self-sufficient buildings[13]. In this field, monolithic DSSCs could play an important role. They are a particular kind of DSSC in which the presence of two different glasses, where the photo-anode and the counter electrode are deposited, is substituted fabricating the device on a single substrate that contains both electrodes. Thanks to the absence of the second counter electrode glass, it is possible to fabricate, saving material costs and device weight, coloured windows with a lot of devices deposited on, connected in series to obtain a sufficiently high voltage to supply an inverter. It is done to convert the direct current (DC) from the photovoltaic devices in alternating current (AC) thus connecting the "photovoltaic windows" to the grid and increasing power output[20]. A drawback to overcome is that, at now, the counter electrode is in carbon, which makes the entire device, covering the sensitizer, black. To solve this problem, the idea is to deposit a transparent porous conductive film of ITO instead of the carbon, but it should be porous, and this fact could affect negatively the conductance properties.

Another improvement for the building integrate photovoltaic systems (BIPV), is the device deposition on optical concentrator at low intensity. In this way, the problem of low intensity of incident light, due to the vertical position of the BIPVs, is overcame with a better light harvesting and management but it should be porous, and this fact could affect negatively the conductance properties.

2.1 Working principles

The typical DSSC structure is represented in Fig. 2.1-a. There are two transparent conducting oxide (TCO) electrodes, on the first one a dye-sensitized nano-crystalline semiconductor film is deposited. The second electrode is loaded with Pt. Between the two electrodes there is an electrolyte containing a Redox couple between the electrodes. [21]

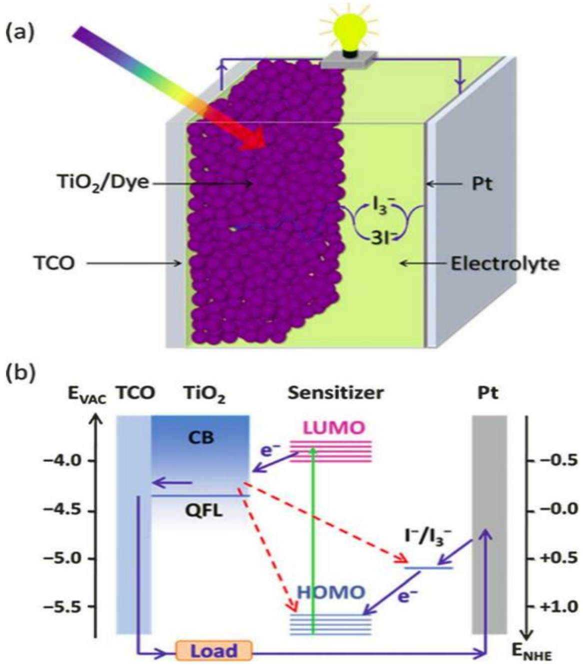

Figure 0.1 (a) Schematic structure and (b) main processes in DSSC

In Fig.1-b, the main processes which happen in a DSSC are schematised. The dye molecules, when illuminated, undergo transition from their ground state (*highest occupied molecular orbital or HOMO*) to an excited one (*lower occupied molecular orbital or LUMO*). The photo-excited dye molecules that are in LUMO state have an unbalance in the charge distribution, from a delocalised charge distribution to a localized one close to the anchoring group; this displacement leads to the formation of an electron-hole couple pair, called exciton.[22] Between electrons (part of the molecule where the charge is localized) and electron-holes (the “other side” of the molecule) there is a Coulomb force. The greater is the distance between the two parts, the less attractive is the force between them. If the potential difference between the Conduction Band (CB) of the semiconductor film and the LUMO level of the dye is lower than the Exciton Binding Energy (EBE), it drives the splitting of the exciton into free charges and the injection of electrons in the metal oxide film.[23-25] The electrons injected in the semiconductor film are transported through this one and towards the TCO anode to an external circuit. This process leaves an electron vacancy in the dye. In order to bring the system back to its early stage, the electrolyte regenerates the dye molecules passing to the oxidized state. Electrons necessary to reduce the oxidized electrolyte are taken from the anode to the cathode by the external circuit.

Current-voltage characteristic is a way to describe performances of an electronic device. It is the representation, in a graph, of the current that flows through the device and the corresponding voltage across it. Depending on the characteristic shape, it is possible to identify the type of device. Current-Voltage characteristic of DSSC, and in general of all photovoltaic devices, is that one of an illuminated diode. (Fig.2.2)

The maximum voltage of the device (also called open circuit voltage or V_{OC}) is the potential difference between the quasi-Fermi level of the semiconductor and the electrolyte redox potential of the electrolyte. This is true for the ideal case and for an n-type semiconductor, the quasi-Fermi level can be approximated with the CB, in particular when electrons are injected. Short circuit current (or I_{SC}) is the current for zero applied reverse voltage and under illumination condition. Another parameter to be taken into account is the fill factor (or FF), which is the ratio of the maximum power output P_M (given by the product between I_M and V_M) to the production of J_{SC} and V_{OC}.

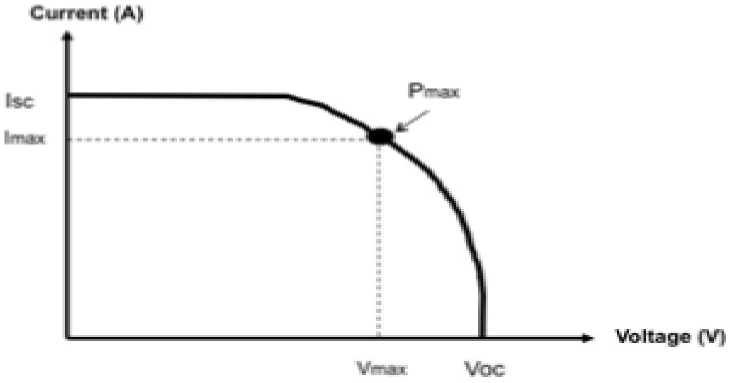

Figure 0.2 Current-Voltage characteristic of a common photovoltaic device

FF is the parameter that represents the quality of the cell. The higher its value, the higher the quality of the cell and higher the conversion efficiency.[21]

The general formula of power conversion efficiency (PCE) is:

$$\eta = \frac{P_{out}}{P_{in}} = \frac{I_{SC} V_{OC} FF}{P_{IN} A_{cell}} \qquad [1]$$

Where P_{in} is the namely incident light-power that illuminated the area of A_{cell}. In turn the power output formula depends on the power input:

$$P_{out} = P_{in} \cdot \eta_{abs} \cdot \eta_{inj} \cdot \eta_{col}$$

Where η_{abs} is the number of photons absorbed over the incident photons (or light absorbance); η_{inj} is the injection efficiency, i.e. the number of electrons injected from the dye into the semiconductor over the photogenerated charges; η_{col} is the collection efficiency, being the efficiency of the injected electrons to be collected by the anode. So the [1] becomes:

$$PCE = \eta = \frac{P_{out}}{P_{in}} = \frac{P_{in} \cdot \eta_{abs} \cdot \eta_{inj} \cdot \eta_{col}}{P_{in}} = \eta_{abs} \cdot \eta_{inj} \cdot \eta_{col}$$

In addition to the described processes, there are other competitive and detrimental processes that lead to loss of efficient energy conversion. Fundamentally, they are processes of charge recombination.[26, 27] Fig.2-b[21] and Fig.2.3 show the parasitic processes with the timescale of each event.

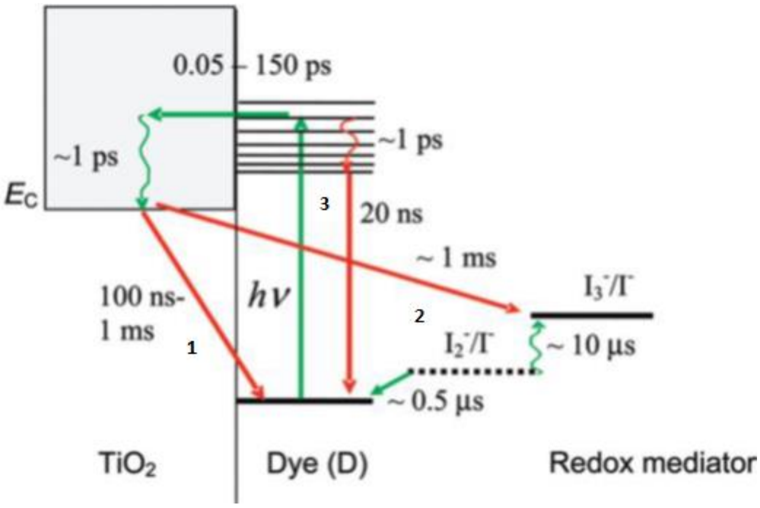

Figure 0.3 Timescale of the main photogeneration and recombination processes in DSSC

In green there are the above described processes, in red there are the detrimental ones:

1. Electrons from the CB of the semiconductor back to the ground state of the dye
2. Electrons From the CB of the semiconductor back to the electrolyte
3. Electrons in the dye LUMO recombine with the vacancy left in the dye itself

Table 2.1 Values of efficiency, J_{SC}, V_{OC} and FF for different kinds of Photovoltaic Cells

Device	**Efficiency [%]**	**J_{SC} [mA/cm^2]**	**V_{OC} [V]**	**FF [%]**
Si (crystalline)	25.0 ± 0.5	42.7	0.706	82.8
GaAs (thin film)	28.8 ± 0.9	29.68	1.122	86.5
Si (amorphous)	10.1 ± 0.3	16.75	0.886	67.8
Organic thin film	10.7 ± 0.3	17.75	0.872	68.9
Dye Sensitized	11.9 ± 0.4	22.47	0.744	71.2

One of the main goal of scientists is to improve more and more these efficiencies, in addition to reduce the row material costs and to increase the stability. To do this, we must work on the key components of DSSCs to optimize them and create a synergy between the different parts to obtain the highest possible PCE: increase the light harvesting by the dye and its electron generation, make a metal oxide film that allows a nearly 100% efficient electron transport, use an electrolyte that could rapidly regenerate the dye, enhance the electrical and catalytic performances of the counter electrode. We discuss about these four fundamental components in the next paragraph.

2.2 Device structure

As we have seen above, the key components of a DSSC are the sensitizer, the electrolyte, the semiconductor and the counter electrode. In this paragraph, we will discuss them in detail.

2.2.1 Photo-anode semiconductor

The photo-anode is a porous large bandgap semiconductor (such as titanium dioxide or zinc oxide) that allows dye chemisorption and electrolyte percolation to favour the formation of the interface between the donor and the acceptor material. To achieve these objectives the photo-anode should have some peculiar characteristics that we will see in this paragraph in which we will talk about TiO_2 based photo-anodes.

2.2.1.1 Surface Properties

Thickness, porosity and Roughness Factor (RF) are three of the main parameters to evaluate a photo-anode and they affect DSSC efficiency. A thinner photo-anode has lower resistance in charge transport process from the sensitizer to TCO than a thicker one, but it could be too thin to assure a good light management. Porosity is the void fraction of a material. It is fundamental to knowing and control the photo-anode porosity because it sets the amount of sensitizer and electrolyte and their distribution into the voids of TiO_2 film. In fact, porous size is a main parameter for the percolation of electrolyte and sensitizer. If pores are too small or not connected, sensitizer and electrolyte cannot reach all the available surface or there could be problems of mass transport, with a consequent efficiency loss.[28] The porosity affects, indirectly, also the light path length and the electron linear pathway. Roughness factor is the ratio between the total material surface and the projected geometrical surface. It is an important parameter because RF represents the specific surface area available for chemisorption of dye and electronic reaction. To enhance PCE, it is necessary to engineer these three parameters and achieve an optimum that could change depending on the morphology, as we will explain in Par. 2.2.1.4.

2.2.1.2 Electronic Properties

As we said above, photo-anode is a semiconductor film that should transport the injected electrons from dye to TCO (Fig.2.4[5]).

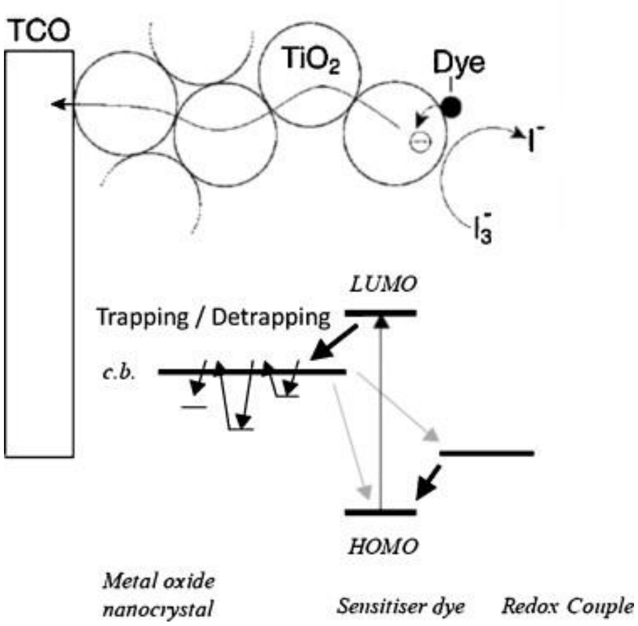

Figure 0.4 Electron transport in a nanoparticle film along a linear pathway

For this reason, one of the main characteristic is the difference between the dye LUMO level and the conduction band of the semiconductor. The conduction band should be more positive than LUMO level, in this way there is a drag force between them that allows the charge passage, but this difference should not be so high to avoid the possible recombination of electrons in LUMO with vacancies left in the electrolyte. Moreover, another fundamental feature for a photo-anode is the transport of injected charge from the dye to the TCO and the external circuit. The electron transport efficiency is affected by the homogenous particle interconnection, it would be better that electrons go through a linear pathway from the sensitizer/photo-anode interface to photo-anode/TCO interface, rather than a winding one or multiple hops from a nanoparticle to another one that could promote recombination processes.

Titanium dioxide (or commonly titania) is a transition metal oxide that has, in addition to the amorphous phase, two main allotropic phases: anatase and rutile. During the last five decades, titania bulk properties have been widely studied and TiO_2 is largely used in a lot of fields: paints, cosmetics, electronic devices, sensors, photo-anodes. In addition to the different crystalline structures, the three phases differ in their bandgap, which is a main feature in the charge injection process from the dye to the semiconductor film. Anatase has a higher optical band-gap than rutile, 3.2 eV and 3.0 eV respectively[29]; so the conduction band of anatase has a slightly lower potential value than the LUMO level of the sensitizer, leading a better electron injection from dye into the photo-anode.[30] During the report, we will talk about the different morphologies (Par. 2.2.1.4) and deposition methods (Par.2.2.1.5) that could be used to fabricate titania devices and to engineer its electronic characteristics.

2.2.1.3 Optical Properties

The main optical property for a photo-anode is the transmittance of visible light. In fact, if photo-anode absorbed visible light, the sensitizer could not work over a wide light spectrum with an evident efficiency loss. TiO_2 is perfect in this case because it absorbs in UV range.

To enhance the light harvesting by the sensitizer and then the incident photon-to-current efficiency (IPCE), the light management allows optimizing incident light harvesting on the photo-anode exploiting scattering given by nanoparticles of which TiO_2 film is made. The theory behind the scattering phenomenon is based on the measurement of the cross section. For particles much smaller than wavelength, the intensity of scattered light is determined by the Rayleigh low and is directly proportional to the sixth power of the particle diameter (approximated to a sphere) and inversely proportional to the fourth power of the wavelength. In this model, light is scattered in a symmetric way, so the light scattered forward has the same intensity of that backscattered. This is true only for particles much smaller than wavelength, otherwise there is a more complex solution given by the Mie theory. In this case the scattering phenomenon does not follow a symmetric trend, but the forward scattered light has a higher intensity than that backscattered (Fig.2.5)[31].

Figure 0.5 Schematic Rayleigh and Mie scattering processes.

In literature, there are lot of examples of how to implement light trapping and most of them are based on morphology engineering. We can see an example in Fig.2.6, Zhang et al. (2013)[21] used large diffusive particles into the crystalline TiO_2 photo-anode increasing the optical path length of the light of about 10%. In the Par.2.2.1.4, we will show different possible morphologies for TiO_2 photo-anodes, from standard nanocrystalline particles to quasi-1D nanostructures that meet the need to have a quasi-linear pathway for electrons conduction and a good light management thanks to the scattering.

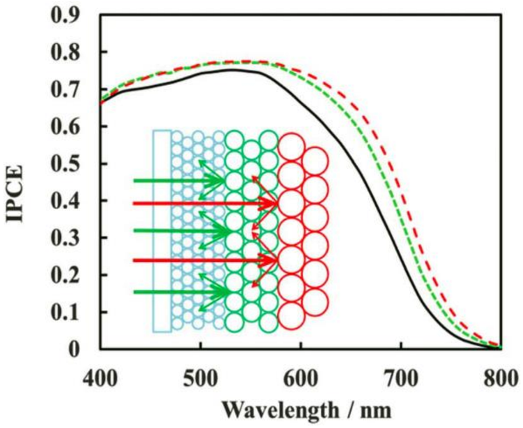

Figure 0.6 IPCE spectra of N719 sensitized solar cells with no light scattering layer (black solid line), a scattering layer with smaller particles size (green short dashed line), and a scattering layer with larger particles (red dashed line). Inset: schematic pictures of the light-scattering effect with scattering centres or scattering layers.

2.2.1.4 Morphology

In Par.2.2.1.5, we will see different standard methods to produce mesoporous films, but now we concentrate on the different morphologies, which can be obtained. When Grätzel et al. in 1991 introduced DSSC technology [11], they used a colloidal solution to deposit TiO_2 photo-anodes. The result was a porous film composed by sintered nanoparticles (Fig.2.7). They controlled the RF of the film by the size of the particles and thickness of the film, achieving an optimum

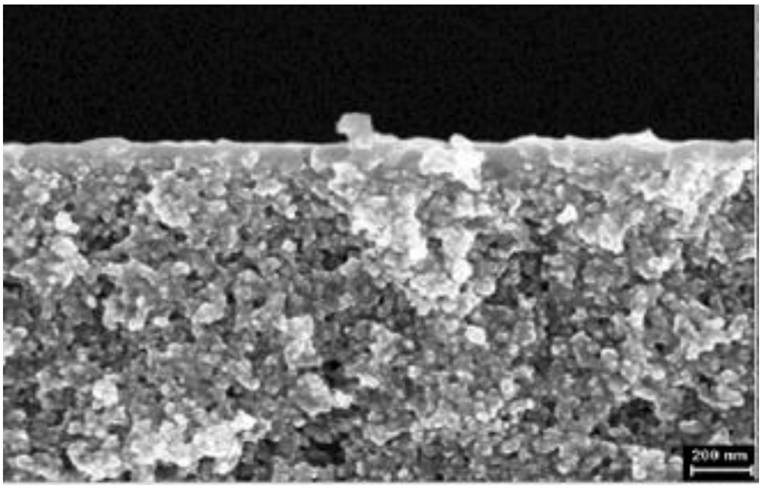

Figure 0.7 SEM image of standard nanocrystalline titanium dioxide

with a thickness of about 10 µm and particles with an average size of 15 nm. Since the first cause of charge recombination within the mesoporous layer is due to a phenomenon of trapping/detrapping at the nanoparticle interconnection[32], the research began to leave the random nanoparticles structure to follow and develop elongated structures, which offer a preferential pathway for electron transport, reducing hops between nanoparticles. These elongated structures can be divided in 1D structures (nanotubes, nanowire and nanorods) and quasi-1D strucutures (branched nanowires, dendritic nanowires, nanoflowers and forest-like architecture). 3D structures, as spherical oxide aggregate nanostructures, are used to enhance the light harvesting.[5]

Nanotubes, Nanowires and Nanorods

Since the discovery of carbon nanotube about three decades ago[33], this particular 1D structure has been studied a lot for its multiple properties. In fabrication of DSSC photo-anodes with TiO_2 nanotubes, the high RF of the nanostructures is exploited with its channels that allow, if they have a suitable diameter (from about 20 nm to hundreds of nm), chemisorption of dye and infiltration of electrolyte. To further increase the surface area, nanotube structure is engineered leading to the fabrication of bamboo-like array (Fig.2.8-b,d)[34, 35].

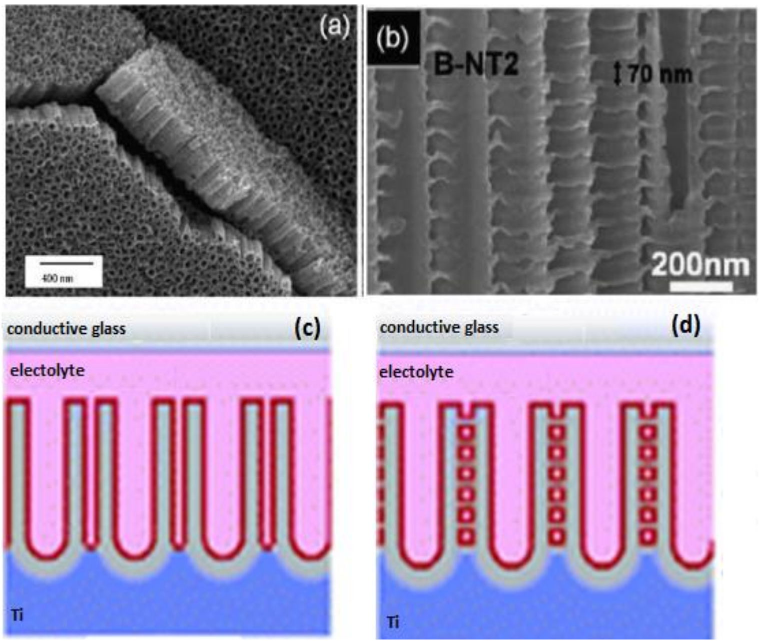

Figure 0.8 SEM images of a) nanotubes of TiO2 and b) nanotubes bamboo-like. Schematic representation of c) nanotubes and d)

Bamboo-like nanotubes have some interconnections between the different channels and they allow to increase the RF and then the overall efficiency.[34]

Nanowires and nanorods (Fig.2.9)[5, 10] have analogous characteristics to high RF and preferential electrons pathway as nanotubes, but instead having channels where

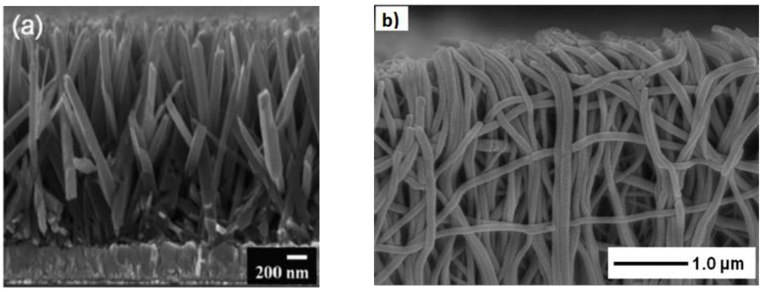

Figure 0.9 SEM images of a) aligned nanorods and b) vertical nanowires

sensitizer and electrolyte can diffuse, they are on the external surfaces of nanowires and nanorods. [36, 37]

3D structures

Kim et al. (2009)[38] showed a way to enhance the light management in TiO_2 photo-anode using spherical nanostructures. As we can see in Fig.2.10[38], they are spherical nanoclusters made uo of smaller nanoparticles. In this way incident light is scattered both by nanoclusters both by single nanoparticles that make up the spherical compounds, increasing of about 10% the quantum efficiency at 550 nm wavelength and in the longer-wavelength region respect to standard nanocrystalline films.[39] The drawback of this morphology would be the presence of a lot of small surfaces among different nanoparticles and among nanoclusters, this fact decreases drastically the electron transport through the photo-anode due to many hops and linear pathway lack.

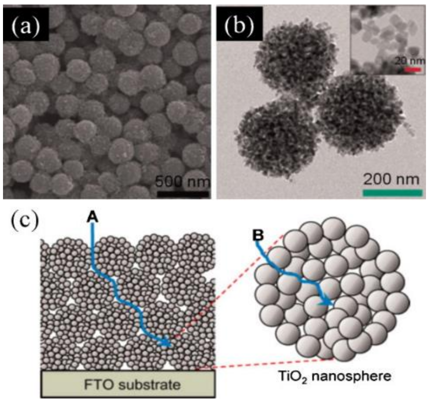

Figure 0.10 (a) SEM and (b) TEM images of nanoporous TiO2 spheres, and (c) schematic diagram showing the electrolyte diffusion through the external (A) and internal (B) pores in the film made of nanoporous TiO2 spheres.

Nanotrees

Nanotrees are part of the so-called quasi-one dimensional hierarchical structures. They mix high RF, to increase active area for chemisorption of sensitizer and to charge photogeneration, and few particle/particle surfaces with linear pathways for electron transport, typically of 1D structures, with a rough surface that enhances the light harvesting. It is possible to control densities, porosities and branching, depending on method a parameters of deposition, affecting optical, surface and electronic properties, so it is important to achieve an optimum among these three important parameters. About this, Di Fonzo et al. (2010) have shown interesting results.[40]

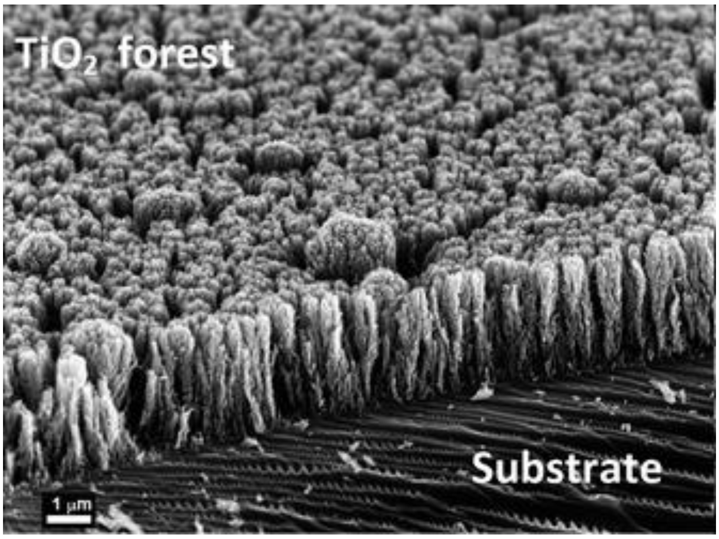

Figure 0.11 SEM image of TiO2 nanotrees deposited by PLD

In the next paragraph we will show some different deposition methods to fabricate photo-anode with the described morphologies.

2.2.1.5 Standard Deposition Processing

In Par.2.2.1.4, we talked about the different possible morphologies of photo-anodes. To fabricate photo-anodes with one of the described morphologies, there are many deposition processes, which we will describe in this chapter. In order to make a device competitive, the deposition method of the photo-anode should combine the possibility to deposit desired morphology and thickness with a low cost of the process, a good reproducibility, a large deposition area and a low time of deposition. Pulsed Laser Deposition (PLD), Sputtering and Plasma Assisted-Super Sonic Jet Deposition (PA-SSJD) will be described in the part of methods (Par.3.1) because are the deposition technique that I used during my work.

Doctor Blade

Doctor Blade is a process taken from the rotogravure. A flexible blade removes the excess of ink during the print of an imagine from an engraved die.[41] In the DSSCs fabrication, ink is replaced by a titania paste, which is a blend of titania flakes and nanoparticles (or also nanotubes)[42] mixed with a solvent to avoid the big aggregates and obtain a homogenous paste. This blend is spread on the TCO glass and you can act on pressure of the blade on the ink film and on its driving velocity, in order to obtain the desired thickness on a large area. The advantages of this technique are the simplicity of the process and the commercial availability of materials. The drawback is the low homogeneity of the surface caused by particles agglomerates. Moreover you can obtain a porous film with a net of titania nanoparticles but it is impossible to obtain a forest-like architecture and a preferential pathways that allow a good electron transport.[43]

Hydrothermal Growth

Hydrothermal technique consists in a crystal growth method borrowed by the quartz crystals deposition.[44] It is based on the use of the autoclave, a machinery that allows conducting reaction at high temperature and high pressure. Pressure and temperature are the main parameters for the hydrothermal growth: an aqueous solution of salts of the material to be deposited is heated and kept at high pressure leading the deposition of big crystals. In this way it is possible to control thickness and morphology of the deposited film.[37] This technique is used to obtain pastes that then will be deposited with different methods (doctor blade, ink jet…)[45, 46], but the disadvantage is the slowness of the process.[37]

Anodization

Anodization (or anodic oxidation) is a top-down fabrication process. It is one of the most common fabrication technique of TiO_2 films, also thanks to its easiness and low cost.[47] The fundamental principle upon this method is based is the oxidation of the anodizing metal. In the case of titania, a film of Ti is deposited on the substrate, then with an electrolyte and giving current, a passivation process happens and pure titanium becomes TiO_2. This phenomenon is well explained by the next formulas that show the formation of an oxide layer at the anode:

$$2Ti \rightarrow 2Ti^{4+} + 8e^-$$

$$Ti^{4+} + 4OH^- \rightarrow Ti(OH)_4$$

$$Ti^{4+} + 2O^{2-} \rightarrow TiO_2$$

$$Ti(OH)_4 \rightarrow TiO_2 + 2H_2O$$

Lin et al. (2013)[48] show a method to obtain porous TiO_2 films in a really exhaustively way, but also nanotube morphologies are possible to deposit.[49] We have already said that this technique is simple and easy for fabrication, has low cost and is suitable to deposit on large areas. Efficiencies achieved by devices fabricated with this method are about 6%.[47, 49] A possible drawback is the dangerous nature of components of the electrolyte (Par.2.2.4), in fact in 1999, Zwilling et al.[50] fabricated a Ti film using chromic acid and hydrofluoric acid, which are harmful to health. In the last decade, many efforts have been done trying to use electrolyte without not-fluorinated electrolytes. Recently a method to give up fluorinated electrolytes has been studied by Sreekantan et al. (2010)[51] using organic baths. In this way, they still obtain long nanotubes in times comparable with that typical of acid electrolytes, but they are not harmful to health and, moreover, it is possible to fabricate TiO_2 nanostructured film on a lot of new substrate that were not suitable for previous acid solutions. In this way, it is possible to overcome the problem to fabricate nanotube arrays on a suitable substrate (typically alumina) and then transport it on a conductive glass. This is also a method to fabricate and crystallize by annealing TiO_2 nanotubes films on organic material that can not achieve 500°C necessary for annealing.[52]

2.2.2 Counter Electrode

The counter electrode, which works as cathode, has the task to take electrons from the external circuit and to provide them for the triiodide reduction to iodide. The main features should be an excellent electrochemical and catalytic efficiency, a low internal resistance and raw material cost.[53] At the moment platinum ensures the catalytic efficiency and the low internal resistance, but its cost is very high, so in the last years other solutions have been in evaluated, i.e. carbon films and activated carbons.

The reaction mechanism of triiodide production is the following[54]:

$$(a)\ I^- + Pt \rightleftarrows I^-(Pt)$$

$$(b)\ I^-(Pt) \rightleftarrows I(Pt) + e^-$$

$$(c)\ I(Pt) + I(Pt) \rightleftarrows I_2 + 2\mathrm{Pt}$$

$$(d)\ I_2 + I^- \rightleftarrows I_3^-$$

I^- is the result of dye reduction by triiodide and is in concentration ration 9:1 respect to the I_3^-. The (a) step is the adsorption of iodide on platinum. (b) is the oxidation of iodide. (c) and (d) are respectively the I_2 and I_3^- production. Among these steps, the rate-determining step is represented by the iodide oxidation, which is the slowest process.

The other parameters that affect counter electrode efficiency are the charge-transfer resistance of the platinum electrode/electrolyte interface and the diffusion constant of triiodide in the electrolyte. As we said before, iodide is in higher concentration in the solution, so the diffusion time of triiodide from counter electrode to the dye surface is crucial, but this is an electrolyte characteristic. Instead, regarding the charge-transfer resistance, it is affected by the parameters of the Pt film. The thickness of the layer is the main parameter; thicker is the film, higher will be the quantities of Pt present and lower is the charge-transfer resistance. But, as said before, one of the main features is the row material cost, which, using high quantity of Pt, increases very much. Moreover, the high Pt presence does not always give good results. For example, the catalytic power is affected not only by the quantity but also by the free Pt surface. In fact, the reactions occur at the surface of the Pt particles, if the film is low porous and thick, only the external Pt particles contribute in the reaction, while the underlying one give only the contribution in electrons transport. In this context, the optimization of porosity and morphology could give good result in increasing the catalytic power and decreasing the charge-transfer resistance. Hauch et al. (2001)[54] exploit a columnar structure to match the increase in thickness with an enhancing in surface area available for the reduction reaction. Platinum film should be perfectly adherent to the substrate. If some Pt particles come off, they could be adsorbed at TiO_2 surface and create a short circuit, with loss of photogenerated current. To avoid this problem, it is important the deposition process.

To overcome the cost issue, Li et al. (2009)[55] suggest to use carbon black with a low load of platinum. The results are encouraging, they fabricate devices with efficiency of 6.72%, while, with only Pt counter electrode, the efficiency is 6.63%. Their idea is to exploit the catalytic power of carbon, which is usually located on the edge of carbon crystal sheet. Carbon black is low crystalline and has a great amount of edges, so it is more suitable and efficient in catalytic activity than carbon materials as graphite and nanotubes that have a high structure orientation.

2.2.3 Sensitizer

The sensitizer is the hub that generates the photocurrent in the DSSC. To develop highly efficient DSSCs, the molecular engineering of the dye sensitizers is fundamental and they must fulfil the following characteristics:[56]

1. The sensitizer should have the widest absorption spectrum possible in the visible/NIR (Near infrared) region.
2. The sensitizer should present strong anchoring groups (such as –COOH, -SO_3H etc.) for an optimum and hard binding onto the semiconductor film. This parameter affects the charge injection in the photo-anode.
3. The sensitizer should have a LUMO level more negative than the CB of the semiconductor to allow the charge injection.
4. The lifetime of the excited state should be in the order of femtoseconds. As we have seen above in Fig.3, it would be two orders of magnitude faster than the recombination process.
5. The sensitizer should have a HOMO level more positive than the redox potential of the electrolyte to be regenerated after charge injection.
6. The sensitizer should be electrochemically, photo-chemically and thermally stable for longer periods.
7. The sensitizer should be low cost, abundant, soluble in a variety of solvents and not hazardous.

There are three main categories of sensitizers: metal complexes (Ruthenium, Platinum, etc.), organic dyes and tetrapyrrolic dyes (such as Porphyrin).

Metal Complex Sensitizer

These dye sensitizers are organometallic compounds, i.e. a molecule that have a central metallic atom (in this case typically Ruthenium) and some organic ligands. We can see two examples in Fig.2.12.

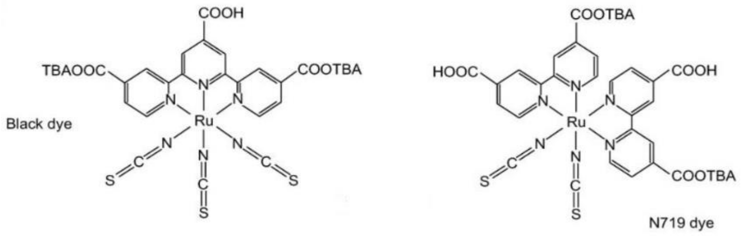

Figure 0.12 Molecular structure of N749 (left) and N719 (right). Two examples of Ruthenium based dyes

Metal to Ligand Charge Transfer (MLCT) is main working principle: the electrons in the metal are excited in the π* orbital of the ligand (e.g. CN or CO), the presence of the –COOH group and the semiconductor then make possible the charge injection. In Fig.2.13, we can see the distribution of LUMO and HOMO for the Black dye. HOMO level is mainly localized on the Ru and electron donating ligands, while LUMO level is mainly distributed on the polypyridyl ligands, where there are the groups anchored on the metal oxide film.This promotes an efficient electron injection into the semiconductor film via chemical bonding and the regeneration of oxidized dyes.[21]

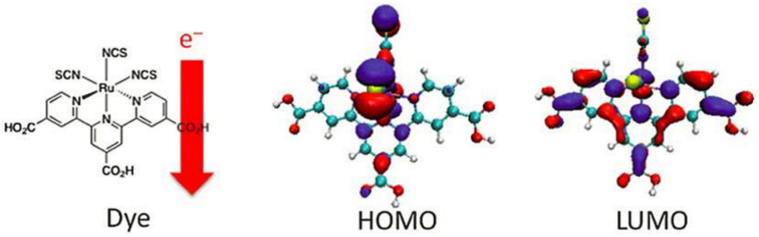

Figure 0.13 Electron flow and the HOMO and LUMO distributions of black dye (N749)

To engineer this kind of sensitizer, there are studies that try to improve the intrinsically light extinction coefficient, i.e. a measurement of how a chemical specie absorbs light at a given wavelength. For example, N719 shows prominent absorption peaks at the UV region and the visible-NIR region. In this way, there is missed good light management in visible region.[21] To increase the visible light absorption, the expansion of π-conjunction of polypyridyl ligand results in a bathochromic shift of the absorption band.[57, 58] Changing the central metal atom, absorption property changes drastically, an example is the use of Os based dyes by Wu et al. (2012)[59].

In Fig.2.14, we can see the absorption difference between Ru-based dye (N719) and Os-based dyes (TF-5, TF-51, TF-52).

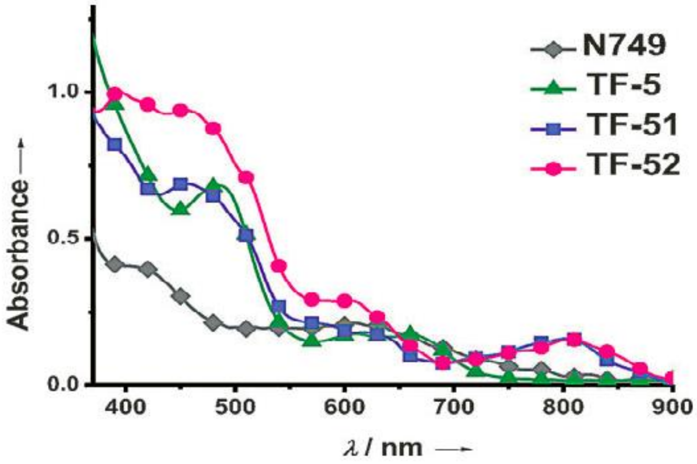

Figure 0.14 Absorption spectra of TF-5, TF-51, TF-52 and N749

The other challenge is to make Ru-based dyes more resistant to the environment.[35] Thiocyanate (NCS) is one of the ligands of N719, but is easily eliminated or exchanged for solvent, redox mediator and additives in the electrolyte under illuminated condition.[21] Bessho et al. (2009)[60] use "NCS-free" Ru dye, achieving an efficiency of about 10.1%.

Using Ru based sensitizer, the devices show PCE above 10%, but the main drawback is the high cost of noble metals required.

Organic Dyes

Respect to metal complex sensitizers, organic dyes have a different photophysics. These sensitizers are composed by three main parts, as we can see in Fig.2.15, a donor, a π-spacer and an acceptor, which also work as anchor to TiO_2. The presence of these parts, when the device is iluminated, allows an intramolecular charge separation, with electrons that pass in TiO_2 substrates through the acceptor part.

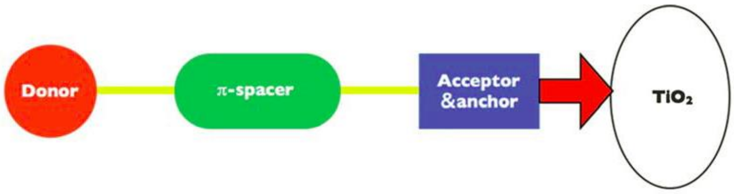

Figure 0.15 Schematic drawing of D-p-A type organic dye

The main advantage of the metal-free organic dyes is, exactly, the absence of the central noble metal in the molecule. This leads to a reduction in cost, because organic molecules are surely cheaper and easier processable than the metal complexes. Despite these advantages, they present some drawbacks: narrow absorption spectra, shorter exciton lifetime, aggregation induced self-quenching.[61] The organic molecules used for these sensitizers are triarylamines, coumarins, squaraines, carbazoles and indoline. The use of these sensitizers for DSSCs has leads to reach PCE up to 9.8%.[46]

Tetrapyrrolic Dyes

This is the most promising sensitizer category because they could overcome limited light absorption in the NIR zone of metal complex dyes and low stability of organic dyes.[62] The main categories among tetrapyrrolic molecules are porphyrins and phthalocyanines. We can see an example in Fig.2.16.[63]

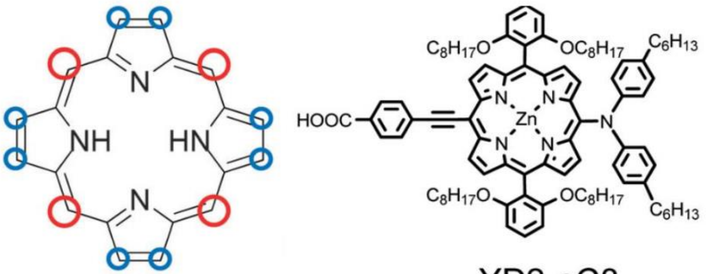

YD2-oC8

Figure 0.16 (left) Typical porphyrin dye core structure, (right) the best performing dye holding PCE record

The figure on the left shows the sites available for the attachment of anti-aggregation (such as 3,5-di-tertbutylphenyl groups) in blue and anchoring group (such as –COOH) in red. The main characteristic of porphyrins is the optical response, in fact they show two main absorption peaks (Fig.2.17): the first one is in the 400-450 nm spectral region and the second in the 550-700nm spectral region. To overcome this gap between the two absorption regions, blend of dyes have been engineered and employed, with encourage results in terms of IPCE and PCE.[15, 16]

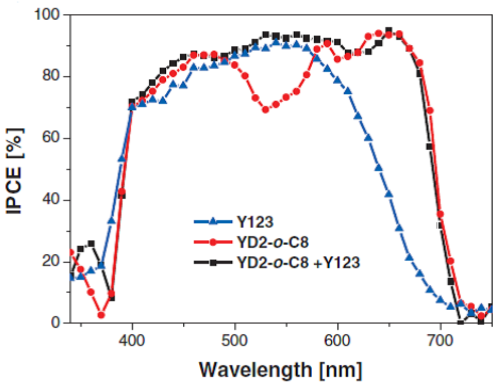

Figure 0.17 the IPCE spectra (number of charges collected per incident photon) of the YD2-o-C8 porphyrin (in black the spectrum of the same porphyrin blended with Y123 dye)

2.2.4 Electrolyte

The electrolyte has the fundamental task of regenerating the oxidized dye by donating a negative charge once the sensitizer has injected an electron into the semiconductor. The timescale of this process should be as fast as possible and have the same order of magnitude of the electron injection process (from tens of picoseconds to hundreds of femtoseconds).[27] Other characteristics that a hole conductor should fulfil are a low absorption in visible spectra to avoid parasitic absorption, a big difference between the dyes LUMO and the redox potential to enhance open circuit voltage, a low corrosive power and volatility.

The most common electrolytes are based on iodide/triiodide redox couple and their use could be achieved a PCE over 11%.[64, 65] The reduction reaction of the oxidized dye is the following two-electron reaction:

$$I_3^- + 2e^- = 3I^-$$

There are several steps to get to the previous overall formula. When the sunlight photoexcites the sensitizer, there is the splitting of the exciton and the oxidize of the dye. Than the oxidized dye creates an unstable bonding with an iodine ion. Another I^- ion from the electrolyte break this weak bond state and forms an unstable I_2^- that, in the end, thanks to another iodine ion, forms triiodide[66]:

$$D^* \rightarrow D^+ + e^-(TiO_2)$$

$$D^+ + I^- \rightarrow (D \cdots I)$$

$$(D \cdots I) + I^- \rightarrow D + I_2^-$$

$$2I_2^- \rightarrow I_3^- + I^-$$

The needed electrons to the dye regeneration should be provided by the counter electrode with the external circuit that comes from the anode. A low load of a catalytic material (usually Pt) on the counter electrode is used to facilitate and accelerate the reactions.

As we said above, a crucial feature for an electrolyte in DSSCs is the difference between the dye LUMO (1.1V for typical Ru based dyes) and the redox potential of the electrolyte (0.35V c.a. for Iodide based electrolyte), because this is the potential used to drive the forward reaction of the whole device. It is also called open circuit potential, as we said in Par2.1; in the case of iodide/triiodide based electrolyte is about

0.75V. This value is lower respect to other Photovoltaic Device (Tab.1), besides the two-electron reaction is an intrinsically slow process and the iodide-based electrolytes are corrosive on the TCO. To overcome these problems, in the last years, there has been an increasing study for iodide-free electrolytes.[67, 68]

In this way, the most promising iodide-free hole conductors are cobalt-based ones. Nusbaumer et al. in 2001[69] introduced the first cobalt based electrolytes; in 2014, Mathew et al.[16]achieved the actual PCE record of 13% for DSSCs. These electrolytes are based on the Co^{2+}/Co^{3+} redox shuttle. As we have seen above, the typical potential difference between the LUMO level of the Ru-based dye and the iodine based electrolyte is about 0.7V, instead the redox shuttle in a cobalt based electrolyte has a more positive reaction driving potential (0.5-1V) (Fig.2.18), so the V_{OC} could achieve value of about 1V, leading the achievement of better PCE.

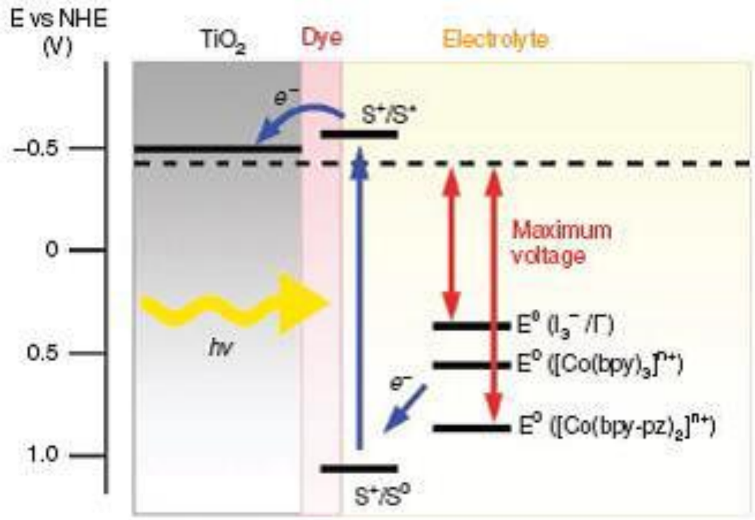

Figure 0.19 Redox potential of different Cobalt based electrolytes

Moreover, in iodide electrolytes, during the regeneration process, there is the formation of intermediate species (I^{2-}) that are corrosive towards the dye and metal such as Ag, Au, Cu that, otherwise, could be used as counter electrodes.[70]

In general, you can divide DSSCs in three subgroups: liquids, solids and quasi-solids, depending on the electrolyte used.

2.2.4.1 Liquid

Most of the above exposed electrolytes are in liquid state at room temperature, so devices fabricated with these electrolytes are called liquid DSSCc and are the most common in literature. Efficiency record of 13% is achieved using a liquid Cu-based electrolyte.[16] Liquid electrolytes have a lot of properties that have made common their availment in DSSC fabrication. The most important is the possibility to percolate easily into the pores of mesoporous photo-anode, taking advantage of the big contact surface area where sensitizer is regenerated. Despite the many properties this family of electrolytes has there are some drawbacks though, which brought to the research of different materials. The main disadvantage is the corrosion of the photo-anode in contact with electrolytes, above all for iodide-based ones, but also leakage and evaporation of electrolyte and photodegradation that occurs with redox cycles are drawbacks that must be overcome to improve this family.[67, 71]

2.2.4.2 Solid

To overcome the drawbacks of liquid DSSCs, a new type of DSSCs was engineered which is characterized by a conducting polymer as hole transporting material (HTM) instead of the liquid electrolyte. These devices are called solid-state DSSCs (or ss-DSSCs). In the case of ss-DSSCs, photo-anode morphology is fundamental for the percolation of the electrolyte. In fact, conducting polymer is injected in liquid phase into the device but, during the percolation, it solidifies and could not bath all the photo-anode surface, making imbalances in dye regeneration and charge transport. The photo-anode should have a large-pores structure where electrolyte could easily flow and occupy all available surface. I-K Ding et al. (2009)[72] used spin coating method to infiltrate the spiro-OMeTAD in a mesoporous film of TiO_2 with a thickness of 2μm. They achieved an efficiency of about 5%, which is less than liquid DSSCs, as we have seen. One of the causes is the too low thickness of the photo-anode, which does not guarantee a high light harvesting[73]; but, increasing the film thickness, HTM percolation is more difficult and the risk is to have a non-uniform distribution of polymer in the photo-anode pores, with an obvious loss in dye-regeneration efficiency and then a PCE decreasing. In this case, 1D and quasi 1-D structures could be a solution thanks to their preferential “channels”[74], moreover these morphologies allow a better light management thanks to their structure and thickness.[75] Another problem given by solid state is the charge mobility. In a solid conducting polymer, charge is slowed down by travelling along the polymer molecules, but Ahn et al. (2012)[76], using PEBII as HTM, achieved ionic conductivity of about 2.0×10^{-4} S/cm . Nowadays, the record PCE for ss-DSSCs is of 8% for TiO_2 based[74], using a tree-like morphology and PEBII electrolyte.

2.2.4.3 Quasi-solid

There is another solution that attempts to combine advantages of liquid and solid electrolytes and avoid their cons: quasi-solid DSSCs. This kind of devices were introduced for the first time by Cao et al. (1996)[77] and are characterised by the use of sol-gel electrolytes. Sol-gel is a particular technique to produce mainly ceramic materials. Colloidal solutions (Sol) are sensitised and are precursors for the subsequent formation of an inorganic net that holds an interconnected liquid phase (gel) by step of hydrolysis and condensation. After the gelation there are some thermic treatments to evaporate the liquid phase and to achieve a solid structure with implemented mechanical properties.[78]

For sol-gel electrolytes production, thermic treatments are not made, in this way it is possible to have an electrolyte that can percolate in a better way than solid ones and, also, is less volatile than liquid electrolyte, with consequent less problem of leakages.[79] Good results, in terms of efficiency, were obtained using, as solvents for Sols acetonitrile and acetone (about 6-7%)[80, 81], but they are volatile components, so one of the problem of liquid electrolyte is not overcome. Ileperuma et al. (2011)[82] achieved 7.27% conversion efficiency, using polyacrylonitrile (PAN) as host polymer without any volatile solvents.

The main problem to overcome are resistive losses in the bulk and at interface.[82]

2.3 Monolithic DSSC

Monolithic DSSCs (or m-DSSCs) are a particular kind of device that is a part of the DSSC family. They are different from common DSSCs for their structure. m-DSSCs could be divided in liquid or solid ones, depending on the electrolyte. Their characteristic is the absence of the glass where the counter electrode is deposited.[83, 84] This a fundamental characteristic because in this way it is possible to reduce costs, saving an FTO glass, and to decrease the weight. We can see the device structure in Fig.2.19, in this case, the upper glass is used as protection against environmental damage (rain, dirty, animals...) and to avoid the electrolyte evaporation (using a solid one this risk is avoided), but it can be substituted by a polymer coating, which is cheaper and lighter than an FTO glass.

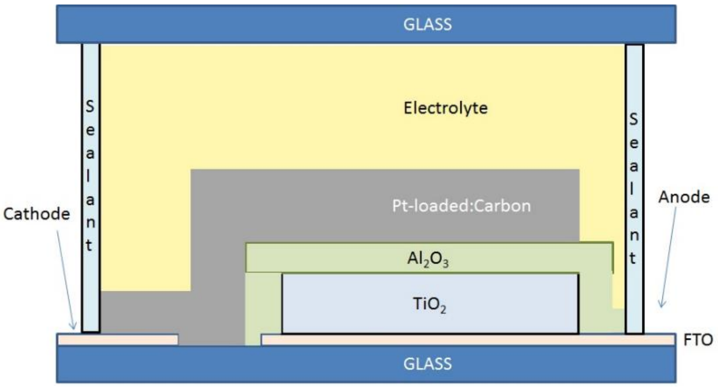

Figure 0.20 Scheme of a monolithic DSSC

Main components are the same, there is the FTO glass, the dye-sensitized TiO_2 photo-anode, the electrolyte and the Pt loaded carbon counter electrode and the working principle is the same. The main differences are the presence of a thin porous alumina (or Al_2O_3) film between the photo-anode and the counter electrode and the etching of a part of FTO. Alumina is a transparent insulating film that is used to avoid the short circuit between the two electrodes, in fact photogenerated electrons are injected in TiO_2 film and travel through the FTO to the anode, while the hole are transported by the electrolyte which permeates the three porous films (TiO_2, Al_2O_3, Pt-C) to the counter electrode for dye-regeneration. Another fundamental characteristic is the possibility to deposit before all three films (titania, alumina and carbon-platinum) and then, later or in another place, go on with the “wet part” (dye-loading and electrolyte percolation). Efficiencies are not yet at level of other devices, but Liu et al. (2012) [85] achieved PCE about 7.6%.

In this thesis, my aim is to characterize and optimize the deposited parts (TiO_2 photo-anode with Al_2O_3 spacer and C-Pt counter electrode). Relating to the photo-anode, I characterize how Al_2O_3 spacer affects the optical properties of photo-anode. Moreover, I exploit the possibility to deposit TiO_2 with another method: Plasma Assisted Super Sonic Jet Deposition. The reactor for the PA-SSJD is a prototype and in this work there is a first characterization of material deposited with this machine. The objective is to deposit TiO_2 that has the same morphology of that deposited by PLD, but the process time would be reduced and the deposition area increased. Relating to the counter electrode, I characterize the electronic and catalytic properties of C-Pt films, with different Pt load and thicknesses. In this way, I try to reduce the use of platinum, because it has a high cost, and, at the same time, I try to take advantage of the maximum active area for the catalytic reaction. Moreover, I investigate how the thickness of C layer affects the conductivity of the counter electrode, with the aim to optimize the electron conduction into this film, reducing the thickness and, then, the quantity of deposited material, with a saving in terms of costs and deposition time. The last part of my work is to fabricate an m-DSSC, testing the performance. Before to fabricate a monolithic device on the designed solar concentrator in TIFAIN project, we study the performances of the DSSC fabricated on flat FTO glass in order to optimize each time the different parts. When the device efficiency will achieve a satisfying value, the m-DSSC will be fabricated on the solar concentrator and then will be gradually optimized in order to fabricate building integrate photovoltaics modules.

3 Methods

In this paragraph, we will expose the deposition methods used for fabrication of samples and the instrument used for the characterization. During this work, I learnt to use the PLD reactor and the PA-SSJD reactor, while the magnetron sputtering deposition was performed by Francesco Fumagalli. Regarding to the part of characterization, I performed all the characterizations. The DSSC fabrication was made in collaboration with Luca Passoni.

3.1 Deposition Process

3.1.1 Sputtering

Grove observed sputtering for the first time in 1852, but he classified it as “dirt effect”. Only after over a century, scientists begun to study this technique to deposit different materials.[86] Sputtering is a process in which there is an emission of atoms or particles from a target due to a bombardment by energetic particles. In a vacuum chamber there are the TiO_2 target and the substrate interfaced. When there is High Vacuum (about $1 \cdot 10^{-3}$ Pa), we inject in chamber a gas that can be inert (e.g. argon) or reactive (e.g. oxygen), to promote the formation of the plasma. Sputtering deposition has two variants, which differ in the way to ignite plasma: in DC sputtering (for metals), ions are accelerated by an electric field in direct current; in RF sputtering (for semiconductors), energetic particles are accelerated in a rapidly in time variable field. Energetic particles (above all ions) in the plasma hit the target surface displacing atoms and particles, which goes on substrate surface and condensate creating the film.[87]

Magnetron sputtering was introduced in the early 1970s. In magnetron sputtering, there are some magnets near the target which create a magnetic field to affect electrons motion but ions one (Fig.3.1). In this way, electrons are confined near the cathode (target) and can not advance through the field against anode or chamber walls, so the risk of losing primary electrons due to collisions with wall or anode is drastically reduce and also the risk of spoiling the deposited film is decreased.[86] Moreover, thanks to the high ionization efficiency (i.e. ratio between the number of ionizations that a single electron performs and the number of ionizations performed by a well-confined electron in the absence of excitation and elastic collisions)[88], sputtering velocity, i.e. flux of clusters ablated from the target, is increased. With this process, it is possible to obtain columnar morphology with a preferential growth direction.[89]

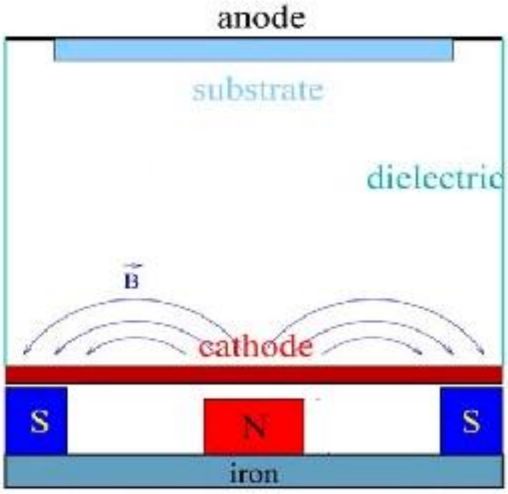

Figure 3.1 Schematic diagram of magnetron sputtering

Changing the various parameters (target-substrates distance, temperature of substrate) deposited film could be more or less porous and nanowire could change their diameter. This technique allows a large scale deposition, high quality of the films, the deposition of a lot of materials and blend, but the rate of deposition are low (about 0.1 μm/min) and this fact could lead to gas trapping in the deposited film. Furthermore, if target has not a high quality, it could "shoot" melted particles (spitting) on the substrate.[90] Conversion efficiencies achieved by DSSCs with photo-anodes deposited by sputtering are about 4%.[91, 92]

3.1.2 Pulsed Laser Deposition (PLD)

PLD is a Physical Vapour Deposition. The first thin film deposited using a laser was fabricated by Smith et al.(1965)[93], only five years after the laser invention by Maiman. This technique consists in the ablation of a target of the material to deposit with an excimer laser inside a vacuum chamber, which can be filled with a selected gas. The ablated particles create a plasma that expands supersonically with a gradient between the target and the substrate. Once in contact with the substrate, the particles condense and make a film.

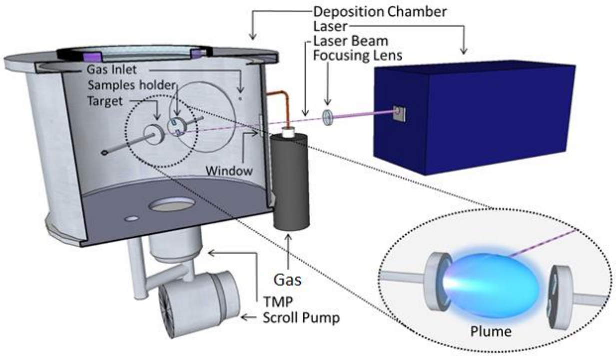

Figure 3.2 PLD schematic

Laser beam can evaporate a lot of materials, both metallic and ceramic; this characteristic is one of the main qualities of this deposition technique. The background gas affects the deposition, for example in TiO_2 deposition, using a titania target, the process is performed in oxygen, in this way the stoichiometry of the deposited film is maintained. Instead, during the deposition of carbon film the presence of an oxygen atmosphere is deleterious, because during the deposition an oxidation reaction happens and carbon ablated from the target becomes an oxide. In this case, an argon atmosphere is used, since argon is an inert gas. There are some parameters that affect the film morphology and the deposition rate. Among laser parameters, one of the most important is the laser fluence[J/cm^2], which is the energy delivered per unit area. Changing the laser fluence, it is possible to ablate more or less material with each pulse, affecting the deposition flux, the film quality and the stoichiometry.[94] The target-substrate distance is another of the main parameters, because it affects the kinetic energy of clusters ablated from the target and accelerated by the plasma plume. The other main parameter is the background gas pressure, which affects strongly the plasma plume density and, consequently, the kinetic energy of clusters. Working on these parameters, it is possible to deposit films with different morphologies or different stoichiometry(Fig.3.3[75]).

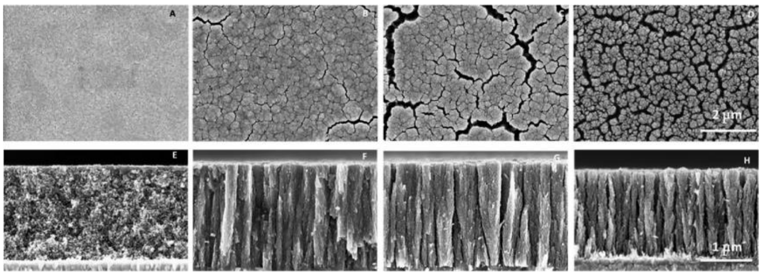

Figure 3.3 Top view SEM images of (A) nanoparticle paste and PLD films at (B) 5 Pa, (C) 7 Pa, and (D) 10 Pa. Cross section SEM images of (E) nanoparticle paste and PLD films at (F) 5 Pa, (G) 7 Pa, and (H) 10 Pa.

In Fig.3.3, we can see that increasing the oxygen pressure in the chamber, the TiO_2 morphology is less compact and the columns begin to become tree-like. This fact happens because, increasing the pressure, plasma becomes denser and particles suffer more shots between themselves, losing kinetic energy, before being deposited on the substrate.[40, 75, 95]

This technique guarantees an extremely fine control on morphology and thickness of the film and to deposit high quality crystalline films; it is also possible to alternate the layer with different porosity or different materials (changing the target). Possible drawbacks are low deposition area and deposition rate, cost of excimer laser and spitting.

In our machine configuration, there is the possibility to perform a co-deposition, adding the magnetron sputtering deposition of a material to the Pulsed Laser Deposition of another one (Fig.3.4). This fact is very interesting, because, in this way, it is possible to deposit blend films with different ratio between the two materials. In our case, we used this method for a co-deposition of carbon platinum films.

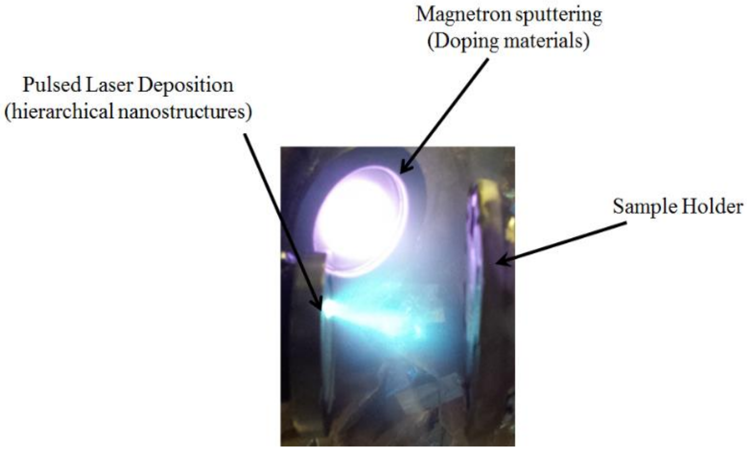

Figure 3.4 Example of co-deposition process Magnetron sputtering (violet plasma plume) + PLD (blue plasma plume).

3.1.3 Plasma Assisted-Super Sonic Jet Deposition (PA-SSJD)

A novel nanostructured material deposition technique is studied to verify the feasibility of scaling up the fabrication of titania hierarchically organized photo-anodes (quasi 1D morphology) over large area (10x10 cm2).

The design of the prototype, called delta source, exploits the division of the deposition process into two separate and independent stages: the reaction chamber and the deposition chamber. Precursor dissociation takes place in the reaction chamber in a plasma discharge, creating the clusters representing the building blocks of the deposited film. The created particles are then removed from the first stage and accelerate in a supersonic jet into the reaction chamber, where they impact on a substrate. The thin slit dividing the first and the second stage makes it possible, thanks to its limited conductance, to maintain the reaction chamber at higher stagnation pressure with respect to the second stage, thus establishing a supersonic jet in the latter, above a certain pressure ratio value.

We can see the machine schematics in Fig.3.5.

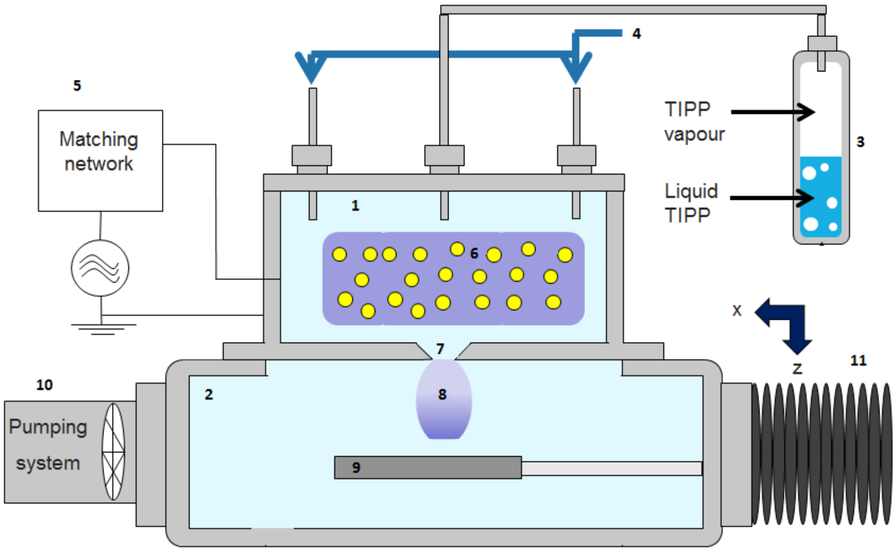

Figura 3.5 PA-SSJD reactor schematics

Different parts of the lay-out are:

1. Reaction Chamber (or Upper Chamber)
2. Deposition Chamber (or Lower Chamber)
3. Bottle with precursor
4. Additional gas inlet
5. Matching box
6. Plasma Discharge
7. Slit
8. Mach Disc
9. Sample holder
10. Pumping System
11. Motors

Reaction Chamber

In the reaction chamber a capacitively coupled discharge ignites an argon-oxygen plasma. Titanium isopropoxide, a liquid precursor of titania, is injected in the reaction chamber and dissociated in the discharge. The TTIP dissociation occurs in three possible ways: thermic decay, chemical interaction with oxygen and, the most important, by impacts with energetic particles (mainly ions) of the plasma.

Titanium (IV) isopropoxide (Fig.3.6) is a chemical compound with formula Ti{OCH(CH_3)$_2$}$_4$.[96] It is commonly used in Plasma Enanched Chemical Vapor Deposition (PE-CVD) as a precursor of titanium dioxide instead of titanium tetrachloride, because the latter could leave trace of chlorine into the film. At room temperature, TTIP is liquid, but, in contact with oxygen undergoes a rapid reaction with a consequent precipitation of a white powder, unusuable for the deposition process. The dissociation reaction enhanced by the Ar-O_2 plasma is:

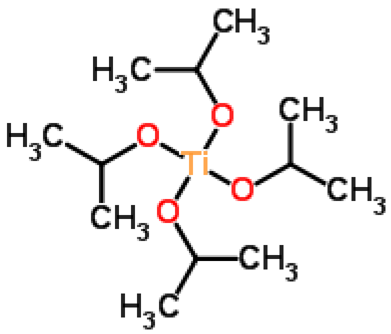

Figure 39.6 Titanium (IV) isopropoxide structure

$$\mathrm{Ti}\{OCH(CH_3)_2\}_4 + 18O_2 \rightarrow TiO_2 + 12CO_2 + 14HO_2$$

The bottle containing the precursor is heated to vaporize the precursor, by a sistem of electric blanckets connected with two PIDs (Proportional Integral Derivative controller), thus making it possibile to compensate for small temperature fluctutation and maintain a constant precursor flux inside the reaction chamber. The PID control parameter have been optimized the ensure the above said optimal control.

Several different designs for the injection system of the liquid precursor have been tested to evaluate the best possible configuration. The optimal configuration is schematized in Fig.3.7.

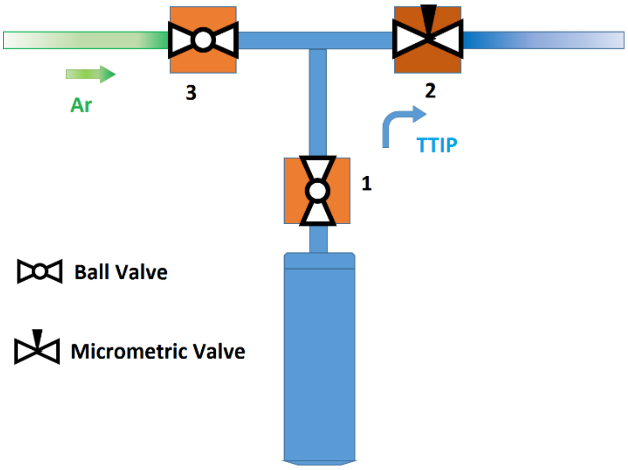

Figure 3.7 Scheme of new valves system

Valve 1 is an on-off ball valve, , when opened, allows the flux of evaporated TTIP up to valve 2. Valve 1 can be used to exclude rapidly the precursor flux in case of need . Valve 2 is a micrometric one, allowing fine control over the precursor flux towards the reaction chamber. Valve 3 is also a ball valve and is used to purge with argon the injection system from residual TTIP (at the end of the deposition process; valve 1 closed and valve 2 open). An Optical Emission Spectroscopy (OES) tool, was added to the reaction chamber in oder to monitor the dissociation of TTIP and the plasma reactions.Optical emission spectroscopy is a non-invasive method to charcterize plasma by recording the optical emission from the excited species inside of the plasma. OES system is composed by an optical fiber, a detector and it is connected to a PC. The optical fiber is applied on a viewport of the reaction chamber. The window should possibly be in quartz, because of the higher trasmittance of the material in visible and UV region (it absorbs below 200nm[97]), thus allowing a broader spectral range analysis and a more complete insight on the plasma composition. In my case, I control precursor dissociation, monitoring Halfa emission line from the Hydrogen Balmer series (emission wavelength 656,27 nm). TTIP dissociation in the discharge releases hydrogen, thus Hα increasing intensity can be considered a good indication of higher precursor dissociation.

In the first test Hα was monitored in order to verify that the precursor dissociation was constant during the whole deposition process. Fig.3.8 (Hα intensity vs deposition time) shows the good stability in time achived during the dissociation process. Hα value is almost constant along all the deposition time (20 min).

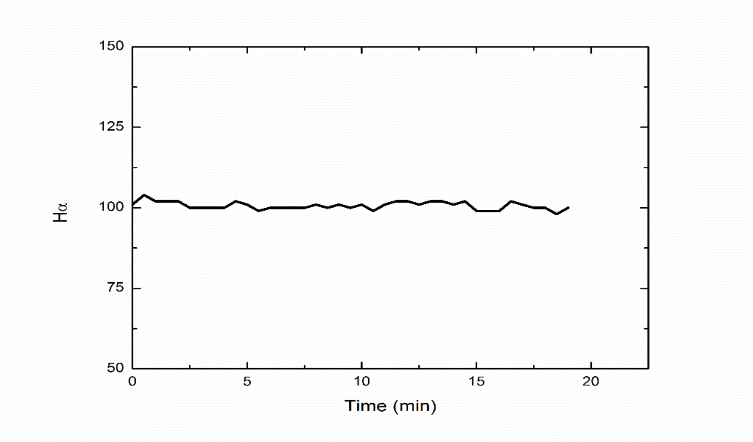

Figure 3.8 Hα value in time of TTIP during a deposition

Deposition Chamber

Fig.3.9[98] depicts the hydrodynamic phenomena occuring below the slit when a high pressure ratio is present between reaction and deposition chamber (over 2). A supersonic expansion of the gas is established in the deposition chamber, ending in strong recompression shockwave called Mach Disk. Below the Mach Disk the gas recompresses reaching the pressure value of the deposition chamber.

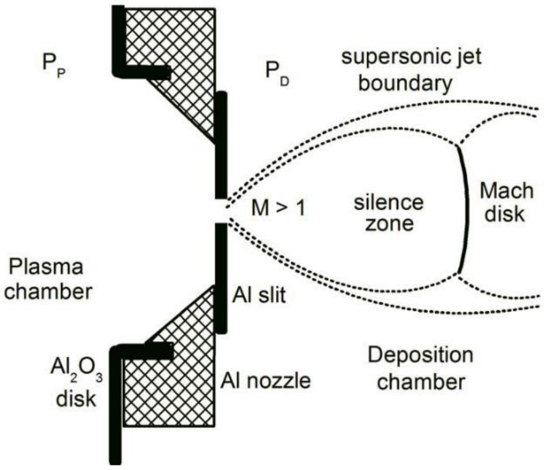

Figure 3.9 Cross section of nozzle region with a schematic view of the jet expansion in our experimental setup.

The chocked flow condition of the slit, for which the conductance does not change for pressure above a critical value, makes it possible to decouple the reaction chamber, where the production of the material takes place, from the deposition chamber, where it is possible to tune the material morphology.

Titania nanoclusters formed in the plasma are drugged by the gas expanding in the deposition chamber and undergo a strong acceleration . In the lower chamber a motorized sample holder is kept at a certain distance from the nozzle and moved back and forth in a direction normal to the one of the slit . The deposition process is based on the pressure ratio between the two chambers and the slit dimensions. These two parameters control the velocity of supersonic jet and the length of the Mach disk. The most important parameter (called Ω) to control the morphology is the ratio between the distance slit-substrate and the leght of Mach disc.

There are three main different conditions of deposition which we can be see in Fig.3.10:

1. The substrate is into the Mach disc and $\Omega<1$
2. The substrate is at the end of the Mach disc and $\Omega=1$
3. The substrate is out of the Mach disc and $\Omega>1$

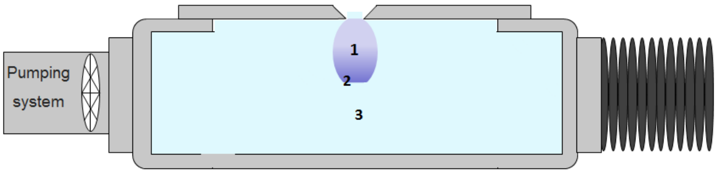

Figure 3.10 Schematic deposition chamber of Δ-source with in evidence the three different condition of deposition: 1) $\Omega<1$; 2) $\Omega=1$; 3) $\Omega>1$

When Ω is less than one, nanoclusters have high kinetic energy and the resultant film is characterized by low porosity. Increasing Ω, the morphology becomes more porouse and assumes tree-likes shape.

This technique allows to deposit, in theory, all materials that can be dissociated by the plasma, on a large area and with fast deposition rates (5µm/min). As I said, PA-SSJD reactor is yet a prototype under development to overcome the problems connected to the deposition process. Main studies are concentrated on the plasma charcterization during the deposition, the aim is to obtain a high denisty of oxygen radical in order to enhance the precursor dissociation by impact with energetic particles. The solution could be to find an optimum in the ratio Ar-O_2, linked to a higher plasma power. Regarding the homogeneity on the whole area of deposition, precursor injector with particular geometry (e.g. shower-shape), are being studied.

3.2 Characterization

3.2.1 Scanning Electron Microscopy (SEM)

To analyse the morphology of deposited materials and devices and to measure thickness of different films at micro- and nanoscale, I use a Scanning Electron Microscopy (SEM). Electrons are extracted from a tungsten filament at few keV, and accelerated (in a range of 20-30keV) in a condenser lens then through an objective lens and an aperture at last. In this way electrons are collimated in a beam that reaches the specimen (Fig.3.11)[99].

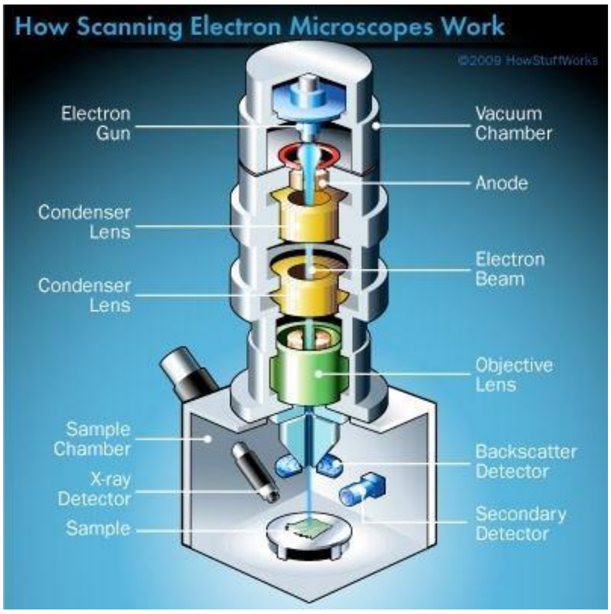

Figure 3.11 SEM schematic

Specimens have to be conductive for this kind of analysis, this is the reason why it would be better to use Si wafers as substrates. I use also FTO substrate, instead Si wafer, at the expense of image quality, but to reproduce the film growth conditions that could be different in the two cases. “Image capture” is based on the emission of secondary electrons from the specimen. The secondary electrons ejection is due to the inelastic scattering interactions of the incident beam. It is possible to have different degrees of magnification. In this way it is possible to observe each detail of the attained morphology, from the hierarchical structure of the whole substrate, to the detailed branches. Depending on where incident beam is conveyed, we can observe the morphology on top of the specimen or its section. From the section, we can measure the thickness of deposited film and its morphology (porous, nanostructured, nanotrees…).

I perform these characterizations using a JEOL Touchscope JSM-6010LA present in the CNST. In this case, the electron beam is produced by Tungsten (W) hairpin electron filament which is heated resistively to produce electron. This fact leads to an electron beam rather wide and the resolution is negatively affected (about 1µm). The SEM images that requires higher quality and magnification are taken with a Supra 40 Zeiss Scanning Electron Microscope of Dipartimento di Nucleare of Politecnico di Milano, thanking Luca Passoni for the collaboration. In this case, the electron beam is emitted by a Field Emission electron gun. A wire of Tungsten with a very sharp tip (less than 100nm) produces an electron beam using the field electron emission. The emitted beam is closer than the previous one and the focusing ability is increased very much (maximum resolution about 2nm).

3.2.2 Raman Spectroscopy

In order to investigate the deposited substrates energetic states, I perform a spectroscopic analysis using a Renishaw inVia Raman microscope/spectrometer (Fig.3.12), for Raman spectroscopy analysis.

Figure 3.12 Renishaw inVia Raman microscope/spectrometer

Raman spectroscopy is a technique that consist in exciting vibrational, rotational and other low-frequency energetic levels of crystals. It is based on an inelastic scattering process (Raman scattering) that happens when a monochromatic light beam interacts with molecular vibrations or phonons of the system. The result is an energetic shift of photons upwards or downwards. A monochromatic laser light illuminates sample and the scattered photons are collected by a lens and then dispersed on a detector. As we said above, Raman effect is an inelastic scattering process, in which incident photons are absorbed and re-emitted by the substrate. Re-emitted photons have an energy profile that depends on the interaction suffered by photons. Almost all of incident photons suffer Rayleigh scattering: an elastic interaction with the material in which incident photons continue their motion with the same kinetic energy (frequency and wavelength) they had before the interaction with the sample. Only about 1 per 10^7 incident photons are scattered by an excitation. In this case, excited molecules relax in different states more or less energetic. These processes are called Stokes and anti-Stokes scattering (Fig.3.13)

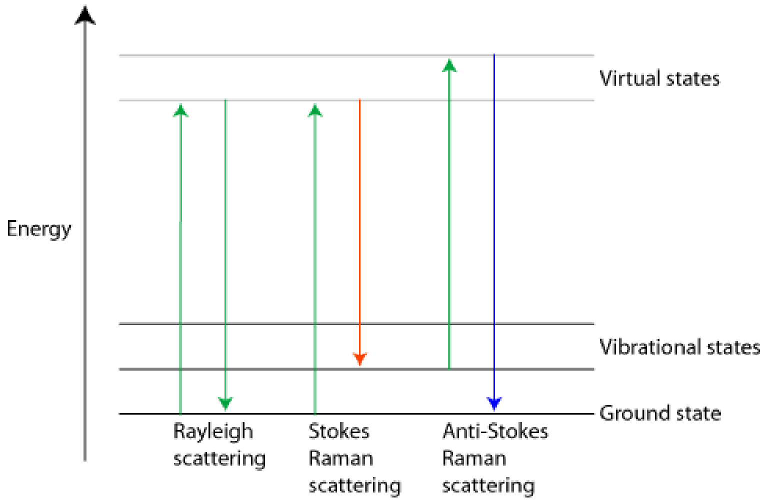

Figure 3.13 Schematic of the different light scattering possibilities: Rayleigh, Stokes and anti-Stokes.

Since molecules are excited at virtual states, incident photons do not need energetic requirements. Scattering process corresponds to the creation/destruction of vibrational energy quanta and depend on what bond is present in the material. Each kind of bonds has resonant wavelengths that provide form maximum yield. In the Raman spectrum, observable peaks indicate the kind of bonds present in the material, in this way it is possible to verify what allotropic phase is present or which bonds.

3.2.3 UV-Vis Spectroscopy

The optical characterization regarding transmittance and absorbance of the different deposited materials and roughness factor extrapolation are performed by a Perkin Elmer Lambda 1050 UV/Vis/NIR system (Fig.3.14) with a 150mm integrating sphere employed as spectrophotometer.

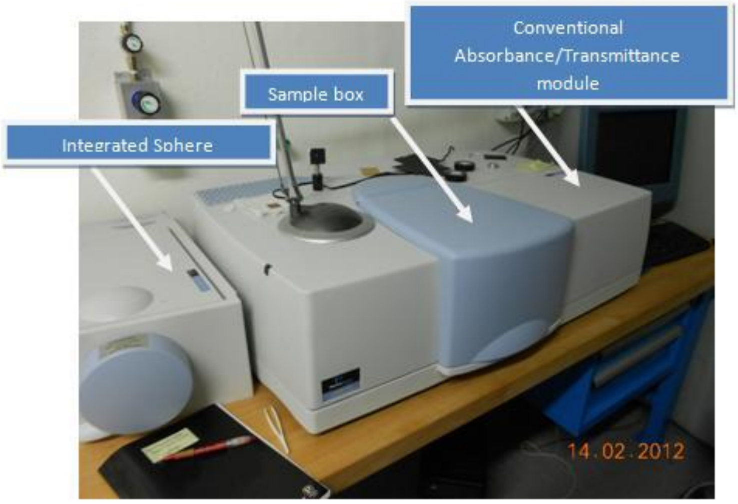

Figure 3.15 Perkin Elmer Lambda 1050 UV/Vis/NIR system

As we can see in Fig.3.14, this machine has two modules, in addition to the integrating sphere modulus there is a conventional absorbance/transmittance one used in order to measure optical properties of a solution in a cuvette. Integrating sphere is in spectralon, a fluoropolymer with a very high diffuse reflectance over the ultraviolet (UV), visible (Vis) and near-infrared (NIR) regions of spectrum[100]. In this way, it is possible to have a complete light collection in total and diffuse transmittance/reflectance, also for high scattering materials. In Fig.3.15[101] an optical design of the integrating sphere is represented.

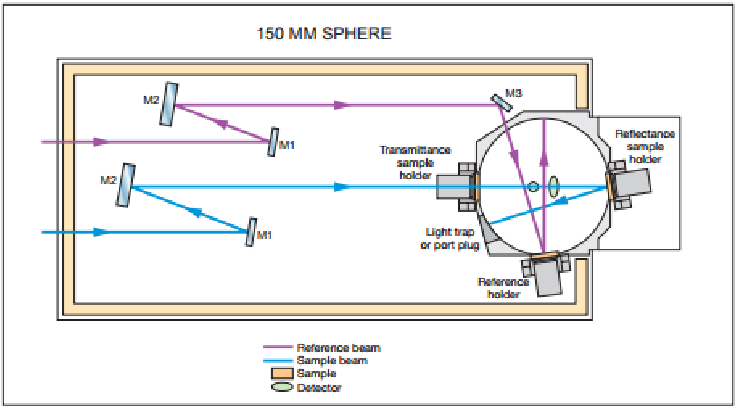

Figure 3.14 Optical design of integrated sphere

There are two light beams that go through a monochromator, one (violet in the outline above) is the reference beam and is sent directly into the integrating sphere to the reference holder. The second beam (blue in the outline) comes in contact with the sample. The sample position is crucial for the kind of analysis: for transmittance, the beam goes through the sample before entering into the integrating sphere; in case of reflectance analysis, sample beam goes first through the sphere and then hits the sample. Then, a detector collects the percentage of transmitted/reflected beam and plot the data in a graphic in function of fathomed wavelengths.

Having transmittance and reflectance of a specimen, it is simple to obtain the absorbance with the formula:

$$A = 1 - T - R$$

Where A is the absorbance, T is the transmittance and R is the reflectance. I perform the measurement with a wavelength range that goes from 1300nm to 300nm, with acquisition steps of 1nm. Since the openings of the integrating sphere are larger than our specimen, I have to use masks that cover in part the hole, but, in this way, measures are not perfectly precise and some light is lost.

To calculate the roughness factor, after having unloaded the dye from the specimen, I take 3ml of the NaOH with desorbed dye solution in a cuvette and I measure its transmittance with the UV-Vis spectrophotometer. It has a pick of absorbance at 530nm.

Through the Lambert-Beer equation, we can calculate the dye concentration in each solution:

$$A = \varepsilon_{\lambda} l M$$

where A is the absorbance, ε_{λ} is the molar extinction coefficient (14000 l/(mol*cm)), l is the path length (1cm) and M is the analyte molarity. I calculate the solution molarity and, knowing the volume of solution (3ml), the number of moles of dye particles. To have the number of dye particles, I multiply the number of moles for the Avogadro number. Since the single dye molecule surface is of $1.6\text{x}10^{-12}\text{mm}^2$, I can calculate the total dye surface. The roughness factor is the ratio between the total dye surface and the specimen geometrical surface.

Another parameter that can be calculated by UV-Vis spectroscopy analysis is the maximum expected photocurrent generated by the absorbance of photons and production of electrons. We assume that the External Quantum Efficiency (EQE) is equal to one. This means that every incident photon absorbed by the sample is converted into an electron. I make this hypothesis in order to obtain the maximum photocurrent, in case that the incident photons generate the same number of electrons. The next step is to calculate the Light Harvesting Efficiency (LHE), which gives the percentage of incident photons absorbed by the dye, according to the formula:

$$LHE = A_{dye} - A_{unloaded}$$

where A_{dye} is the absorbance of dye loaded specimen, while $A_{unloaded}$ is the absorbance for a sample without dye.

Fixed these parameters, the formula to calculate the maximum expected photocurrent (or $J_{SC,max}$) is:

$$J_{SC,max} = \int EQE \times LHE \times photon\ flux \times q\ d\lambda$$

Since EQE is equal to one, the formula becomes:

$$J_{SC,max} = \int LHE \times photon\ flux \times q\ d\lambda$$

Where q is the electron charge (1.6E-19C) and photon flux [$m^{-2}\ s^{-1}\ nm^{-1}$] is the number of incident photons per second per unit of area. The photon flux is filtered using the Air Mass coefficient AM1.5, which gives the number of photons of solar irradiance that arrive at mid-latitude. The sunlight has suffered a higher attenuation by the atmosphere when arrive to the ground at mid-latitude because the atmosphere is thicker than the atmosphere of equatorial and tropical regions. Maximum expected photocurrent is calculated integrating respect to all fathomed wavelengths.

3.2.4 Current-Voltage Characterization

Characterization of our fabricated monolithic cells is performed by a Newport Oriel Sol3A solar simulator (Fig.3.16). The devices are connected to the instrument by two electrodes covered with Ag paste and are exposed to an irradiance that is 1.5AM in according to the ASTM E927-05 standard. Through the two connectors a potential difference is applied, the instrument measures the current generated by the device and plots the result in the current-voltage characteristic of the device (Par.2.1).

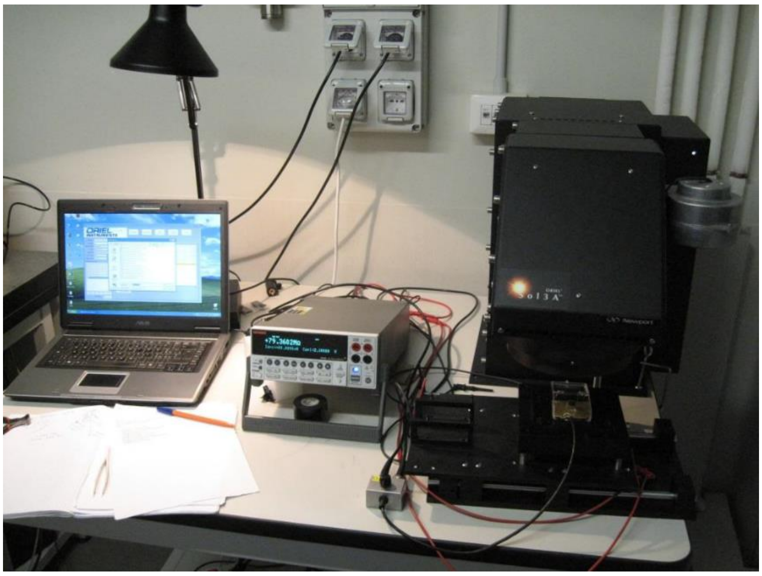

Figure 3.16 Newport Oriel Sol3A solar simulator picture

3.2.5 Electrical Characterization

A film resistivity characterization is performed on the carbon platinum counter electrode, to observe how the electrical properties of the material change with different load of platinum and with different thickness of the film. To make this analysis, I use an Ecopia Hall Effect measurements system (Fig.3.17).

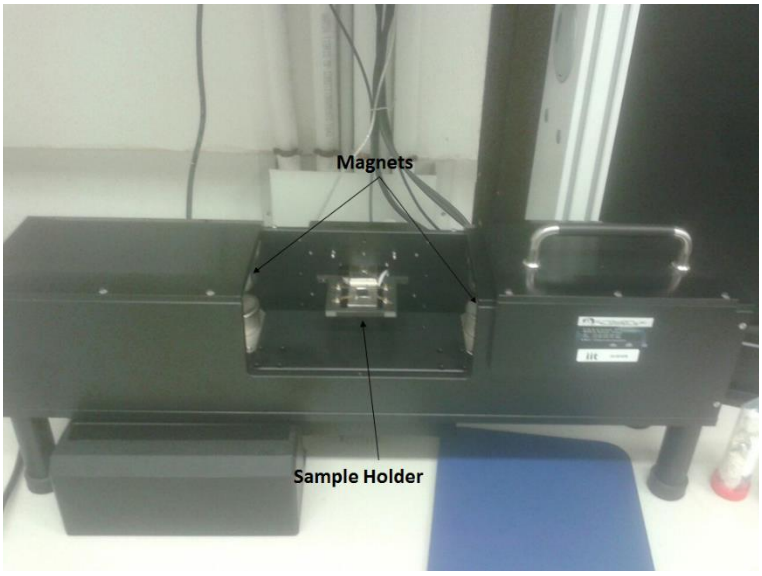

Figure 3.17 Ecopia Hall Effect measurements system

I use the van der Pauw (to four points) method to measure the bulk concentration (concentration of charge carriers) and carrier mobility (how quickly a charge carrier can move through a material when is dragged by an electric field). It consists in a sample-holder with four tips in gold and four magnets, coupled in order to have two couple N-S, and they are orthogonal respect to the sample holder and have the polarity inverted one respect to the other one.

To perform the measure of the resistivity, a current (in our case 5μA) is circulated from alternatives from a tip to another one, following the side of the square. While the current circulates, the two couples of magnets are moved, alternatively, on the samples, to measure the Hall effect.

Conduction electrons, injected by the tips into the film, move into the magnetic field and undergo the Lorentz force:

$$\vec{F} = q\vec{v} \text{ x } \vec{B}$$

Where q is the electron charge (equal to -1.6×10^{-19}C), v is the electron velocity and B is the magnetic field. The Lorentz force make a deviation in charges path.

After enough time, there is an equilibrium between the longitudinal electric field, which makes the Hall voltage and the Lorentz force:

$$qE = qv_dB$$

Where E is the electric field and v_d is the electron velocity (or drift velocity). Since the Hall voltage is:

$$V = Ed$$

Where d is the thickness of the material; we calculate E and, consequently, the drift velocity. Knowing the physic dimensions of the conductor and electric current intensity, it is possible to know the charges density into the specimen, in fact:

$$n = \frac{i}{qv_dA}$$

Where A is the specimen area and i is the electric current intensity (also called Hall current). Having the electric field value and the drift velocity, it is possible to calculate the charges mobility:

$$\mu = \frac{v_d}{E}$$

The electric conductivity can be calculated by the expression:

$$\sigma = q\mu n$$

Since electric conductivity is the inverse of resistivity:

$$\rho = \frac{1}{\sigma} = \frac{1}{q\mu n}$$

In this way, it is possible to know how a film conducts or not and if there are relevant difference between films with different platinum loads or thicknesses.

4 Results and Discussions

This thesis work is embedded in the wider research context of nanostructured materials development for photoelectrochemical exploitation of renewable energy sources performed at the Nano2Energy Laboratories (Center for NanoScience and Technology @ Polimi, Istituto Italiano di Tecnologia) and in particular it represents a contribution in the sector of photovoltaic applications which is actively studied at the Nano2Energy Laboratories. The bases of this work are the results obtained in the last years by Di Fonzo et al. (2009)[95] in synthesis of nanocrystalline TiO_2 hierarchical nanostructures by PLD and by Passoni et al.(2013)[75] in the fabrication of ss-DSSCs using these TiO_2 nanostructures as photo-anodes. Regarding the deposition method, Di Fonzo et al. (2009)[95] performed a complete characterization of how the oxygen pressure in the deposition chamber affects the TiO_2 morphology and structure. Passoni et al. (2013)[75] used the previous work to fabricate a ss-DSSC with a TiO_2 photo-anode deposited by PLD. They obtained a maximum efficiency of 3.96%. The aim of this thesis work is to fabricate a functioning monolithic DSSC starting from the Pulsed Laser Deposition process optimized by Di Fonzo and the device fabrication of Passoni. I am inspired the fabrication method of monolithic DSSCs proposed by Han et al.(2009)[102] and Petterson et al.(2010)[103]. This is the first step of a research project named TIFAIN, which aims for develop monolithic DSSC for Building Integrating Photovoltaic (BIPV).

The experimental section is organized as following: first the characterization and optimization of the different functional elements of the monolithic DSSC structure (photo-anode and counter-electrode) is reported then the fabrication of a working monolithic device is described and discussed. In the part of photo-anode characterization there is a brief report describing the preliminary results obtained using novel deposition method (PA-SSJD, Par.3.1.3) for nanostructured photo-anodes fabrication. PA-SSJD concept shows a great potential for increasing the deposition area and the deposition rate of ns-TiO_2 photo-anodes, in order to develop a new cheaper and faster way to fabricate the devices on a large scale. In this way, the cost of electricity could be reduced and the deposition process could be industrialized.

4.1 Photo-anode characterization

In this paragraph, I am going to do a characterization of the photo-anode used for the building of a monolithic device. Picking up on Par.2.2.1, it is important to summarize the main characteristics of a photo-anode. Firstly, it is a porous wide-bandgap semiconductor, which allows the conduction of electrons, injected from the chemisorbed dye to the Transparent Conducting Oxide (TCO). As shown above, the best structure, that could ensure the carriers transport, is the one that provides a linear path from the dye/photo-anode surface, where electrons are injected, to the TCO. In this context, it could be useful to take advantage of the columnar 1D and quasi-1D structures shown in Par.2.2.1.4 (nanotubes, nanorods, trees, etc.). The second important feature is the light transmittance, at least in the visible range, where dye has the main absorption peak (530nm). Otherwise, if the photo-anode absorbed all the visible light, the dye would not be exited and the electrons photogeneration would not take place. From this point of view, TiO_2 ensures a good transmittance, since it is a material that mainly absorbs in the UV range. The third important feature of a photo-anode is to promote and enhance the light management. It is a very important characteristic, because allows to maximise the incident light and enhance the performance of the device. As shown before (Par.2.2.1.3), the light management is based mainly on the scattering of the light. Light scattering is that physical phenomenon for which an incident photon suffers of a casual deflection after an elastic (or quasi-elastic) interaction with a particle. Scattering differentiates from reflectance and refraction because these two phenomena change the light trajectory in a controlled and determined way.

The importance of scattering phenomena in for the light management lies in the Lambert-Beer formula, showed in Par.3.2.3:

$$A = k_{\lambda} l$$

Where A is the absorbance, k_{λ} is the attenuation coefficient (an intrinsic characteristic of the material, dependent by the wavelength) and l is the thickness of material traversed by the light. This last parameter is what correlates the absorbance to the scattering power. In fact, increasing the light path, the absorbance increases. There are two ways to enhance l: the first one is to deposit a thicker film, the second one is to increase the optical path of photons into the film, taking advantage from the scattering. In this case, the beam undergoes to multiple scattering phenomena due to the morphology of the material and remains “confined” into the film, enhancing the probability of being absorbed. In this part, I use the optimization work performed by Passoni for fabrication of ss-DSSCs, because the aim is the same. The hyper-branched structure allows a higher light absorption than a standard mesoporous TiO_2 substrate. In my case, I have, in addition to the TiO_2 photo-anode, also an alumina film which plays the role of electrical insulating layer between the photo-anode and the counter electrode, so that it avoids a short circuit that can occur after an eventual contact of the two. Moreover, it should have a porosity that allows the infiltration of dye in the TiO_2 and the percolation of electrolyte. I begin investigating how the deposition of Al_2O_3 on top of the TiO_2 photo-anode affects its features, mainly the morphology and the optical properties.

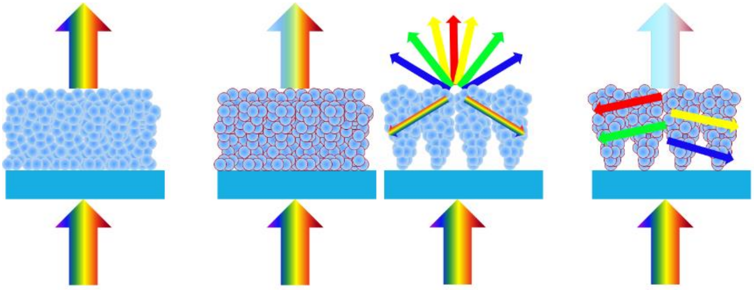

Figure 4.1 Schematics of the light-trapping and light-scattering behaviour of [left] a standard mesoporous TiO_2 substrate and [right] a hierarchical mesoporous TiO_2 substrate. Both structures are illustrated without sensitizing material and with sensitizing material

4.1.1 TiO_2 Photo-anode and Al_2O_3 Spacer deposited by PLD

Samples were deposited on Dyesol TEC15 Glass Plates, consisting in 3.2 mm-thick soda-lime glass with a commercial FTO conducting coating (15 $\Omega/_{m^2}$ sheet resistance and ±10 μm flatness). The glass sheets came in 300 mm x 300 mm size and afterwards was cut in proper size with handy cutter, paying attention to do not scratch FTO layer. Photo-anode characterization was performed on samples fabricated on FTO substrate of area 20mm x 15mm masked with a free area of 10mm x 10mm in the centre of the specimen. The substrates were cleaned with a fixed treatment: 10 minutes ultrasonic bath in acetone, 20 minutes ultrasonic bath in isopropanol to further remove any residual particles. The last step was the Oxygen Plasma Cleaning, performed for 5 minutes at 100 W to eliminate the last eventual contaminant and clean completely the surface.

TiO_2 film was deposited by PLD technique at 7Pa in oxygen with 105k pulses (about 5μm). On some specimens was deposited also Al_2O_3 on top of the TiO_2 by PLD.

Samples with TiO_2 were unmasked and subsequently re-masked leaving a free area of 10mm x 10mm that covered precisely the TiO_2 film. Al_2O_3 is deposited at 30Pa in oxygen atmosphere with 36k pulses (about 3μm).

For all depositions, laser parameters and conditions were the same, derived by a previous meticulous study[95]: laser fluence was 400mJ and repetition rate 20Hz. The deposition was done performed in dynamic mode, by rotating the substrates holder continuously at 10rpm, to obtain a uniform deposition.

After the alumina deposition, the devices were annealed in a furnace at 500°C for 2hs. This process of annealing is necessary to achieve the crystalline transition in TiO_2 from amorphous form to the Anatase phase.

4.1.2 SEM Characterization

The first step was to ensure that studies performed by Di Fonzo, about PLD method, would be replicable for used materials. After the deposition process descripted in Par.3.1.2, I analysed the device structure using the SEM (in this case the SEM image acquisitions were performed by Passoni with SEM present in Dipartimento di Nucleare). Fig.4.2 shows the cross section of my deposited specimen, specifying the thickness of each layer.

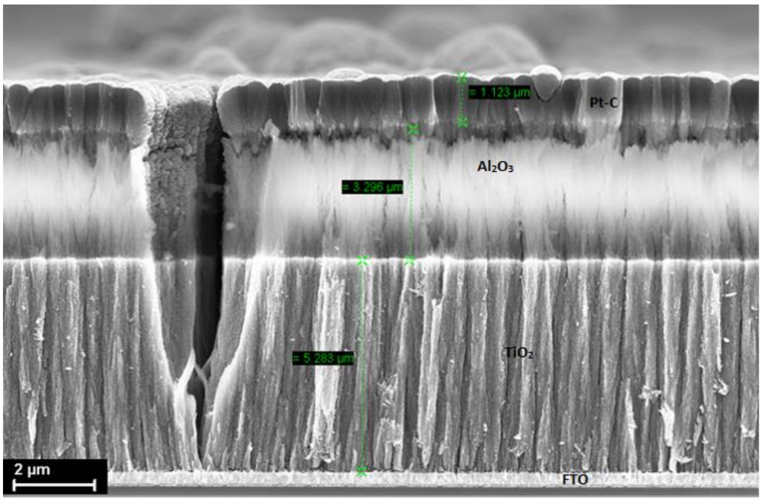

Figure 4.2 SEM image of a monolithich's cross section, where are signed different thickness of TiO_2 photo-anode, Al_2O_3 spacer and C-Pt counter electrode

Thicknesses were almost those requested, this fact shows the high precision and replicability of PLD process. The morphologies were the same expected. The TiO_2 columnar structure should be emphasized, because, as I said before, it is an important factor in light management.

In that figure, it is possible to note a crack orthogonally to the layers. Observing a sample, where was deposited a TiO_2 film covered by an Al_2O_3 layer, before and after the annealing process, it is possible to note that, before the annealing the sample surface presented a lot of droplets. There is an example in Fig.4.3.

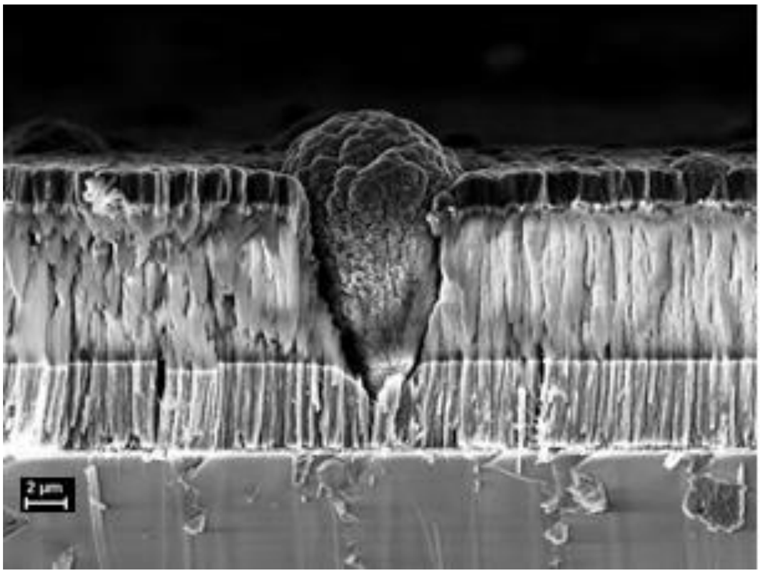

Figure 4.3 SEM image of a droplet present in the deposited films.

Droplets are some big aggregates that are detached from target and deposited on to the substrate during the deposition. It is a common defect in deposition methods with a beam that ablate a target.

During the annealing, these droplets could detach and leave the TiO_2 surface exposed to the air (Fig.4.4).

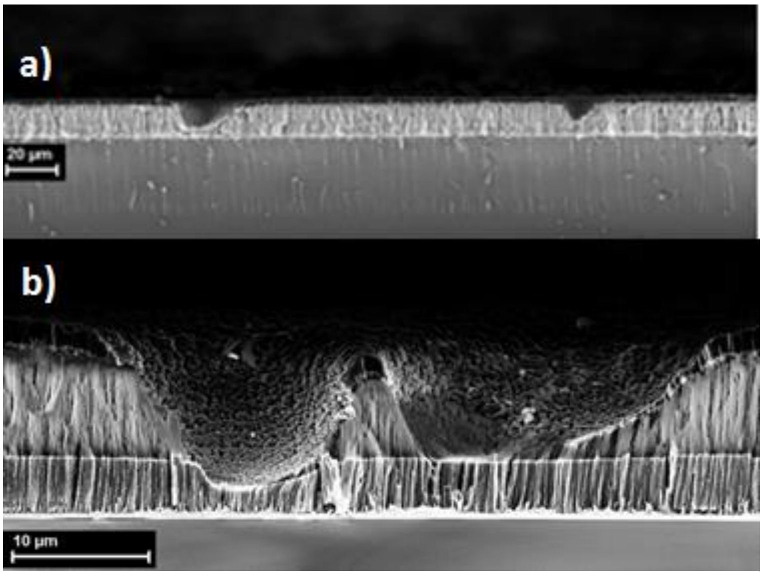

Figure 4.4 SEM images at two different magnifications of holes left by droplets detachment

This could be a serious problem because, during the carbon platinum deposition, an amount of material could deposit into the crack leading a short circuit between TiO_2 and carbon platinum. An idea to overcome this problem is to anneal the TiO_2 alone and then deposit alumina and carbon-platinum layers, but I have not yet experienced.

4.1.3 Optical Characterization

The characterization of optical properties arises from the necessity to investigate which is the contribute given by the alumina film deposited on top of the titania photo-anode. I performed different measures by UV-Vis spectrophotometer on specimens:

- Transmittance and reflectance of unloaded TiO_2;
- Transmittance and reflectance of dye loaded TiO_2;
- Transmittance and reflectance of unloaded TiO_2+Al_2O_3;
- Transmittance and reflectance of dye loaded TiO_2+Al_2O_3.

The first step was to compare their Haze factors, which is the ratio between the Diffuse Transmittance (DT) and the Total Transmittance (TT) of specimen not dye loaded:

$$Haze\ Factor = \frac{DT}{TT}$$

It is an indication of the percentage of transmitted light is affected by a scattering process passing through the deposited film. As shown before, scattering process is very important in the light management because allows to increase the light path into the film, enhancing the possibility of a higher light absorption. The higher is the Haze factor and the longer will be the light path into the photo-anode. The results are showed in Fig.4.5.

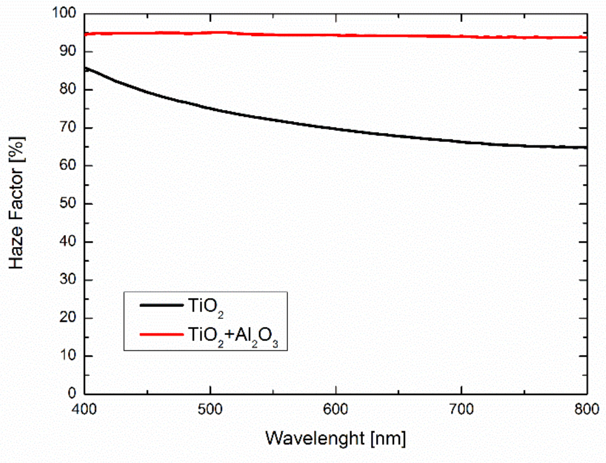

Figure 4.5 Haze factor of TiO_2 and TiO2+Al_2O_3 deposited by PLD.

The presence of the alumina porous layer gives really high constant scattering values of about 95% on all visible spectrum, while the only TiO_2 film has values that ranging from 70% to 85% along the spectrum, with a progressive increase towards the UV wavelengths. In literature, there are maximum values for TiO_2 films in line with those reported in this work. Fig.4.6 shows three possible morphologies of TiO_2 photo-anode, with their relative Haze factor values.[104]

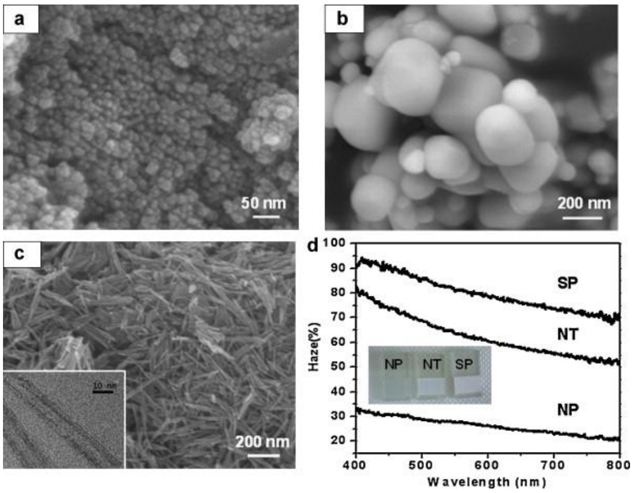

Figure 4.6 SEM image of TiO_2 a) microparticles, b) nanoparticles, c) disordered nanotubes. d) Haze factor vs wavelength for the three different morphologies and photography of three specimens.

Film composed by submicron particles (SB) has the highest Haze factor among the three examples and it is higher than my TiO_2 hierarchically nanostructured specimen. This fact could be explained with the bigger size of submicron particles respect to the nanometer one, according to the difference between Rayleigh and Mie scattering explained in Par.2.2.1.2. Larger particles have a higher cross section, this fact allows an higher probability to have an interaction between the incident light and the particle, with an eventual scattering process. Furthermore, the thickness of their specimens (12μm) is more than double of mine (5μm), so also the path length that crosses orthogonally the material without scattering process is longer than mine is. Nevertheless, the difference in values is not so high, above all at high wavelengths, sign of a higher presence of scattering phenomena in my photo-anode. The specimen fabricated by disordered nanotubes (NT) shows slightly lower values of Haze factor respect to my morphology. This fact could be attributed to lack of a hyper-branched structure, the scattering process is promoted by the random position nanotubes and thickness of the film, without an optimization of light trapping with the study of a better way to dispose the NTs. Specimen fabricated by nanoparticles (NP) shows the lowest values, less than 50% of others. The particles have a so small size (20nm) that light could not interact with them and the result is low diffusion by this specimen. This difference can be seen with naked-eye observing the photography present in Fig.4.6-d, where the three deposited specimens are showed. The scattering effect is represented by the fact that, at the same thickness and material, the NP sample shows a much higher transparency than NT and SP specimens, which appear white.

Then, returning to the results obtained by me, the higher Haze factor value of specimen with Al_2O_3 could be explained, in consideration of the above, with the higher thickness of the sample and the different refractive index between TiO_2 (2.5 for anatase)and Al_2O_3 (1.726). This difference could lead to a complete reflectance, when the incident light hits the surface TiO_2/Al_2O_3 with a critical angle, calculable with the Snell formula:

$$n_1 \sin \theta_1 = n_2 \sin \theta_2$$

Where n_1 of material from witch arrives the light (in our case TiO_2), θ_1 is the angle between the surface normal and the incident light, n_2 is the refractive index of material where light is refracted (in my case Al_2O_3) and θ_2 is the angle between the surface normal and the refracted light. The complete reflectance occurs when the light passes from a denser material to a less dense and the following condition is verified:

$$\frac{n_1}{n_2} \sin \theta_1 > 1$$

For the couple TiO_2/Al_2O_3, the critical angle is 43.66°. This means that, in my case, the light that, after crossing the glass, the FTO and the TiO_2, undergoing refraction processes and scattering phenomena, arrives at the TiO_2/Al_2O_3 surface with an angle higher than critical angle is reflected again in TiO_2 layer and re-scattered. This leads an important increasing in path length with the consequent enhancing in Haze factor value, along all visible spectrum.

In Fig.4.7, the comparison between the reflectance of the sample with only TiO_2 and that one of the sample with TiO_2 and Al_2O_3 is shown.

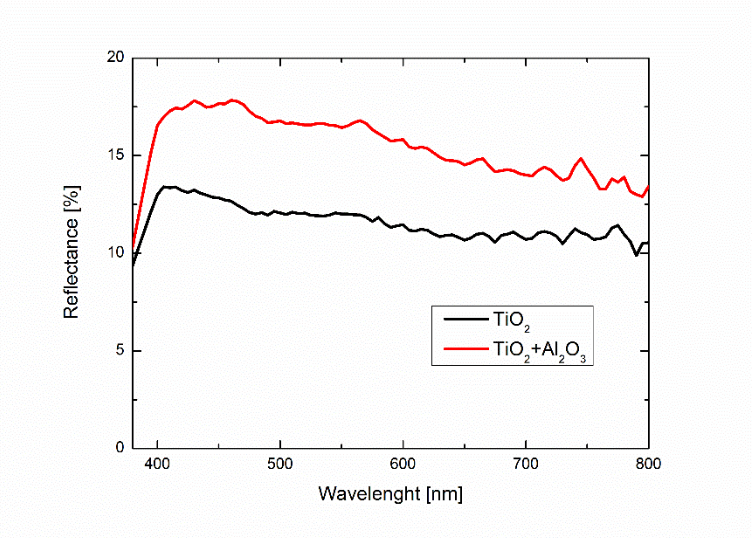

Figure 4.7 Comparison between the reflectance of only TiO_2 (black) and TiO_2 plus Al_2O_3 (red)

The two reflectances have the same trend along the spectrum, but the presence of Al_2O_3 gives a value of about 10% higher than that one with only TiO_2. This could be the confirm of the hypothesis done previously: the alumina layer, with its lower refractive index, enhance the light reflection.

TiO_2 was deposited in tree-shape morphology, instead in the nano-particles, because, even if the scattering power is the same, there is a difference in the charge transport. As I said before (Par.2.2.1.1), in 1D and quasi-1D structure there is a preferential path for the electron transport from the dye/TiO_2 surface to the FTO, while the random nanoparticles offer a large ways for charge transport, with an increasing in a charge recombination probability.

The next step was to compare the LHE, to really have an idea of how and how much the film of alumina affects the light trapping and the absorbance of light when the specimen is sensitized with dye.

After the annealing process, the samples underwent a dye loading process. B2 (N719) Dye from DYESOL is the commercial ruthenium-based dye used for device fabrication. The solution was prepared with the following recipe:

- 4.75mg of N719
- 10ml of tert-butanol
- 10ml of acetonitrile

The solution must be steered for 6hs, while devices were put on a hot plate at 140°C for about 6hs to desorb humidity adsorbed into the deposited films.

After the steering, dye solution was put in a weighing bottle. When devices were below 70°C (boiling temperature of dye solution), they were immersed into the solution and left in the bath for 16hs so that dye particles can be chemisorbed to different films.

The Light Harvesting Efficiency (LHE) is calculated with the formula:

$$LHE = A_{dye} - A_{unloaded}$$

Where A_{dye} is the absorbance of dye loaded specimen, while $A_{unloaded}$ is the absorbance of specimen without dye. This factor shows the light percentage absorbed by the dye, which can photo-excite the sensitizer molecules and create a photocurrent with injection of electrons in the photo-anode. LHE is connected to Haze factor by the Lambert-Beer equation in the way that I explain above: the Haze factor affects the path length travelled by the light into the film, the absorbance increases with the path length increasing. Observing the Fig.4.8, I found that at high wavelengths the trend is the same shown in the Haze factors and specimen with Al_2O_3 shows a higher LHE in near-IR region.

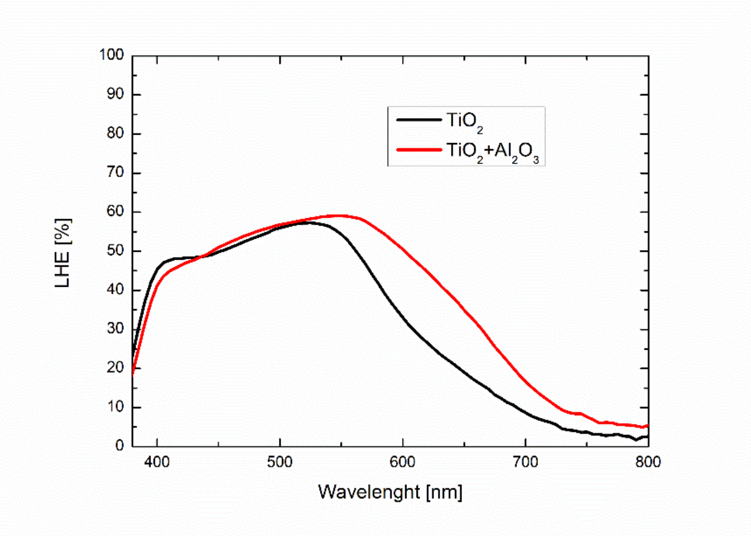

Figure 4.8 Light Harvesting Efficiency of TiO_2 and $TiO_2+Al_2O_3$

Instead, LHEs of the two specimens are practically identical in the 500nm zone, where is localized the dye absorbance. This result could mean that the alumina layer, after the dye loading process, did not give an important contribute in the light absorbance. A possible hypothesis could be that the very high porosity of alumina reduce the quantity of dye that can chemisorb on its. This fact could be interesting, because, in this case, there would no parasitic absorbance due to the Al_2O_3 and the incident photons would be absorbed only by the TiO_2 with the consequent photocurrent generation. I investigated this fact performing an unloading process onto the dye loaded samples, both with and without Al_2O_3. The unloading process was performed rinsed devices one by one with 4ml of a basic 0.1M sodium hydroxide (NaOH) solution that desorbed dye from the device. 3ml of solution with unloaded dye and NaOH were collected in a cuvette and analysed with spectrophotometer.

To extrapolate the dye molecule numbers chemisorbed on the specimens, the Lambert-Beer equation for the solutions was used:

$$A = \varepsilon_\lambda l M$$

Where A is always the absorbance, ε_λ is molar extinction coefficient, *l* is the path length and M is the solution molarity. The number of dye particles chemisorbed onto the device was calculated with the method exposed in Par.3.2.3 and I obtained that in sample with Al_2O_3 there were a more than twice particles ($4.43E15\mu^{-1}$) respect to the number in the only TiO_2 sample ($1.94E15\mu^{-1}$). This means that my previous hypothesis was wrong and dye chemisorbed on the alumina. Our second hypothesis for the difference between the two LHEs was that one explained when I talked about the critical angle to have total reflection: light beams that, crossing TiO_2, arrives to TiO_2/Al_2O_3 surfaces with an angles higher than 43.66° are totally reflected and re-scattered by sensitized titania film where they are absorbed almost totally. This should lead to a high absorbance, in order to respect what we said before correlating the scattering, the path length and the absorbance. But, looking in the literature (Fig.44)[64], I found that, even if the Haze factor value increases, the Incident Photon-

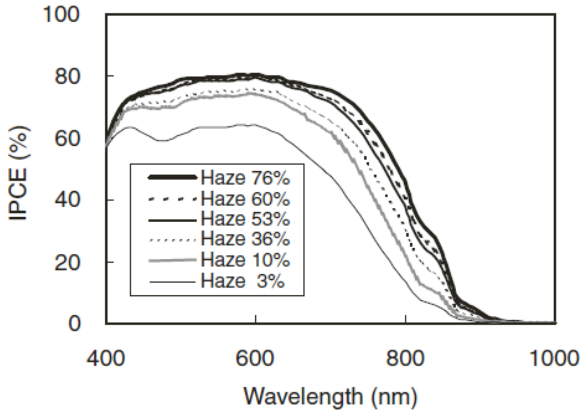

Figure 4.9 IPCE vs wavelength of TiO_2 films with six different Haze factor values

to-Current Efficiency (IPCE) enhances until achieve a value at which the increase in Haze factor does not correspond to a significant increase in the IPCE.

This could mean that after a certain Haze factor value, the chemisorbed dye is not able to absorb a higher quantity of incident light. After the measurement of LHE, the maximum expected photocurrent was calculated with formula exposed in Par.3.2.3. I assumed EQE equal to one, which means that for each incident photon, an electron is generated. This is an ideal case that gives us the maximum limit of our device. For the specimen with only TiO_2 the maximum expected photocurrent was 6.42mA/cm^2, while for that one with also the Al_2O_3 layer was 8.01mA/cm^2. There is a difference of about 20% given by the difference in the LHE at 600-700nm. This could mean that the alumina layer, with its increasing in Haze factor, helps the light absorbance by die particles at higher wavelengths.

4.1.4 TiO_2 photo-anode deposited by PA-SSJD

After the characterization of material deposited by PLD, my work was to optimize the various parameters of PA-SSJD reactor prototype, trying to obtain the same TiO_2 morphologies deposited by PLD in less time and on larger area. Since it is a prototype, I (in collaboration with Giorgio Nava) started from scratch and we spent some time to stabilize the flux of precursor in the reaction chamber, studying the new system of TTIP injection (Par.3.1.3). We fabricated specimens in four different relevant situations, changing the Ω parameter that is the ratio between the Mach disc length and the distance slit-sample. We deposited specimens with the sample holder into the Mach disc, one with the sample at the end of Mach disc and the last two specimens out of the zone where the flux is supersonic. These are the first analysis on TiO_2 deposited with this reactor so it is a first screening of PA-SSJD potential.

4.1.4.1 TiO_2 Deposition by PA-SSJD

FTO sheet was cut in plates with area 20mm x 15mm, cleaned with the above descripted procedure and masked with Kapton-tape leaving a free area of 10mm x 10mm, as represented in Fig.4.10, where TiO_2 film is deposited.

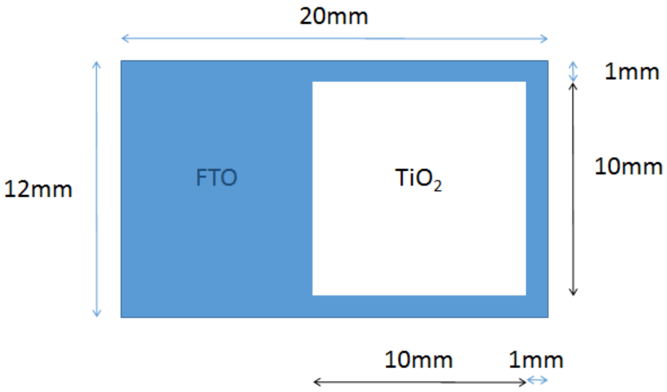

Figure 4.10 Schematic of the FTO glass substrate for TiO2 deposition by PA-SSJD

For all depositions, we kept constant the radio frequency (RF) power at 80W. The deposition was in an argon-oxygen atmosphere, with a ratio of 10:1. The reaction chamber was at 80Pa and deposition chamber at 10Pa, the slit that divided the two chamber was of area 100mm x 0.5mm. During the deposition, TTIP was heated at 59.3°C. The substrates holder, during the deposition, swept along x-axis with a velocity of 5.7mm/s on a distance of 40mm. In this way, it was possible deposit homogeneously on a large area. As explained in Par.3.1.3, moving the sample holder along y-axis, it is possible to obtain different morphology. We deposited at different Ω (ratio between the distance slit-substrate and the leght of Mach disc) that are resumed in Tab.2. In the same table are exposed also the distance substrate-slit (length of Mach disc is 11.4mm) and the thickness of deposited films.

Table 4.1 Distance substrate-slit and film Thicknesses for each value of Ω

Sample	Ω	Substrate-slit [mm]	Thickness [μm]
D162	0.75	8.55	4.6
D158	1	11.4	5.4
D155	1.25	14.25	4.8
D165	1.5	17.1	5.8

After deposition process, samples were annealed in furnace at 500°C for 2hs to achieve the crystalline transition in TiO_2 from amorphous form to the Anatase phase.

For the characterization measurements, some samples for each Ω values underwent a dye loading and unloading process, above exposed.

4.1.4.2 Morphological characterization

The first step was to characterize the morphology of TiO_2 deposited by PA-SSJD and compare it to that obtained with PLD technique. We began fabricating a specimen with Ω factor equal to one, so the sample was at the end of the Mach disc (Fig.4.11).

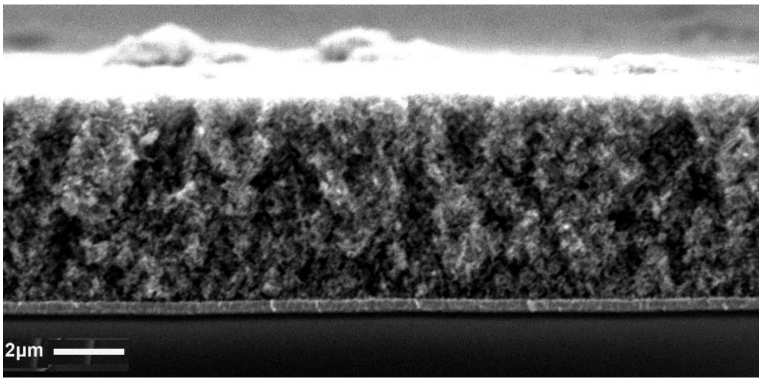

Figure 4.11 Cross section SEM image of TiO_2 film deposited by PA-SSJD with $\Omega=1$

In Fig.4.11, the morphology of film is not similar to the forest-like structures deposited by PLD (Fig.2.11), but it is similar to that one in Fig.3.3-d deposited by TiO_2 paste. It is not hierarchically ordered, but it seems a sponge. Observing the top view image, this fact is confirmed, the surface is not smooth but very rough (Fig.4.12).

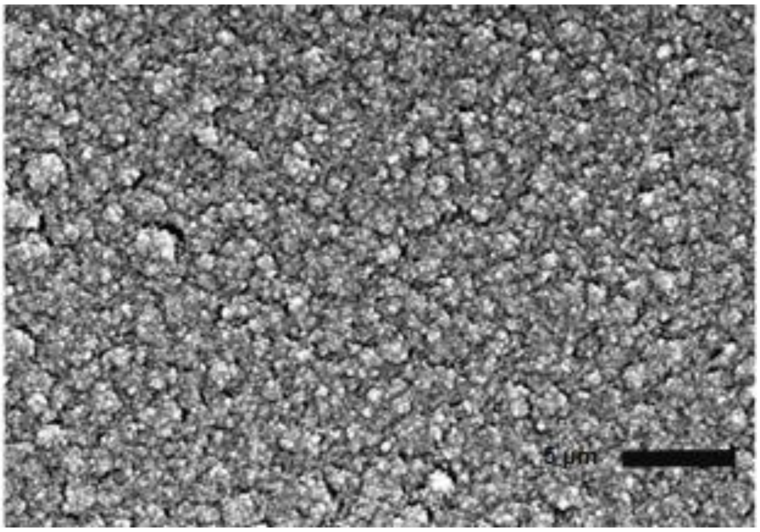

Figure 4.12 Top view SEM image of TiO2 film deposited by PA-SSJD with $\Omega=1$

After this first deposition, we investigated what happens when deposition occurs with sample into the Mach disc. The result is in the Fig.4.13.

Film deposited with value of Ω of 0.75 has the same morphology of that one deposited at Ω equal to 1. It is a porous layer without a clear hierarchical structure. In this case, it seems more compact of the previous one. Since the specimen is into the Mach disc

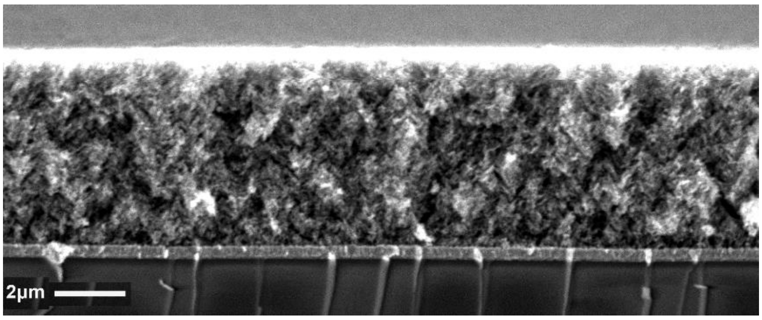

Figure 4.13 Cross section SEM image of TiO2 film deposited by PA-SSJD with Ω=0.75

during the deposition process, the nano-clusters have a higher kinetic energy when they come in contact with the substrate and they pack in a less porous structure.

This characteristic is confirmed also analysing the top view image of this specimen (Fig.4.14). The surface is always rough, but, respect to the specimen in Fig.4.12, it seems more smooth.

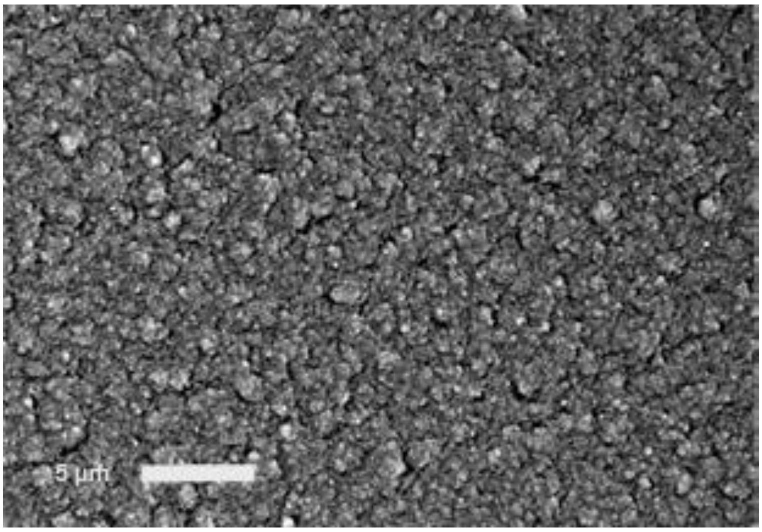

Figure 4.14 Top view SEM image of TiO2 film deposited by PA-SSJD with Ω=0.

After these two deposition respectively, one at the end of Mach disc and the other into the Mach disc, we performed the morphology analysis of a specimen deposited out of Mach disc, with a value of Ω of 1.5. At this distance, the nano-clusters have less kinetic energy, so we aspect a more porous and hierarchical morphology (Par.3.1.3). This fact is assumption is confirmed by Fig.4.15.

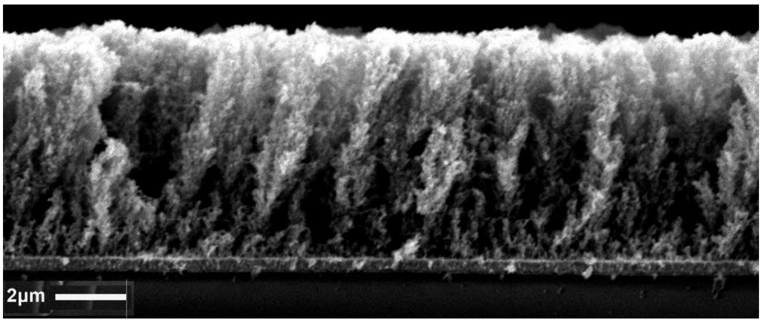

Figure 4.16 Cross section SEM image of TiO2 film deposited by PA-SSJD with Ω=1. 75

In this case, It is evident a certain similarity with the TiO_2 forest of Fig.2.11, but they are not compact as in Fig.3.3-e-f-g, they are very porous respect them, and this fact is confirmed observing the top view image (Fig.4.16).

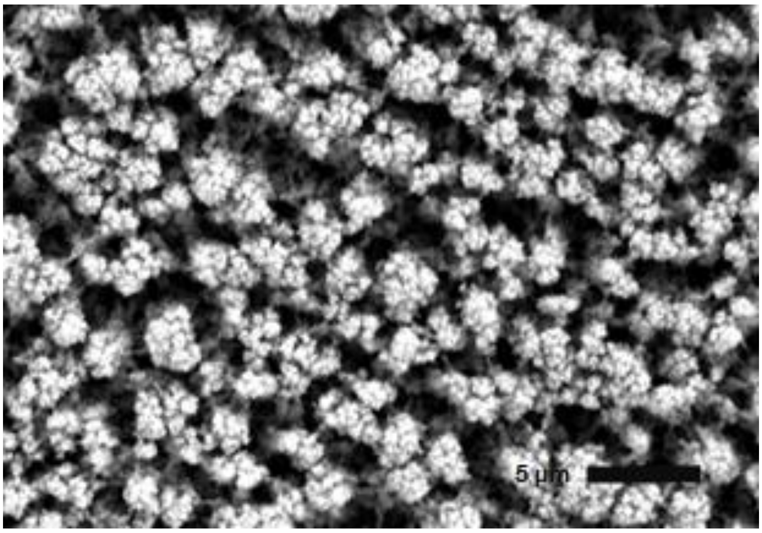

Figure 4.15 Top view SEM image of TiO2 film deposited by PA-SSJD with Ω=1.5

Since specimen deposited at Ω equal 1.5 was too porous but had a tree like morphology, while that one deposited with a value of Ω equal to one had not a defined nanostructure but was more compact, we decided to investigate the condition in the middle of the previous. Taking the sample in the way to be at a value of Ω of 1.25, we deposited the last specimen for this first analysis. Observing the SEM image (Fig.17) is possible to note that the tree structures of Fig.4.15 are still present but the

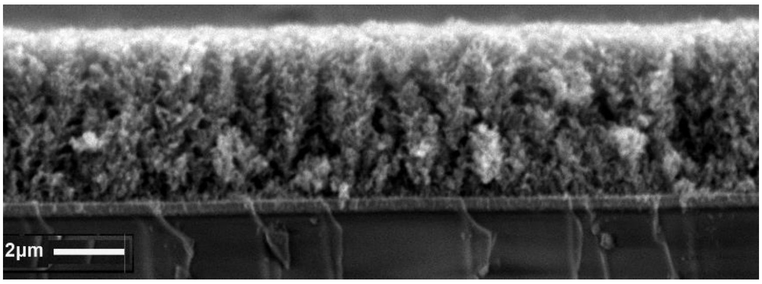

Figure 4.17 Cross section SEM image of TiO2 film deposited by PA-SSJD with Ω=1.25

morphology is more compact respect to that one of specimen deposited at Ω equal to 1.5.

The top view image (Fig.4.18) give us a confirm of this fact, the “end of the trees” are still present but they are not so separated from each other as in Fig.51.

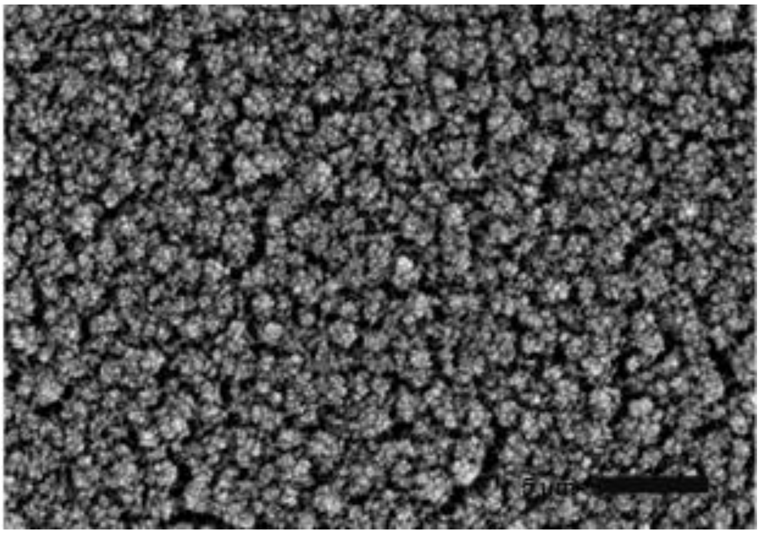

Figure 4.18 Top view SEM image of TiO2 film deposited by PA-SSJD with Ω=1.25

4.1.4.3 Raman Characterization

The second step was to control if, after the annealing process, we obtained Anatase phase. To do that, we analysed the specimens with Raman spectroscopy. In Fig.4.19, there is the typical Raman spectrum of TiO_2 deposited by PLD. The four peaks typical of Anatase phase are evident at 144, 399, 519 and 639cm^{-1}.

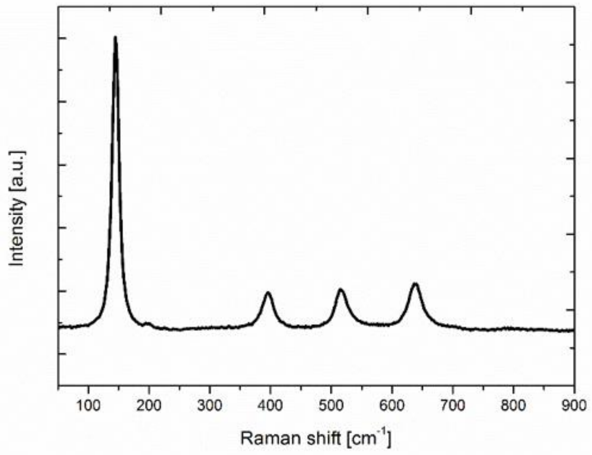

Figure 4.19 Raman spectrum of TiO2 substrates deposited by PLD whit a thickness of 30μm

In Fig.4.20, it is possible to observe the Raman spectrum of our specimen deposited with Ω equal to 1.

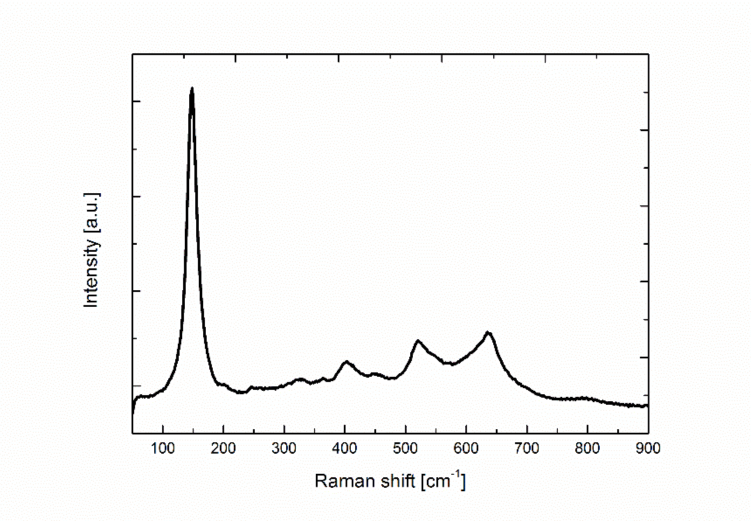

Figure 4.20 Raman spectrum of TiO2 substrate deposited by PA-SSJD with Ω=1

The peaks at 144cm^{-1} is perfectly evident, the other three are not so sharp as in the previous image, but they are present, so we can say that it is surely TiO_2.

The reason of this lack of sharpness of the three peaks is the presence of FTO. In fact, observing Fig.4.21, where TiO_2 spectrum of our specimen and a common FTO Raman spectrum are compared, we can observe that FTO has two characteristic peaks, one at 600cm^{-1} and the secondo at 1100cm^{-1}. The TiO_2 film is so thin and porous, that the below FTO interferes and distorts the Raman spectrum.

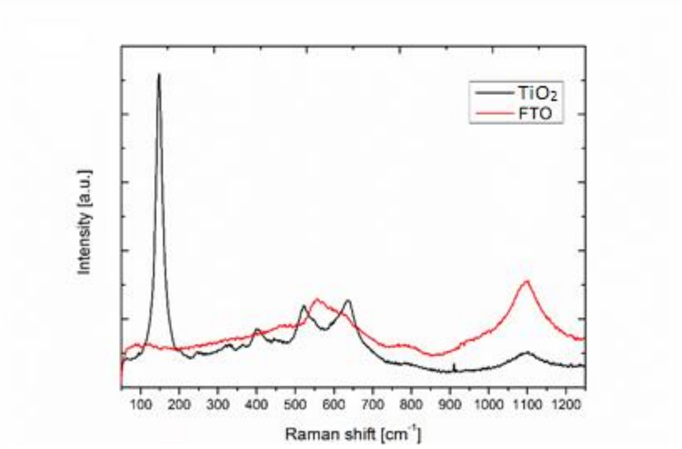

Figure 4.21 Raman spectrum of TiO2 substrate deposited by PA-SSJD with Ω=1 and commercial FTO glass substrate.

In fig.4.22, we can observe that all the specimens have similar spectrum between them. The difference is in the intensity, it decreases with the increasing of Ω parameter. This fact could be attributed to the higher porosity of specimen deposited out of the Mach disc.

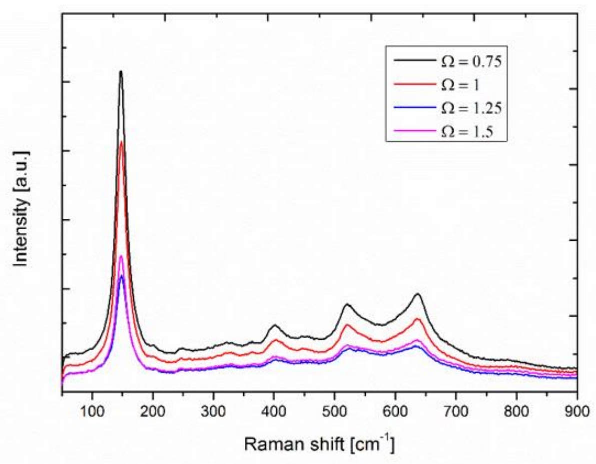

Figure 4.22 Raman spectra of TiO2 substrate deposited by PA-SSJD with different values of Ω

4.1.4.4 Optical properties

After the morphological characterization and established by Raman analysis that the deposited TiO$_2$ was in Anatase phase , we analysed the specimens by UV-Vis spectroscopy to explore how our material interacts with the light, in order to use them as photo-anode in a DSSC. The procedure is the same descripted in Par.4.1.3.

Firstly, we calculated the Haze factor of different depositions. The results in Fig.4.23 show the Haze factor trend from the NIR to high UV spectrum.

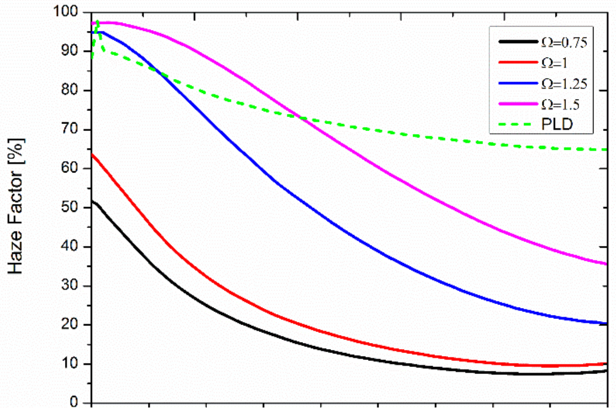

Figure 4.23 Haze factor of TiO2 deposited by PLD with different Ω conditions. Dot line is the Haze factor of TiO2 deposited by PLD.

It is immediately evident that the samples with the forest morphology have a higher scattering power than that with the more compact and disordered structure, specially going to UV wavelengths. It would seem that nanostructured film having a better light management. Comparing the Haze factor of specimen deposited by PLD with those of samples at high Ω value fabricated by PA-SSJD reactor, we note that the values are similar from 500nm to 350 nm, but in the rest of the spectrum there is a big difference between them. This fact is probably due to the high porosity of PA-SSJD reactor specimens, that, in contrary of more compact structures deposited by PLD, lead a path for the light more free.

To investigate which is the real light management of our samples, we calculate the Light Harvesting Efficiency (LHE). The results are shown in Fig.4.24.

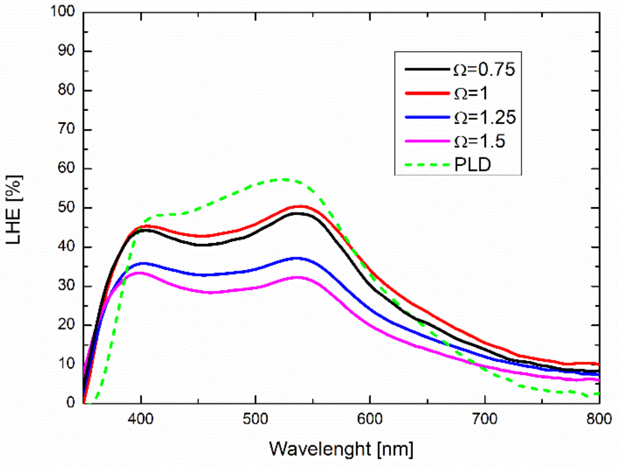

Figure 4.24 Light Harvesting Efficiency of TiO_2 deposited by PA-SSJD with different Ω conditions. Dot line is the LHE of TiO_2 deposited by PLD

Respect to the Haze factor, LHE follows a different trend. In this case, the forest-like structured specimens show a worse light management respect to the not-nanostructured samples. This fact can be explained with the help of Roughness Factor (RF). As explained in Par.2.2.1.1, RF is the ratio between the total surface and the projected surface and represent the area available for the dye chemisorption. In Par.3.2.3, we explained how to extrapolate it from the absorbance.

In Fig.4.25, are represented the different RF values obtained for each Ω values. The RF values are summarized in Tab.4.2.

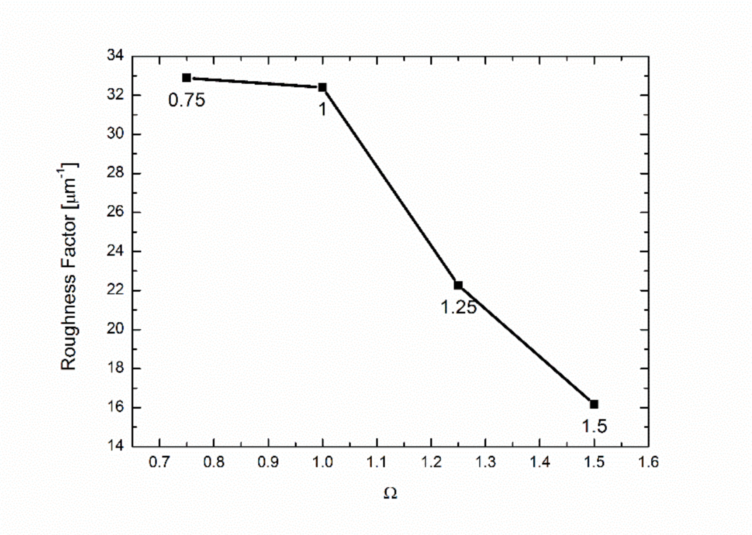

Figure 4.25 Roughness factor of TiO2 deposited by PA-SSJD with different values of Ω.

Table 4.2 Values of Roughness Factor obtained for each Ω value.

Ω	RF [µm^{-1}]
0.75	32.89
1	32.41
1.25	22.26
1.5	16.17

As for the LHE, also for RF the values are higher for lower Ω values. This means that the specimens with forest morphologies (deposited at Ω=1.25 and Ω=1.5) are too porous for a good chemisorption of the dye. This fact affects also the LHE, because with less chemisorbed dye obviously the dye light absorbance is lower.

Respect to the TiO_2 deposited by PLD in hierarchically ordered structures, the titania films deposited by PA-SSJD reactor have a really low RF. In fact, Passoni et al. (2013)[75] obtain values of Roughness Factor of about 80µm^{-1} that is more than double respect to our PA-SSJD reactor specimens. This means that also the morphologies obtained at low Ω values are not enough compact to lead a good dye chemisorption.

Using the LHEs obtained, we can calculate the maximum expected photocurrent, as explained in Par.3.2.3. Results are summarize in Tab.4

Table 4.3 Values of max expected photocurrent calculated for each value of Ω

Ω	Max photocurrent [mA/cm^2]
0.75	3.29
1	3.61
1.25	2.54
1.5	2.00

In Fig.4.26, it is possible to compare the trend of Roughness Factor with the max expected photocurrent.

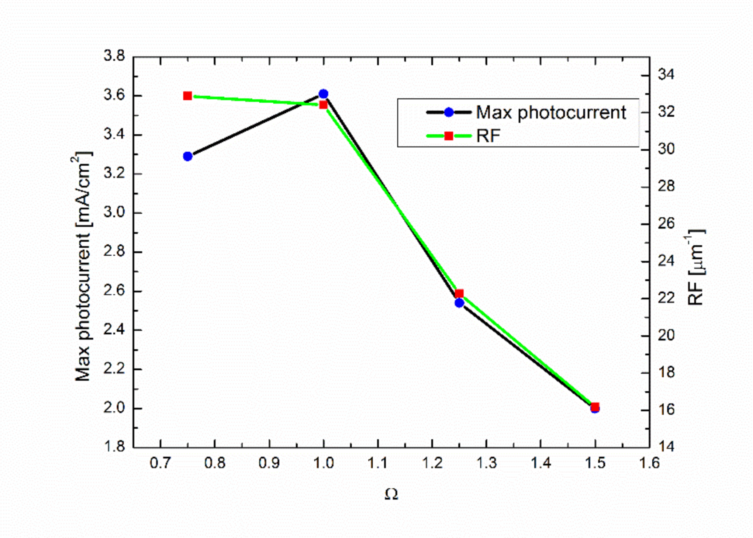

Figure 4.26 Max expected photocurrent and Roughness Factor of TiO2 deposited by PA-SSJD with different values of Ω

The two parameters are connected because RF gives an indication of area available for dye chemisorption, then higher is the RF value, higher is dye chemisorbed and the LHE of the specimen. All this leads to an higher value of max expected photocurrent.

Comparing the max photocurrent values obtained with PA-SSJD reactor and with PLD, we find that the differences that we observe in the RF values (about 20-40%) are almost the same for the photocurrent values (30-50%).

In the light of this big difference between values of RF obtained by PLD and PA-SSJD, we decided to not fabricate DSSC with photo-anode deposited by PA-SSJD during this work of thesis. The RF values are too low to obtain a functioning device. The fabrication of a device by PA-SSJD will be possible after a more precise development of the reactor.

4.2 Counter electrode

Making reference to Par.2.2.2, counter electrode's function is to produce I_3^-, taking electrons from the external circuit and promoting the following reaction mechanism on its surface:

$$(a)\; I^- + Pt \rightleftarrows I^-(Pt)$$

$$(b)\; I^-(Pt) \rightleftarrows I(Pt) + e^-$$

$$(c)\; I(Pt) + I(Pt) \rightleftarrows I_2 + 2\mathrm{Pt}$$

$$(d)\; I_2 + I^- \rightleftarrows I_3^-$$

Invoking the Par.2.2.4, I^- is the result of dye reduction by triiodide and is in concentration ration 9:1 respect to the I_3^-, in commercial electrolyte. The (a) step is the adsorption of iodide on platinum. (b) is the oxidation of iodide. (c) and (d) are respectively the I_2 and I_3^- production. Then triiodide diffuses from counter electrode, through the electrolyte, to the dye particles chemisorbed on the photo-anode. In our case, counter electrode is not the usually Pt layer deposited on a TCO, but is a platinum loaded carbon film deposited on the alumina spacer. It is crucial that there is not electric contact between the TiO_2 photo-anode and the counter electrode, to avoid a short circuit that causes a malfunction of the device, with the loss of generated photocurrent. Another important feature is that the counter electrode should connect the two electrodes into which is divided the FTO substrate in monolithic configuration (Fig.2.19). Moreover, it should be porous to ensure a correct percolation of electrolyte.

In this paragraph, we investigate how the presence of carbon, instead of the usual only Pt layer, could affect the counter electrode performances, above all, whether the surface has a low resistance or not. This is a main feature to have a good electrons conductance from the external load to the counter electrode/electrolyte surface. Moreover we try to achieve an optimum in ratio Pt:C, using less platinum as possible to reduce the costs.

4.2.1 Carbon-Platinum co-deposition by PLD and Magnetron Sputtering

For the study about carbon platinum counter electrode optimization, we fabricated two different kinds of sample.

The first one was used for Hall effect analysis. An FTO substrate was etched drawing a cross, as we can see in Fig.4.27.

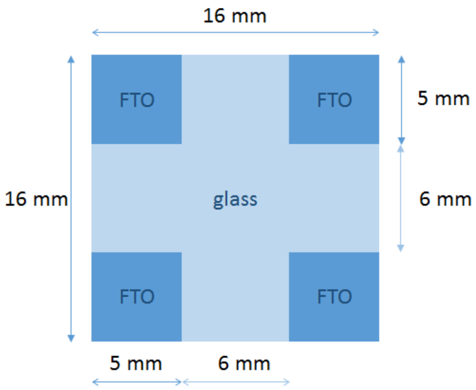

Figure 4.27 Schematic of the glass substrate after the etching for Hall effect characterization

Substrates etching, to remove FTO from the glass, was done using zinc powder as catalyst and 1:4 hydrochloric acid as the etching agent.

These substrates were subsequently cleaned (Par.4.1.1) and masked with a free area of 10mm x 10mm so that the deposited film cover the central part in glass of the specimen, overlapping also on four angles of FTO squares (Fig.4.28).

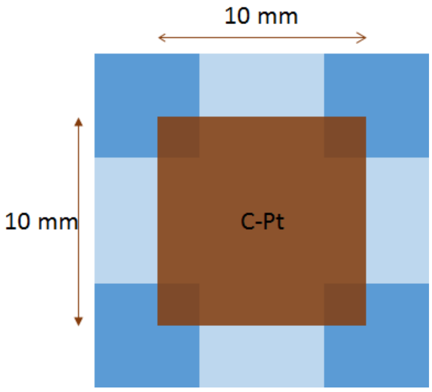

Figure 4.28 Schematic of the glass substrate after C-Pt deposition for Hall effect characterization

In this way, it was possible connect the four tips of the Hall effect instrument in van der Pauw configuration (Par.3.2.5) on the FTO squares, without scratching the deposited film, and they are electrically connected to the carbon platinum film (Fig.4.29).

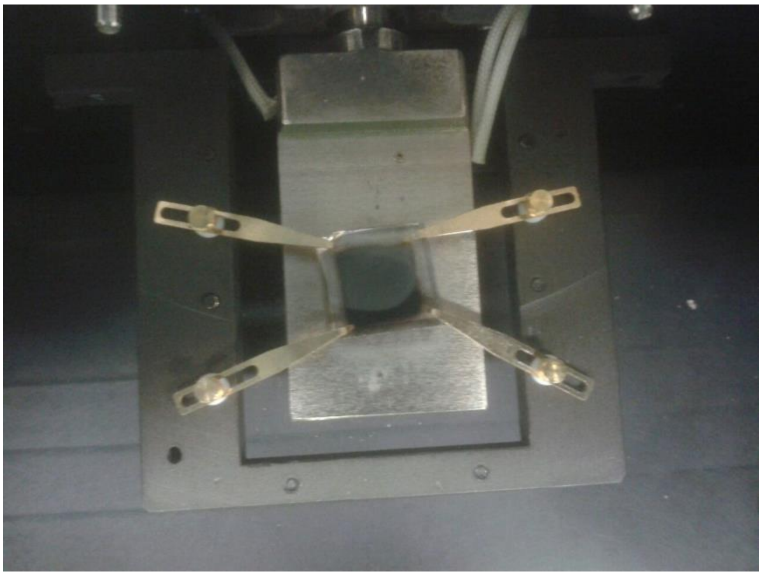

Figure 4.29 A carbon platinum resistivity measurement with van der Pauw method: the four gold points rest on the FTO “contacts” close to the C-Pt film.

The second substrate kind was a silicon wafer used for Raman spectroscopy characterization.

All the substrates, after the eventual etching, were cleaned with the above descripted procedure (Par.4.1.1). Silicon wafers were cleaned only by oxygen plasma treatment, without use of organic solvents, because they were already clean when were fabricated. Carbon platinum films were deposited by a co-deposition, Pt by magnetron sputtering and C by PLD. We did eleven runs of deposition, changing some parameters in each deposition. We kept constant the laser energy (500mJ), the repetition rate (20Hz), the substrate rotation (48rpm) and the background argon atmosphere pressure (9Pa).

First of all, we fabricated samples with different Pt load but maintaining constant the quantity of carbon. To do it, we changed the magnetron sputtering power between different depositions. We exploited the difference in pulses frequencies of PLD and magnetron sputtering. PLD emits a pulse of 15ns with a frequency of 20Hz, while sputtering has a frequency of 50kHz. If I maintain constant the number of pulses of PLD (4500) and magnetron sputtering, and then the thickness of the film, I can ablate more or less material from Pt target increasing or decreasing the power supplied. In Tab.4.4 are resumed the different magnetron sputtering powers used for depositions.

Table 4.4 Magnetron sputtering power for different fabricated samples

Sample	Power [W]	Pt %wt
C/Pt 026	20	3
C/Pt 028	7	1.01
C/Pt 029 (Pt reference)	7	100
C/Pt 030 (C reference)	0	0
C/Pt 034	30	4.5
C/Pt 035	40	6

C/Pt 029 and C/Pt 030 were used as Pt and C reference for the characterization.

For second step, we took constant power of magnetron sputtering (20W), frequencies of sputtering and laser, but we changed number of pulses. In this way, we kept constant the ratio Pt/C in weight and changed the thickness of films. In Tab.6 are resumed number of pulses and thickness of deposited films.

Table 4.5 Number of PLD pulses and thickness of films

Sample	N° pulses	Thickness [nm]
C/Pt 026	4500	100
C/Pt 031	9000	200
C/Pt 032	2250	50
C/Pt 033	1125	25

These two steps concern the study for the optimization of carbon platinum counter electrode co-deposited. The third step concerns only the investigation about conductivity of porous film in carbon with different thickness. As in the previous run, to change thickness just increases or decreases number of pulses with PLD. Argon pressure was the same (9Pa), also frequency (20Hz) and laser energy (500mJ). In Tab.4.6 are resumed number of pulses and thickness of deposited carbon substrates.

Table 4.6 Number of PLD pulses and carbon film thickness

Sample	N° pulses	Thickness [μ m]
C/Pt 036	225000	5
C/Pt 038	45000	1

4.2.2 Carbon-Platinum Morphology Characterization by SEM

The first step in our investigation was to have an idea of how is the morphology of co-deposited carbon-platinum counter electrode, so we performed a SEM analysis. The carbon-platinum film is composed by not organized nanoparticles, with size on the order of hundreds nanometers (Fig.4.30).

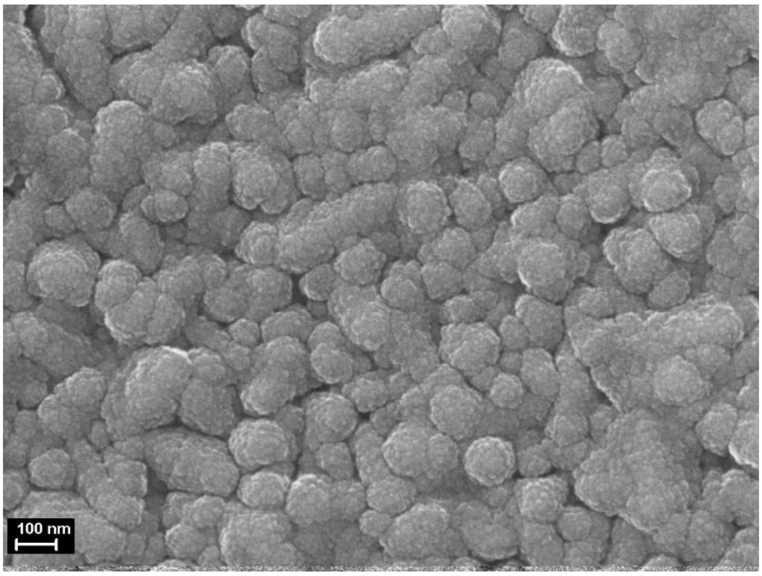

Figure 4.30 Top view SEM image of C-Pt film co-deposited by PLD and magnetron sputtering in Ar atmosphere at 7Pa with a thickness of 100nm

Comparing Fig.4.30 with other SEM images present in literature[105] of carbon platinum film, it possible to note that in our specimen platinum particles are not seen, while in Fig.4.31 the brighter clusters are Pt particles aggregates.

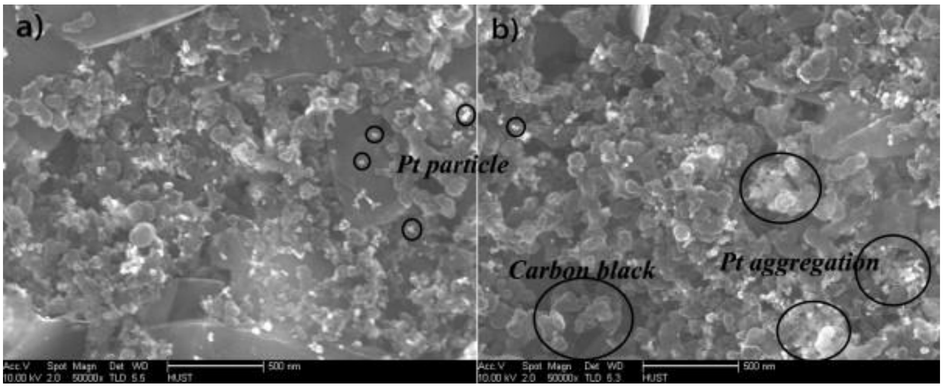

Figure 4.31 SEM image of SEM images of mesoscopic platinized carbon electrode with 0.5 wt.% (a) and 3 wt.% (b)

Since the SEM instrument used by us to perform this measurement has a maximum resolution of two nanometers, we could hypotize that, in our substrate, there is a high dispersion of platinum particles with size of less than 2nm into the carbon matrix. This could be an interesting characteristic, because, in this way, it is possible to take advantage of all particle surface to enhance the catalytic power, while in platinum clusters of Fig.4.31, this compound formation could lead up to a decreasing in total surface area available for catalytic reaction and then to an efficiency loss.

4.2.3 Raman analysis of co-deposited carbon-platinum film.

Raman spectroscopy is a good instrument to have an idea about the material composition. In this case, we investigated in which phase is present the deposited carbon and if there are C-Pt bonds. Raman spectra of carbon thin films is the first analysis to can differentiate the different carbon allotropes [106]. Fig.4.32 shows the main carbon allotropes, they are characterized by carbon-carbon bond (C-C) orientation, degree of crystallinity and hybridization state (sp^2 or sp^3).

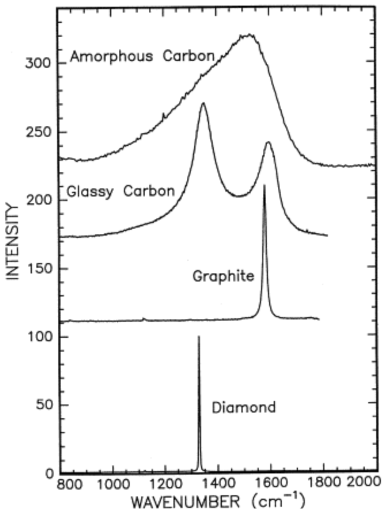

Figure 4.32 Examples of Raman spectra for principal carbon allotropes.

Watching the glass carbon spectrum in Fig.4.32, it is characterized by the presence of two broad bands. The peak in correspondence about 1580cm^{-1} is named G and is associated with the tangential C=C stretch or tangential displacement mode having E_{2g} symmetry. This mode is characteristic of large single-crystals graphite hybridized sp^3, which tend to have a high regular structure composed by hexagonal network plane with a low level of impurities and defects[107]. The other band is named D and is the disorder-activate band having A_{1g} symmetry in the first-order scattering process. It is characteristic of sp^2 sites in hexagonal rings in amorphous non-planar structure[108]. The D band arises from the presence in the material of in-plane substitutional heteroatoms, vacancies, grain boundaries and other defects[107]. The presence of these defects affects the grain size of graphite crystals, which are smaller, and disrupt the transitional symmetry, creating a certain “disorder” in the material. We will see in the next paragraph how the presence of sp^2-bonded carbons with various degree of graphitic order affects the carbon conduction characteristics. In a typical analysis of carbon Raman spectrum, the ratio I(D)/I(G) is a way to investigate how much disorder is present in the material and, then, the relative characteristic of the film.

We began analysing our specimen with 5μm of only carbon deposited by PLD, because its thickness should guarantee the absence of Raman signals from Si substrate. Fig.4.33 shows the spectrum, where there are the two characteristic bands.

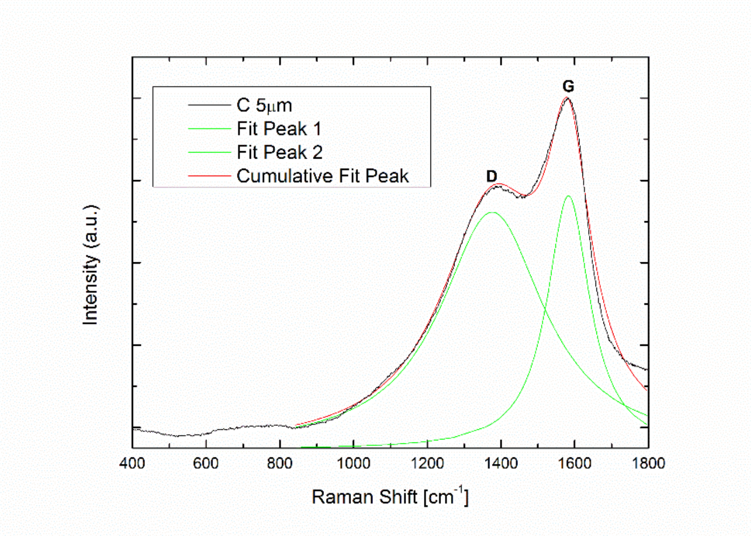

Figure 4.33 Raman spectrum of carbon film deposited by PLD with a thickness of 5μm. Green lines are the fit of D and G peaks, red line is the cumulative fitting.

To obtain the intensity of the bands and the position of peaks centre, we fit the spectrum with two Lorentzian curves. We obtained that G-band’s peak has 1583cm^{-1} as centre, while D-band’s peak is at 1376cm^{-1}. These values agree with that find in literature[108]. The I(D)/I(G) ratio is equal to 2.29, this means that the material is mainly composed by “disordered” small-crystal graphite and there could be the presence of defects in the structure.

We compared sample with 5μm of only carbon with a specimen where there were co-deposited 200nm of carbon (by PLD) and 3%wt of platinum (by magnetron sputtering). The aim was to observe if the different thicknesses lead to a difference in the carbon structure. Moreover, we wanted to investigate how the presence of platinum affects the carbon structure and if there C-Pt bonds.

In the Raman spectrum showed in Fig.4.34, it is possible to note a certain difference with the previous one in Fig.4.33. The main difference is the quasi-disappearance of D-band, while G-band is always presents. Moreover, the shape of the curve is quite similar to that one of amorphous carbon in Fig.4.32. After the peaks fitting, we obtained that G peak shifted at 1552cm^{-1} while D peak shifted at 1350cm^{-1}. This could mean that the presence of Pt leads to a higher disorder in the structure.

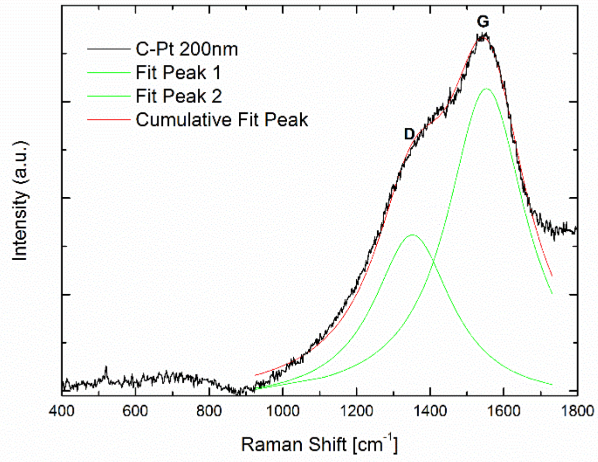

Figure 4.34 Raman spectrum of carbon film deposited by PLD with a thickness of 200nm. Green lines are the fit of D and G peaks, red line is the cumulative fitting

Comparing the two spectra, we would not found indications about possible C-Pt bonds in the second one, so we could suppose that the film is composed by platinum particles embedded in a carbon porous matrix. This fact would confirm the hypothesis done above, when, in the SEM image (Fig.4.30), we do not note the presence of Pt particles with size higher than 2nm.

After a week, in which samples were left in air, we performed the same Raman characterization (Fig.4.35).

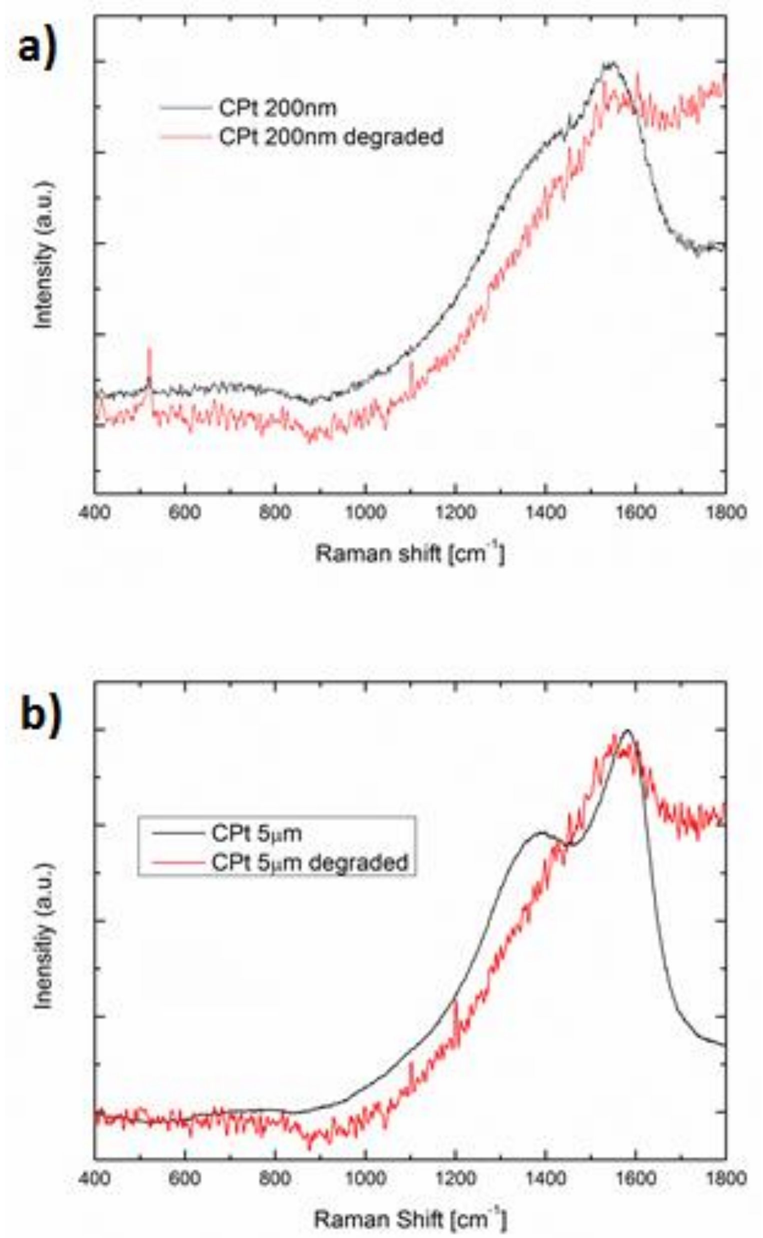

Figure 4.35 a)In black Raman spectrum of C-Pt counter electrode with a thickness of 200nm. In red, Raman spectrum of the same specimen taken a week after the previous measure. during the week the samples has been left in the air. b)In black Raman spectrum of C counter electrode with a thickness of 5μm. In red, Raman spectrum of the same specimen taken a week after the previous measure. During the week the samples has been left in the air.

In both cases, the spectrum was not the same. The two bands, D and G, were disappeared and were substituted by an only big band. The shape is similar to that one of amorphous carbon in Fig.4.32. This fact could be attributed to a degradation process due to oxidation and adsorption of humidity and contaminations, which could break down the crystalline structure.

In conclusion, we deposited a disordered carbon with a certain quantity of nanometric graphite inclusions when the thickness is higher.

4.2.4 Electrical Characterization of co-deposited C-Pt through Hall effect measurements

After the structural analysis, the next step was to characterize the electrical properties of our material. In order to do so, we performed measure with a Hall effect measurements system. With this method, it is possible measure three main factors. The first one is the bulk concentration, which gives the number of electric carriers in volume of material. This parameter is important because leads to understand which is the kind of carriers (electrons or holes) and if the material is a metal, a p/n semiconductor or an insulator. The bulk concentration of a material depends on the electronic band structure. In a metal, valence band and conduction band are not divided. In this way, the metal atoms are surrounded by an electron cloud that is common to all the material and makes a metal a good electric conductor. The carrier concentration in a metal is very high, in the order of $10^{22}cm^{-3}$ electrons. Instead, an insulator has the valence band and the conduction band that are separated by a high energy band gap. In this way, an electron needs a high energy to pass from the valence band to conduction one and give a current. For this reason, the bulk concentration is about $10^{11}cm^{-3}$[109]. These are the extreme cases; in the middle, there are the semiconductors.

For semiconductors, the electronic bands are divided, but the energy gap is not so high. This fact allows to some carriers to pass from an occupied band to the other, which is free. In this way, these materials have a bulk concentration of about $10^{18}cm^{-3}$, an intermediate value compared to the previous one. Semiconductors can be of three different types. A n-type semiconductor has a current band with an energy near to the Fermi level, this fact makes possible to electrons in valence band to pass in the conduction band and create a current. The p-type semiconductors has the opposite characteristic, the valence band is near to Fermi energy and, in this case, the holes present in valence band are the charge carriers. An intrinsic semiconductor material, the main one is silicon, follows a behaviour that depends on what kind of doping suffers. For example, if Si is doped with an atoms with five electrons in the external shell (as P or As), the presence of an extra electron lead to an increasing in number of conduction electrons, because the valence band is totally occupied, and then to creation of a current. This doping process is the n-type.

The Hall effect measurements system gives the value of bulk (or carrier) concentration and its sign indicates which is the type of carriers. In our case, the sign was negative; this means that the carriers were electrons. As a matter of convenience, the dates were plotted with positive sign.

Fig.4.36 shows the bulk concentration as a function of the percentage by weight of platinum. On the right there are the reference materials, platinum (thickness of 32 nm), commercial FTO (thickness of 250nm) and platinum bulk. For platinum bulk the values reported of bulk concentration is taken from literature ad an indicative value for precious metals, as Ag or Au[110]. Comparing the bulk concentration of platinum (about 10^{22}cm^{-3}) and carbon (about $6\cdot10^{17}$cm^{-3}), it is immediately evident the difference between the two materials. The second has the carrier concentration of semiconductors. Moreover, observing the graphic, it is interesting to note that, increasing the Pt load, the carrier density increases until to achieve a maximum value, when the Pt is 3% wt. After this value, the density of carriers is constant. This means that when the Pt load exceeds the 3%wt, the dominant material is the platinum, which gives a high number of free electrons. Below that value, the carrier concentration is dominated by carbon and there are less free electrons.

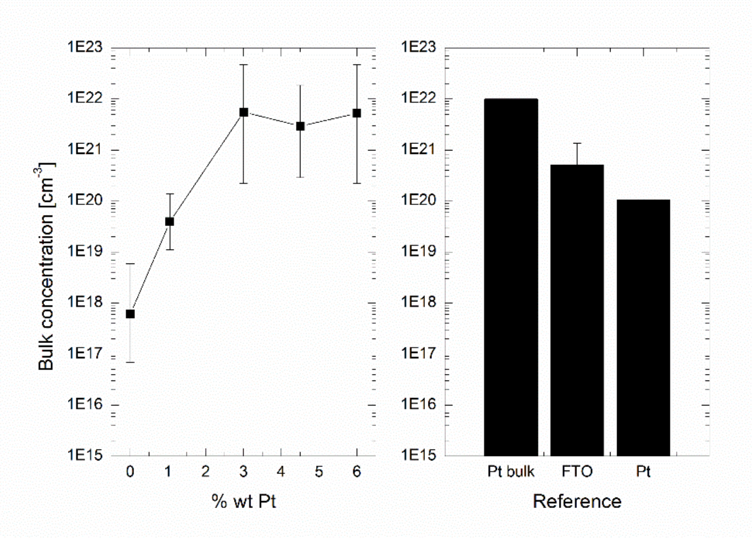

Figure 4.36 Left: bulk concentration respect to the Pt percentage deposited in the film. Right: bulk concentrations for three reference, FTO, Pt bulk and Pt sputtered with a thickness of 32nm

Noted this trend, the next step is to fix a Pt load (in our case 3%wt) and change the thickness of the carbon platinum film. The results are shown in Fig.4.38.

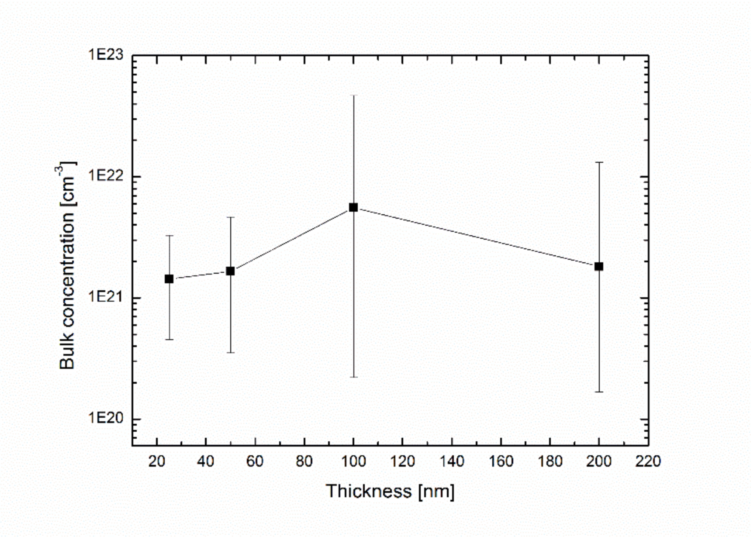

Figure 4.37 Bulk concentration respect to thickness of C-Pt film, with the same ratio Pt:C (3% wt)

The bulk concentration does not change, varying the thickness of C-Pt layer. The presence of Pt in the same percentages in each sample leads a constant trend of charges concentration. The reason could be attributed to the fact that thicknesses change of few nanometers, this means that the difference in volume is very low compared to carrier concentration which is expressed in cm^{-3}. If the difference in volume are higher, for example in order of microns, it is possible to observe an increasing in bulk concentration. Fig.4.38 shows the bulk concentration as a function of only carbon film thickness.

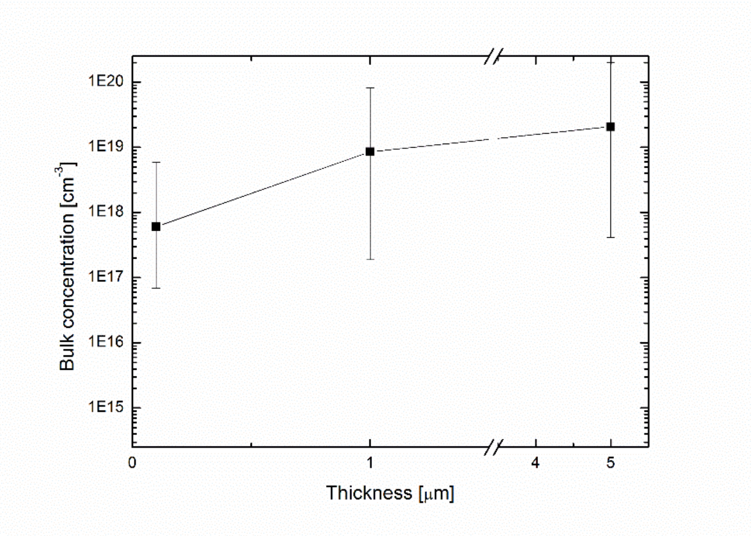

Figure 4.38 Bulk concentration respect to thickness of only C film.

The charges concentration increases by an order of magnitude passing from 100nm to 1μm, then it arrives at saturation and the value remains constant. The reason of this trend could be explained with the same hypothesis expressed before: with the passage from nanometers to micrometers bulk concentration increases of an order of magnitude. When the difference between the two thickness is low, the volume is almost the same and the carrier concentration to change significantly.

After the bulk concentration, the second main parameter is the mobility of carriers. The mobility is the indicator of how quickly a charge carrier can move through a material when is dragged by an electric field. Metals and electrical conductors in general have a high mobility, in accordance of their electronic band structure. As we said before, in this type of materials the conduction electrons are not localized on a specific atom, but are delocalized and makes an electron cloud, which leads a good mobility.

In Fig.4.39, it is possible to note the really high difference between mobility of Pt (bulk and thin layer) and FTO and the carbon-platinum and only carbon film. In latter, mobility could be affected negatively by the porous structure of the film and presence of defects. When an electron meets a hole, a recombination process happens, in which electron loses an amount of energy larger than the band gap with emission of thermal energy (in form of phonons) or radiation (in form of photons). Defects, impurities and dislocations could act as traps for electrons and holes present in a semiconductor, in this way the mobility decreases because carriers are trapped and recombine.

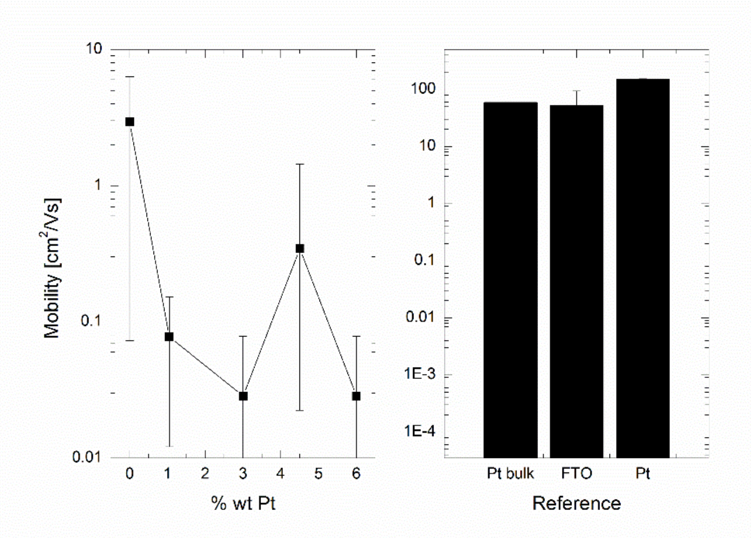

Figure 4.39 Left: mobility respect to the Pt percentage deposited in the film. Right: mobility for three references, FTO, Pt bulk and Pt sputtered with a thickness of 32nm

Maintaining fixed the ratio Pt:C at 3% wt, the mobility, for different thicknesses, has a constant low value, to confirm the previous hypothesis.

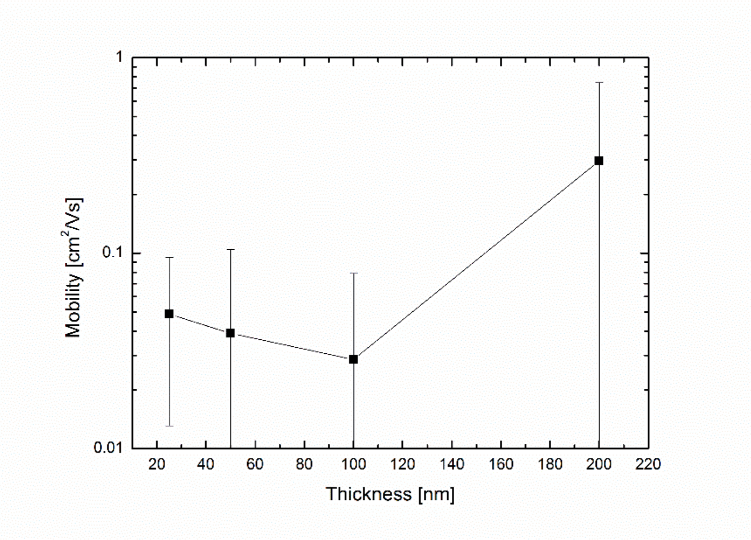

Figure 4.40 Mobility respect to thickness of C-Pt film, with the same ratio Pt:C (3%wt)

In only-carbon layers, the mobility follows a different trend respect to the previous samples. At higher thicknesses, the mobility is lower, and increases with decreasing thickness. This behaviour could be explained with a higher presence of traps and defects due to a higher quantity of disordered material, as seen by Raman characterization.

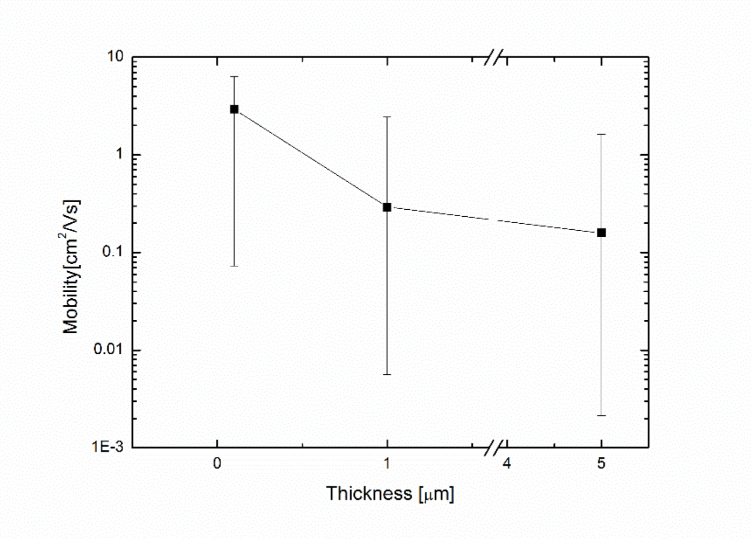

Figure 4.41 Mobility respect to thickness of only C film.

The film resistivity is correlated to carrier mobility and bulk concentration by the formula:

$$\rho = \frac{1}{Bulk\ conc. \times \mu \times q}$$

Where ρ is the resistivity, μ is the mobility and q is the electron charge. The resistivity results are a direct consequence of the previous factors.

At different Pt load, there is a resistivity in the magnitude of 1Ωcm, which is three magnitudes higher than FTO and Pt resistivity (about 10^{-4}Ωcm) and four than Pt bulk ($1.06 \cdot 10^{-6}$Ωcm[111]).

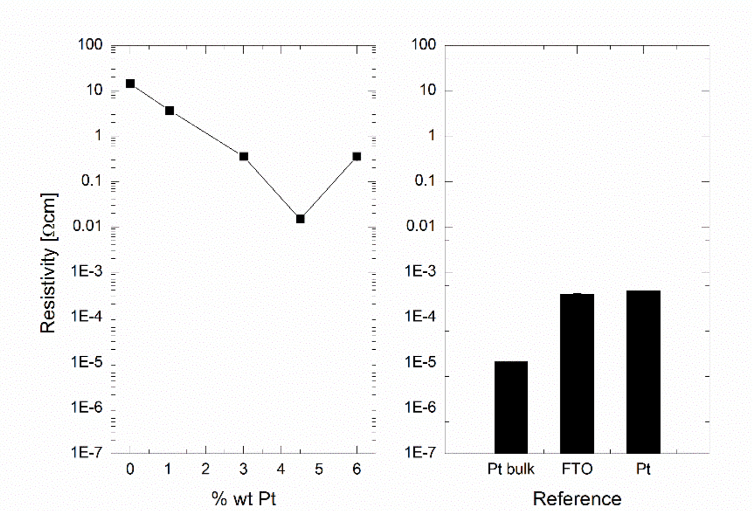

Figure 4.42 Left: Resistivity respect to the Pt percentage deposited in the film. Right: Resistivity for three references, FTO, Pt bulk and Pt sputtered with a thickness of 32nm

Also at different thicknesses, the resistivity has the same high values, sign that the carrier conductance into the film is affected by the disordered and porous nature of the film.

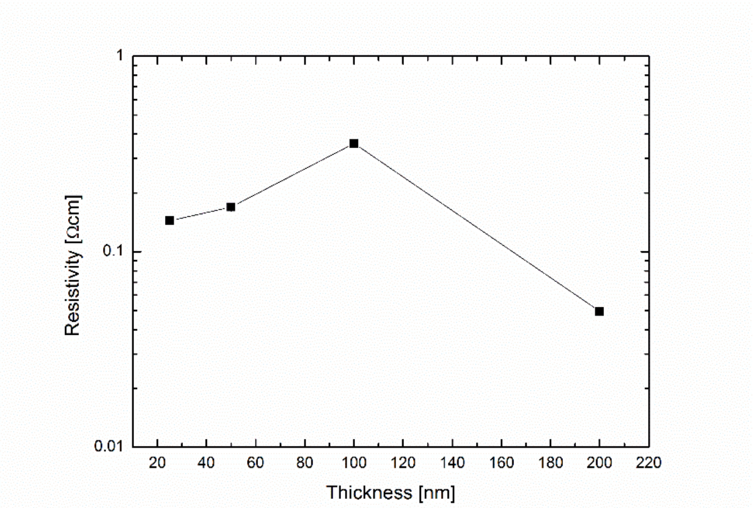

Figure 4.43 Resistivity respect to thickness of C-Pt film, with the same ratio Pt:C (3%wt)

In specimens with only carbon, the resistivity is really high (four order of magnitude higher than Pt), but we can observe a decreasing trend decreases with the thickness. This fact could be explain with a higher bulk concentration due to the greater thickness of film, as hypnotized before.

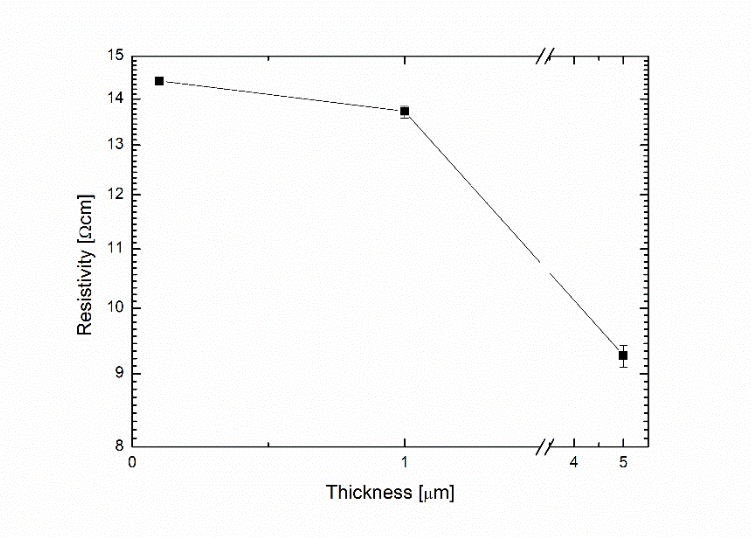

Figure 4.44 Resistivity respect to thickness of only C film.

Our measures are affected by quite high standard deviations. This fact is attributable to the quality of used instrument. The magnets used to perform the measure have a magnetic field of 0.5T, which is too low to allow a quick and good deviation of electron flux in a so porous material, where recombination processes are promoted by the high presence of defects in the crystalline structure.

To conclude this part, we can say that carbon platinum counter electrode does not show good performances as low resistance film due to its high porosity, but, at the same time, porosity is indispensable for the electrolyte percolation. Moreover, carbon platinum film are totally black. This is another problem to overcome, if the final aim is the production of monolithic DSSCs for building integrating photovoltaic.

4.3 Monolithic DSSC

After the study of different components of a DSSC (photo-anode and counter-electrode), I fabricated a device with Luca Passoni's collaboration.

4.3.1 Device Fabrication

FTO sheet was cut in rectangular pieces of 18 mm x 32mm. On the substrates a rectangular of 1mm x 1.8mm was etched, as was represented in Fig.4.45. This was done to divide the substrate in two different parts not in contact between them self that will be the two electrodes of the cell. After the etching step, samples were cleaned with the above descripted method.

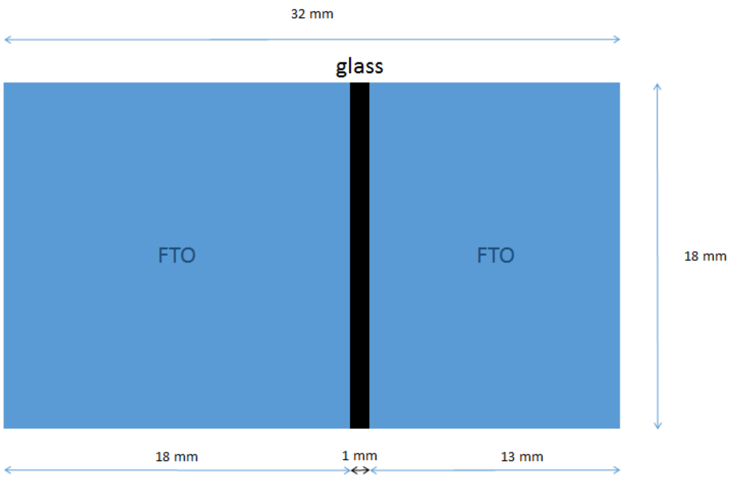

Figure 4.45 Schematic of the glass substrate after the etching treatment

The etched and cleaned samples were masked with Kapton tape, leaving a free area of 6mm x 6mm near to the etched part, as it is possible to see in Fig.4.46. TiO_2 film was deposited by PLD technique at 7Pa in oxygen with 105k pulses (about 5μm).

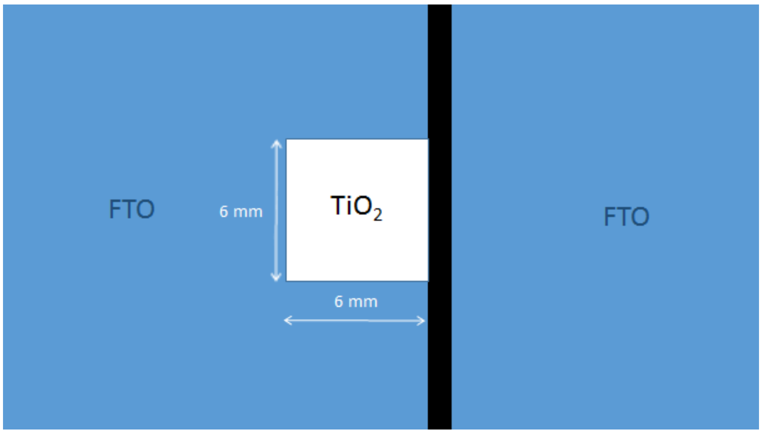

Figure 4.46 Schematic of the glass substrate after TiO_2 deposition.

The next step was the alumina deposition. Samples with TiO_2 were unmasked and subsequently re-masked leaving a free area of 8mm x 8mm that contained the TiO_2 film. Al_2O_3 was deposited at 30Pa in oxygen atmosphere with 36k pulses (about 3µm). In this way the alumina film cover completely the titania one (Fig.4.47).

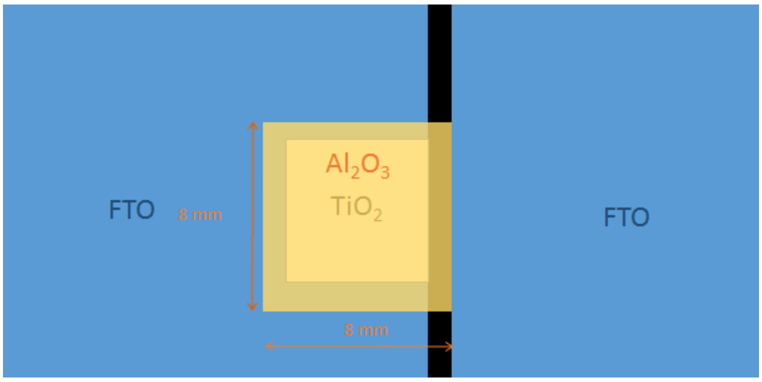

Figure 4.47 Schematic of the glass substrate after Al_2O_3 deposition.

After the alumina deposition and before the carbon-platinum one, the devices were annealed in a furnace at 500°C for 2hs. This process of annealing is necessary to achieve the crystalline transition in TiO_2 from amorphous form to the Anatase phase.

After the annealing process, samples were re-masked. The free area was 6mm x 10mm. The carbon platinum counter electrode was fabricated by a deposition of carbon by PLD and of platinum layer (~40nm) by magnetron sputtering. Film of carbon was deposited at 7Pa in argon atmosphere with 108k pulses. As we can see in Fig.4.48, part of C-Pt film must be deposited onto the alumina film. This because alumina has the role of insulator between TiO_2 and C-Pt film, avoiding a short circuit between them. C-Pt film extended onto the two electrodes and connected them.

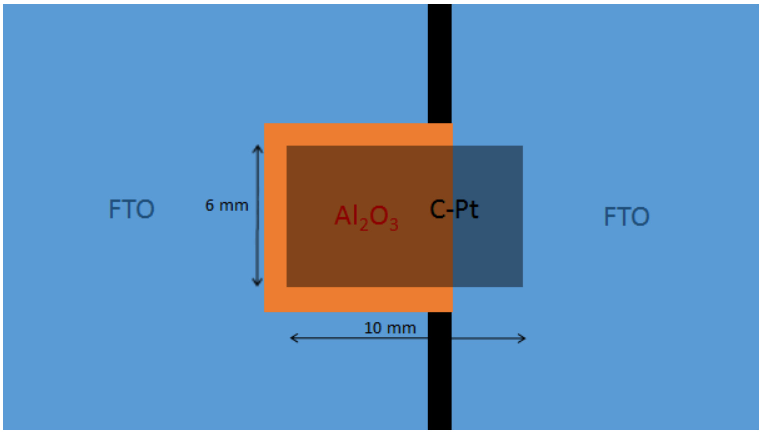

Figure 4.48 Schematic of the glass substrate after the C-Pt counter electrode deposition.

For all depositions, laser parameters and conditions were the same, derived by a previous meticulous study[95]: laser energy was 400mJ and repetition rate 20Hz. The deposition was performed in dynamic mode, by rotating the substrates holder continuously at 10rpm, to obtain a uniform deposition.

After the counter-electrode fabrication, the deposition process was finished and it was possible to begin with the second step of the cell fabrication.

Device underwent a dye loading process (Par.4.1.1). After dye loading process, devices must be encapsulated to avoid leakage of electrolyte. We used a piece of TPS 065093 – 30, a commercial thermoplastic sealant by DYESOL, cut as a frame round to the deposited films (Fig.4.49), as glue and , on top of the sealant layer, we cover with a plate of glass.

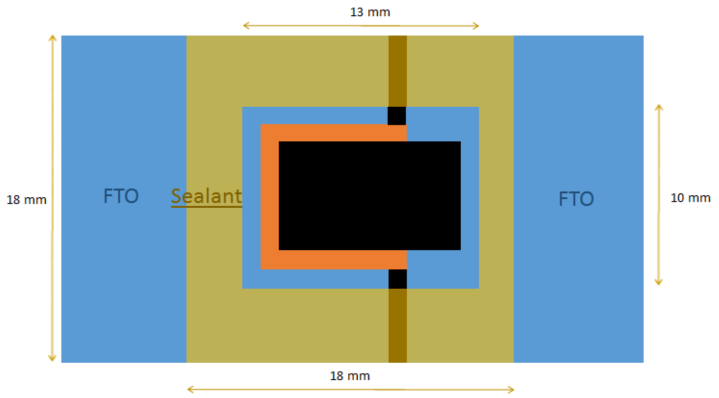

Figure 4.49 Schematic of the glass substrate after the sealing

Glass cover had an area 18mm x 18mm with a hole with 1.8mm of diameter in the centre (Fig.4.50). Device were pressed in a hot press at 130°C to melt the sealant and paste the two glass between them.

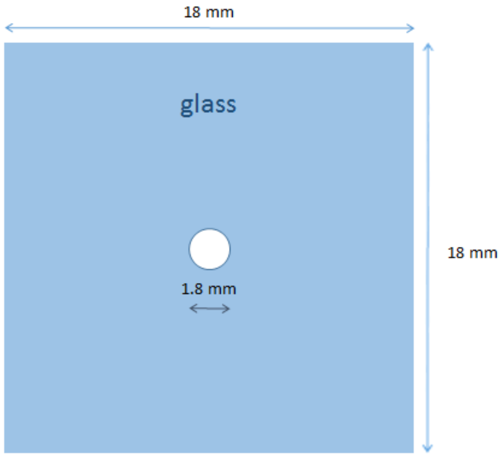

Figure 4.50 Schematic of the cover glass with central hole for electrolyte percolation

The hole in the cover glass was used to infiltrate the liquid electrolyte into the device. Electrolyte was a commercial iodide/triiodide based one by DYESOL (Electrolyte EL-HPE). To percolate into the devices, some drops were put into the hole in the cover glass and, then, with a pump, devices were taken in vacuum for about one minute. With electrolyte percolation, device assumed a yellow tinge. When all the area within the sealant was yellow, the electrolyte was homogeneously percolated in all different deposited films.

After the electrolyte infiltration, the hole in the cover glass was plugged with a piece of sealant ad a piece of aluminium foil, heated by a soldering iron.

The last step was to put two strips of commercial Ag paste at the two extremes of FTO substrate (Fig.4.51), to improve the electric contact for the device characterization.

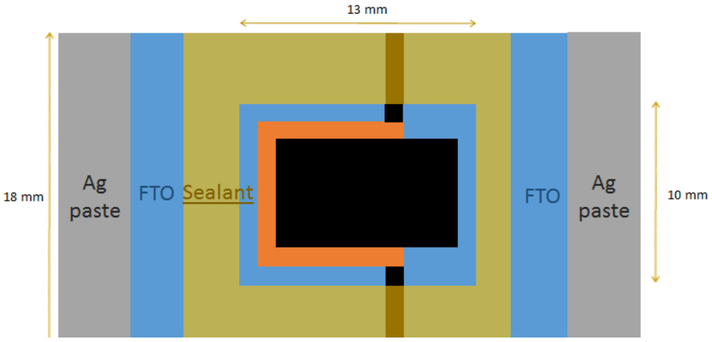

Figure 4.51 Schematic of the glass substrate after added Ag contacts.

Immediately after the electrolyte percolation and the sealing procedure, we performed the current-voltage characterization (Par.3.2.4) to avoid any possible leakage or corrosion by electrolyte.

4.3.2 Current-Voltage characterization of m-DSSC

With reference to Par.2.1, we showed in Fig.2.2 the J-V characteristic curve of a common photovoltaic device explaining the main parameters (short circuit current density, open circuit voltage, fill factor). DSSC can be modelled as current source in parallel with a diode (Fig.4.52).

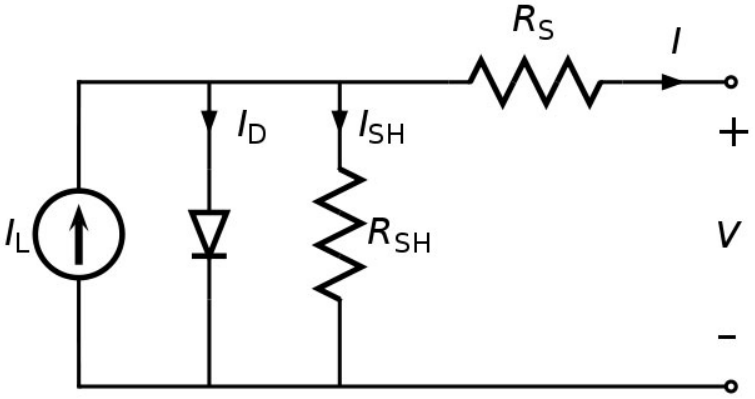

Figure 4.52 Example of an equivalent circuit used to analyse and improve the device.

When the device is not illuminated, current is not photogenerated and DSSC behaves as a diode. Increasing the incident light intensity, the device begins to generate a photocurrent corresponding to light intensity.

In an ideal system, I is the difference between the current generated by the device (I_L) and the diode current (I_D). R_S (series resistance) and R_{SH} (shunt resistance) are parasitic resistances and are respectively modelled as a series resistance and a parallel one. R_S is a sum of three elements:

$$R_s = R_1 + R_3 + R_h$$

Where R_1 is the resistance related to the charge-transfer process occurring at the counter electrode. It is inversely proportional to the counter electrode roughness factor. R_3 is related to the ion transport in the electrolyte and is affected by the transport distance and ion transport rate. R_h is the sheet resistance and is connected to resistance of counter electrode film.

R_{SH}, the shunt resistance, causes power losses by providing an alternate current path for the light-generated photo-current. It is due mainly to manufacturing defects[21].

Fig.4.53 shows how the shape of the J-V is affected by these two parasitic resistances.

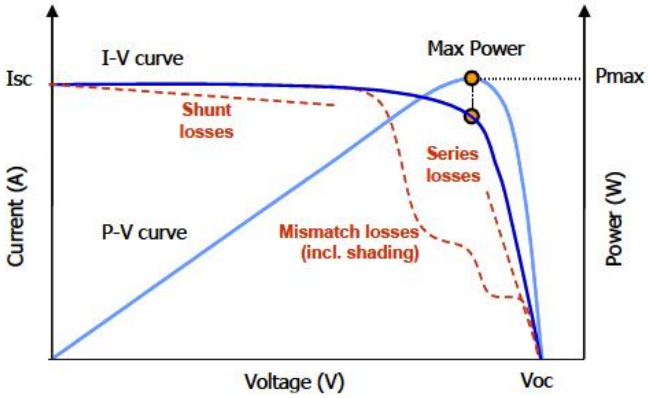

Figure 4.53 Current-Voltage and Power-Voltage characteristics of a common photovoltaic device. Dot lines indicate how the losses present in the device affect the performances.

R_{SH} affects the slope of J-V characteristic in correspondence of J_{SC}. When R_{SH} decreases, the curve tends to have a higher downwards slope, leading a lower value of V_{OC}. This behaviour is due to the fact that if, in an ideal case, R_{SH} would be infinite, the photogenerated current could not follow an alternative path and is totally conveyed to the photo-anode. Instead, in the case where R_S increases, the contribution of electrons at the counter electrode for the electrolyte reduction process is lower, this fact slows down the regeneration of the dye, with a consequent loss in the photocurrent generation.

After the previous characterization on the electrical properties of carbon platinum, we decided to deposit the counter electrode in two different ways. Both required the separation of carbon film from platinum layer, because a co-deposited C-Pt film with a thickness of 1μm was too expensive to deposit; moreover, the co-deposition did not ensure very good results in terms of resistivity on a thick film of carbon. The first configuration is shown in Fig.4.54.

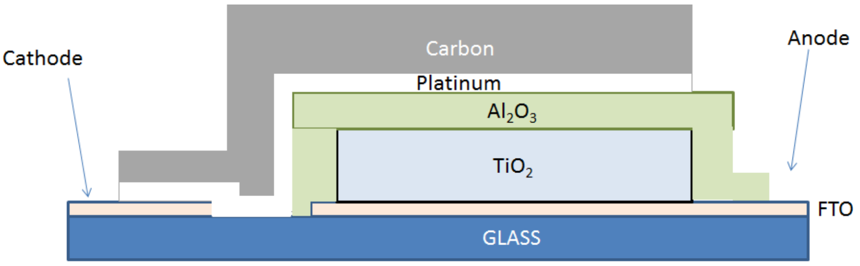

Figure 4.54 First configuration of our m-DSSC. Pt layer is sputtered on top of spacer. C layer is deposited on top of Pt.

We sputtered the layer of Pt directly on the Al_2O_3. In this way, triiodide, reduced at dye surface in the photo-anode, have to diffuse through a thinner path to arrive in contact with Pt.

The second configuration is shown in Fig.4.55.

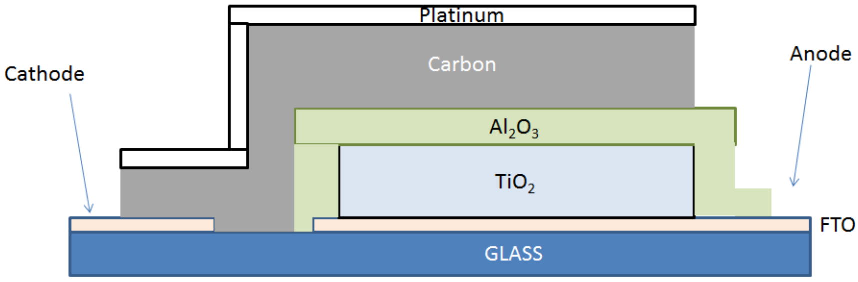

Figure 4.55 Second configuration of our m-DSSC. Pt layer is sputtered on top of C layer

In this case, we referred to Han et al. (2009)[102] and deposited the Pt layer as last layer, on top of carbon.

The comparison between the two J-V obtained characteristics is in Fig.4.56.

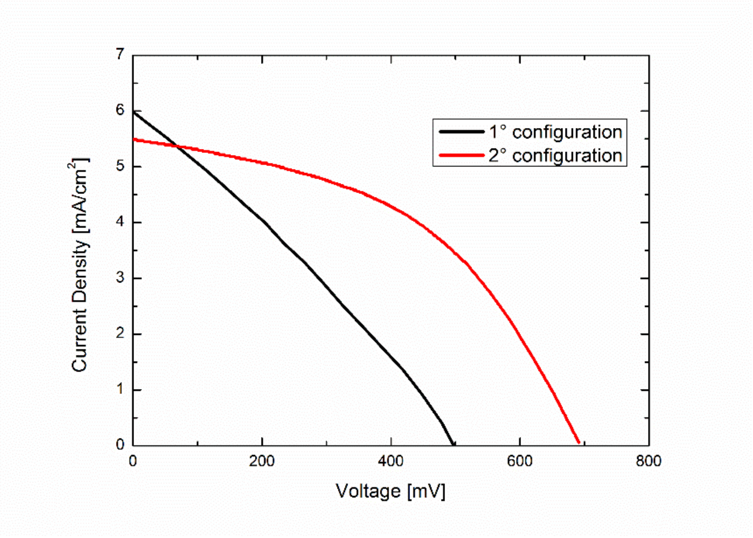

Figure 4.56 In red J-V curve of m-DSSC with Pt layer on top of Al_2O_3. In black: J-V curve of m-DSSC with Pt on top of C.

The shape of J-V characteristic of device with the first configuration shows a behaviour similar to a resistor. The slope of the curve is really high. The device with the second configuration, instead, has the shape of a diode. The fact that the first device has this shape could be due to the presence of short circuit between anode and cathode. In this case, the Al_2O_3 was so porous that Pt deposited nanoparticles were penetrated and were in contact with TiO_2. The fact to have deposited the Pt layer on top of the carbon film prevented the infiltration of Pt nanoparticles in the spacer.

In Fig.4.57 a comparison between our, Petterson's[112] and Liu's devices is shown.

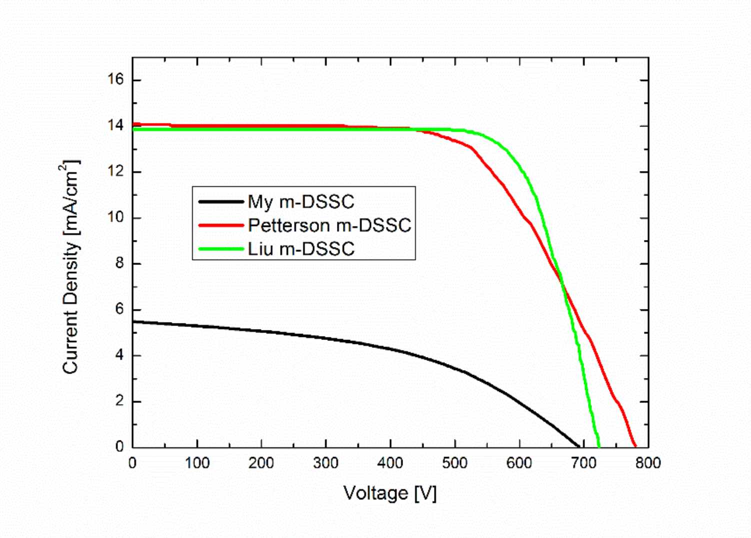

Figure 4.57 In black: J-V curve of my m-DSSC fabricated with 2° configuration. In red: J-V curve of Petterson's m-DSSC. In green: J-V curve of Liu's m-DSSC.

In Tab.4.7 are summarized the main parameters for each device.

Table 4.7 V_{oc}, J_{sc}, FF and PCE values of the two devices fabricated my us (1° and 2° configuration), Petterson's m-DSSC and Liu's m-DSSC

Sample	V_{OC} [mV]	J_{SC} [mA/cm^2]	Fill Factor [%]	PCE [%]
1° configuration	490	5.99	29.4	0.79
2° configuration	693	5.49	46.9	1.93
Pettersson's m-DSSC	780	14.1	62	6.8
Liu's m-DSSC	723	13.89	76	7.61

Keeping out the Liu's device, that I insert because is the most efficient m-DSSC in literature but was fabricated with totally different materials respect to ours (i.e. polyethylene as separator and PEDOT as counter electrode), we can confront the J-V curve of our device with that one of Pettersson's.

The shape of the two curve presents some difference, which can be explained in the light of the analysis previously made. The higher downwards slope in correspondence of J_{SC} could be due to what observed in Par.4.1.2, the holes left by detaching of droplets could be lead the deposition of carbon platinum in contact with TiO_2, creating a short circuit. In this way, the R_{SH} has a low value and J-V characteristic is affected negatively.

Moreover, in Par.4.2.4 I characterized the carbon platinum counter electrode observing that its resistance is very high respect to an only Pt counter electrode. This fact affects negatively J-V curve, because R_S is high.

The main parameter affected by these defects is the Fill factor. Values of J_{SC} and V_{OC} are comparable with that of Han's device. The FF, instead, is about the half, this because the defects affect the slope of the J-V curve, decreasing the FF and then the efficiency.

In order to a correct comparison, we have to take in account the differences there are in the active areas and in layer thicknesses.

We have a TiO_2 active area of 0.36cm^2 while in Petterson's device is 0.48cm^2. This means that there is more material to harvest the light and photo-generate current. Moreover, from Par.4.3.1, we deposited 5µm of TiO_2, 3µm of Al_2O_3, 1µm of carbon a about 40nm of platinum. Petterson fabricated his device depositing 12µm of TiO_2, 10µm of ZrO_2 (it has the same Al_2O_3 insulator properties), 10µm of carbon and 50µm of carbon loaded with platinum. The fact to have a photo-anode more than double of our, leads to enhance the light management and increase the quantity of chemisorbed dye, with an improvement in photocurrent generation. The presence of a spacer very thick respect that one in our case avoids the contact between photo-anode and counter electrode. Finally, the counter electrode is twenty times bigger than ours. As shown in Par.4.2.4, increasing the thickness of the carbon layer, the resistivity decreases and the presence of Pt decreases further the sheet resistance.

This fact to have a very thick specimen was impossible to reproduce for us, because the thick of sealant that we used is of about 25µm. We can not fabricate a device that overall is thicker than the sealant otherwise it can not be encapsulated.

5 Conclusions and Outlooks

In conclusion, the TiO_2 photo-anode, deposited by PLD with a tree-like morphology, undergoes a positive influence with the presence of the Al_2O_3 porous spacer on the top. The Haze factor increases of about 15% on all visible spectrum, this fact means a higher quantity of scattering phenomena and a better light trapping. This enhancement of optical properties and light management leads to an increasing of maximum expected photocurrent of about 20%. Having a high theoretical I_{SC} value is a good starting point for improving the DSSC efficiency, working to increase the shunt losses in order to achieve an I_{SC} value equal to the theoretical one.

Regarding to TiO_2 deposition by PA-SSJD, the reactor is a prototype yet. The first results are encouraging. The obtained tree-like morphology is similar to that by PLD and this is the point from which to start to implement this new deposition technique and to lead a scale-up the DSSC fabrication on large area and with low deposition time.

With reference to the optimization of Pt load in the counter electrode, I obtain that increasing percentage in weight of Pt respect to C, the resistivity does not decrease. On the contrary, a higher thickness of one only carbon layer has a lower sheet resistance.

Finally, I fabricated a functioning monolithic DSSC with a Power Conversion Efficiency of 1.93%, which is a good result to be the first time that I try to fabricate a device after the previous characterization of the different components.

For further investigations on this type of m-DSSC, the improvement of PA-SSJD to deposit TiO_2 film without the presence of droplets could lead to avoid the presence of short circuit between the photo-anode and the counter electrode. In this way, the shunt resistance could be increased, with an enhancement in the performance. In addition to improve the deposition quality, a solution could be to deposit a thicker Al_2O_3, in this way, the probabilities that carbon or platinum nanoparticle could infiltrate through the spacer porosity up to the photo-anode decrease. Regarding to the counter electrode, the next step will be trying to substitute carbon with a porous Transparent Conductive Oxide (an idea is ITO) in order to have a semi-transparent device. This fact would lead to fabricate devices with different colours, depending on the dye sensitizer used, in order to integrate the DSSCs in build facades. After a complete optimization of m-

DSSC fabrication process on flat substrate, the last step is to transpose this process on a solar concentrator, in order to enhance the light management when the device is integrated in a façade in a vertical position. This action requires further analysis to which shape of the substrate affects the deposition process and the properties of different parts. Once the process of characterization and optimization is over, the m-DSSC will be tested as Building Integrated Photovoltaics.

Bibliography

1. Anderson, K. and A. Bows, *Beyond 'dangerous' climate change: emission scenarios for a new world.* Philosophical Transactions of the Royal Society A: Mathematical, Physical and Engineering Sciences, 2011. **369**(1934): p. 20-44.
2. Oreskes, N., *The Scientific Consensus on Climate Change.* Science, 2004. **306**(5702): p. 1686.
3. Stern, N. and G.B. Treasury, *The Economics of Climate Change: The Stern Review*2007: Cambridge University Press.
4. Green, M.A., et al., *Solar cell efficiency tables (version 43).* Progress in Photovoltaics: Research and Applications, 2014. **22**(1): p. 1-9.
5. Zhang, Q. and G. Cao, *Nanostructured photoelectrodes for dye-sensitized solar cells.* Nano Today, 2011. **6**(1): p. 91-109.
6. Badawy, W.A., *A review on solar cells from Si-single crystals to porous materials and quantum dots.* Journal of Advanced Research, (0).
7. Li, G., et al., *High-efficiency solution processable polymer photovoltaic cells by self-organization of polymer blends.* Nat. Mater., 2005. **4**(11): p. 864-868.
8. Jeong, S., et al., *An 8.2% efficient solution-processed CuInSe2 solar cell based on multiphase CuInSe2 nanoparticles.* Energy & Environmental Science, 2012. **5**(6): p. 7539-7542.
9. Katagiri, H., et al., *Development of CZTS-based thin film solar cells.* Thin Solid Films, 2009. **517**(7): p. 2455-2460.
10. Krishnamoorthy, T., et al., *A first report on the fabrication of vertically aligned anatase TiO2 nanowires by electrospinning: Preferred architecture for nanostructured solar cells.* Energy & Environmental Science, 2011. **4**: p. 2807-2812.
11. O'Regan, B. and M. Gratzel, *A low-cost, high-efficiency solar cell based on dye-sensitized colloidal TiO2 films.* Nature, 1991. **353**(6346): p. 737-740.
12. Butler, D., *Thin Films: Ready for Their Close-Up?* Nature, 2008. **454**: p. 558-559.
13. Hug, H., et al., *Biophotovoltaics: Natural pigments in dye-sensitized solar cells.* Applied Energy, 2014. **115**(0): p. 216-225.
14. Hardin, B.E., H.J. Snaith, and M.D. McGehee, *The renaissance of dye-sensitized solar cells.* Nature, 2012. **6**(3): p. 162-169.
15. Yella, A., et al., *Porphyrin-Sensitized Solar Cells with Cobalt (II/III)–Based Redox Electrolyte Exceed 12 Percent Efficiency.* Science, 2011. **334**(6056): p. 629-634.
16. Mathew, S., et al., *Dye-sensitized solar cells with 13% efficiency achieved through the molecular engineering of porphyrin sensitizers.* Nat Chem, 2014. **6**(3): p. 242-247.
17. Stefanović, A., M. Bojić, and D. Gordić, *Achieving net zero energy cost house from old thermally non-insulated house using photovoltaic panels.* Energy and Buildings, 2014. **76**(0): p. 57-63.
18. Zogou, O. and H. Stapountzis, *Experimental validation of an improved concept of building integrated photovoltaic panels.* Renewable Energy, 2011. **36**(12): p. 3488-3498.
19. Yoon, S., et al., *Application of transparent dye-sensitized solar cells to building integrated photovoltaic systems.* Building and Environment, 2011. **46**(10): p. 1899-1904.
20. Hassaine, L., et al., *Overview of power inverter topologies and control structures for grid connected photovoltaic systems.* Renewable and Sustainable Energy Reviews, 2014. **30**(0): p. 796-807.
21. Zhang, S., et al., *Highly efficient dye-sensitized solar cells: progress and future challenges.* Energy & Environmental Science, 2013. **6**(5): p. 1443-1464.
22. Liang, W.Y., *Excitons.* Physics Education, 1970. **5**(4): p. 226.
23. Ardo, S. and G.J. Meyer, *Photodriven heterogeneous charge transfer with transition-metal compounds anchored to TiO2 semiconductor surfaces.* Chemical Society Reviews, 2009. **38**(1): p. 115-164.
24. Hagfeldt, A., et al., *Dye-Sensitized Solar Cells.* Chemical Reviews, 2010. **110**(11): p. 6595-6663.
25. Hagfeldt, A. and M. Graetzel, *Light-Induced Redox Reactions in Nanocrystalline Systems.* Chemical Reviews, 1995. **95**(1): p. 49-68.
26. Wang, M., et al., *The Influence of Charge Transport and Recombination on the Performance of Dye-Sensitized Solar Cells.* ChemPhysChem, 2009. **10**(1): p. 290-299.

27. Haque, S.A., et al., *Charge Separation versus Recombination in Dye-Sensitized Nanocrystalline Solar Cells: the Minimization of Kinetic Redundancy.* Journal of the American Chemical Society, 2005. **127**(10): p. 3456-3462.
28. Oekermann, T., et al., *Electron Transport and Back Reaction in Nanocrystalline TiO2 Films Prepared by Hydrothermal Crystallization.* The Journal of Physical Chemistry B, 2004. **108**(7): p. 2227-2235.
29. Tang, H., et al., *Electrical and optical properties of TiO2 anatase thin films.* Journal of Applied Physics, 1994. **75**(4): p. 2042-2047.
30. De Angelis, F., et al., *Absorption Spectra and Excited State Energy Levels of the N719 Dye on TiO2 in Dye-Sensitized Solar Cell Models.* The Journal of Physical Chemistry C, 2011. **115**(17): p. 8825-8831.
31. By Sharayanan (Own work) [GFDL (http://www.gnu.org/copyleft/fdl.html), C.-B.-S.-h.c.o.l.b.-s. 2007 [cited 2014 30/08/2014]; Depiction of Mie scattering on a spheric particle. The graph roughly displays scattering intensity per direction. From left to right : Rayleigh, intermediate and full Mie scattering]. Available from: http://commons.wikimedia.org/wiki/File%3AMie_scattering.svg.
32. Benkstein, K.D., et al., *Influence of the Percolation Network Geometry on Electron Transport in Dye-Sensitized Titanium Dioxide Solar Cells.* The Journal of Physical Chemistry B, 2003. **107**(31): p. 7759-7767.
33. Monthioux, M. and V.L. Kuznetsov, *Who should be given the credit for the discovery of carbon nanotubes?* Carbon, 2006. **44**(9): p. 1621-1623.
34. Kim, D., et al., *Bamboo-Type TiO2 Nanotubes: Improved Conversion Efficiency in Dye-Sensitized Solar Cells.* Journal of the American Chemical Society, 2008. **130**(49): p. 16454-16455.
35. Cao, Y., et al., *Dye-Sensitized Solar Cells with a High Absorptivity Ruthenium Sensitizer Featuring a 2-(Hexylthio)thiophene Conjugated Bipyridine.* The Journal of Physical Chemistry C, 2009. **113**(15): p. 6290-6297.
36. Law, M., et al., *Nanowire dye-sensitized solar cells.* Nat Mater, 2005. **4**(6): p. 455-459.
37. Feng, X., et al., *Vertically Aligned Single Crystal TiO2 Nanowire Arrays Grown Directly on Transparent Conducting Oxide Coated Glass: Synthesis Details and Applications.* Nano Letters, 2008. **8**(11): p. 3781-3786.
38. Kim, Y.J., et al., *Formation of Highly Efficient Dye-Sensitized Solar Cells by Hierarchical Pore Generation with Nanoporous TiO2 Spheres.* Advanced Materials, 2009. **21**(36): p. 3668-3673.
39. Handoko, A.D., K. Li, and J. Tang, *Recent progress in artificial photosynthesis: CO2 photoreduction to valuable chemicals in a heterogeneous system.* Current Opinion in Chemical Engineering, 2013. **2**(2): p. 200-206.
40. Sauvage, F., et al., *Hierarchical TiO2 Photo-anode for Dye-Sensitized Solar Cells.* Nano Letters, 2010. **10**(7): p. 2562-2567.
41. Fleming III, P.D. *The Gravure Doctor Blade*. 2012 [cited 2014 2014/05/05]; Available from: http://www.wmich.edu/pci/gravure/pp9.htm.
42. Kim, G.-S., et al., *Electrophoretic deposition of titanate nanotubes from commercial titania nanoparticles: Application to dye-sensitized solar cells.* Electrochemistry Communications, 2006. **8**(6): p. 961-966.
43. Kontos, A.I., et al., *Nanostructured TiO2 films for DSSCS prepared by combining doctor-blade and sol–gel techniques.* Journal of Materials Processing Technology, 2008. **196**(1–3): p. 243-248.
44. Corporation, T.R.I. *Hydrothermal Growth*. 10/05/2014]; Available from: http://www.roditi.com/SingleCrystal/Quartz/Hydrothermal_Growth.html.
45. Wang, P., et al., *Enhance the Performance of Dye-Sensitized Solar Cells by Co-grafting Amphiphilic Sensitizer and Hexadecylmalonic Acid on TiO2 Nanocrystals.* The Journal of Physical Chemistry B, 2003. **107**(51): p. 14336-14341.
46. Zhang, G., et al., *High efficiency and stable dye-sensitized solar cells with an organic chromophore featuring a binary [small pi]-conjugated spacer.* Chemical Communications, 2009(16): p. 2198-2200.
47. Chang, H., et al., *Photoelectrode thin film of dye-sensitized solar cell fabricated by anodizing method and spin coating and electrochemical impedance properties of DSSC.* Applied Surface Science, 2013. **275**(0): p. 252-257.

48. Lin, L.-Y., et al., *Highly ordered TiO2 nanotube stamps on Ti foils: Synthesis and application for all flexible dye–sensitized solar cells.* Electrochemistry Communications, 2013. **37**(0): p. 71-75.
49. Ping Wu, H., et al., *Anodic TiO2 Nanotube Arrays for Dye-Sensitized Solar Cells Characterized by Electrochemical Impedance Spectroscopy.* Ceramics International, 2012. **38**(8): p. 6253-6266.
50. Zwilling, V., M. Aucouturier, and E. Darque-Ceretti, *Anodic oxidation of titanium and TA6V alloy in chromic media. An electrochemical approach.* Electrochimica Acta, 1999. **45**(6): p. 921-929.
51. Sreekantan, S., et al., *Fast-rate formation of TiO 2 nanotube arrays in an organic bath and their applications in photocatalysis.* Nanotechnology, 2010. **21**(36): p. 365603.
52. Durr, M., et al., *Low-temperature fabrication of dye-sensitized solar cells by transfer of composite porous layers.* Nat Mater, 2005. **4**(8): p. 607-611.
53. Yang, C.-C., H.Q. Zhang, and Y.R. Zheng, *DSSC with a novel Pt counter electrodes using pulsed electroplating techniques.* Current Applied Physics, 2011. **11**(1, Supplement): p. S147-S153.
54. Hauch, A. and A. Georg, *Diffusion in the electrolyte and charge-transfer reaction at the platinum electrode in dye-sensitized solar cells.* Electrochimica Acta, 2001. **46**(22): p. 3457-3466.
55. Li, P., et al., *High-performance and low platinum loading Pt/Carbon black counter electrode for dye-sensitized solar cells.* Solar Energy, 2009. **83**(6): p. 845-849.
56. Giribabu, L., R.K. Kanaparthi, and V. Velkannan, *Molecular engineering of sensitizers for dye-sensitized solar cell applications.* The Chemical Record, 2012. **12**(3): p. 306-328.
57. Barolo, C., et al., *Synthesis, Characterization, and DFT-TDDFT Computational Study of a Ruthenium Complex Containing a Functionalized Tetradentate Ligand.* Inorganic Chemistry, 2006. **45**(12): p. 4642-4653.
58. Nazeeruddin, M.K., et al., *DFT-INDO/S Modeling of New High Molar Extinction Coefficient Charge-Transfer Sensitizers for Solar Cell Applications.* Inorganic Chemistry, 2005. **45**(2): p. 787-797.
59. Wu, K.-L., et al., *Engineering of Osmium(II)-Based Light Absorbers for Dye-Sensitized Solar Cells.* Angewandte Chemie International Edition, 2012. **51**(23): p. 5642-5646.
60. Bessho, T., et al., *New Paradigm in Molecular Engineering of Sensitizers for Solar Cell Applications.* Journal of the American Chemical Society, 2009. **131**(16): p. 5930-5934.
61. Kim, B.-G., et al., *Organic Dye Design Tools for Efficient Photocurrent Generation in Dye-Sensitized Solar Cells: Exciton Binding Energy and Electron Acceptors.* Advanced Functional Materials, 2012. **22**(8): p. 1606-1612.
62. Wamser, C.C., M.G. Walter, and A.B. Rudine, *Porphyrins and phthalocyanines in solar photovoltaic cells.* Journal of Porphyrins and Phthalocyanines, 2010. **14**(09): p. 759-792.
63. Li, L.-L. and E.W.-G. Diau, *Porphyrin-sensitized solar cells.* Chemical Society Reviews, 2013. **42**(1): p. 291-304.
64. Chiba, Y., et al., *Dye-Sensitized Solar Cells with Conversion Efficiency of 11.1%.* Japanese Journal of Applied Physics, 2006. **45**(7L): p. L638.
65. Boschloo, G. and A. Hagfeldt, *Characteristics of the Iodide/Triiodide Redox Mediator in Dye-Sensitized Solar Cells.* Accounts of Chemical Research, 2009. **42**(11): p. 1819-1826.
66. Clifford, J.N., et al., *Dye Dependent Regeneration Dynamics in Dye Sensitized Nanocrystalline Solar Cells: Evidence for the Formation of a Ruthenium Bipyridyl Cation/Iodide Intermediate.* The Journal of Physical Chemistry C, 2007. **111**(17): p. 6561-6567.
67. Yanagida, S., Y. Yu, and K. Manseki, *Iodine/Iodide-Free Dye-Sensitized Solar Cells.* Accounts of Chemical Research, 2009. **42**(11): p. 1827-1838.
68. Cong, J., et al., *Iodine/iodide-free redox shuttles for liquid electrolyte-based dye-sensitized solar cells.* Energy & Environmental Science, 2012. **5**(11): p. 9180-9194.
69. Nusbaumer, H., et al., *CoII(dbbip)22+ Complex Rivals Tri-iodide/Iodide Redox Mediator in Dye-Sensitized Photovoltaic Cells.* The Journal of Physical Chemistry B, 2001. **105**(43): p. 10461-10464.
70. Yum, J.-H., et al., *A cobalt complex redox shuttle for dye-sensitized solar cells with high open-circuit potentials.* Nat Commun, 2012. **3**(631).
71. Chung, I., et al., *All-solid-state dye-sensitized solar cells with high efficiency.* Nature, 2012. **485**(7399): p. 486-489.

72. Ding, I.K., et al., *Pore-Filling of Spiro-OMeTAD in Solid-State Dye Sensitized Solar Cells: Quantification, Mechanism, and Consequences for Device Performance.* Advanced Functional Materials, 2009. **19**(15): p. 2431-2436.

73. Schmidt-Mende, L., S.M. Zakeeruddin, and M. Grätzel, *Efficiency improvement in solid-state-dye-sensitized photovoltaics with an amphiphilic Ruthenium-dye.* Applied Physics Letters, 2005. **86**(1): p. -.

74. Roh, D.K., et al., *High Efficiency Solid-State Dye-Sensitized Solar Cells Assembled with Hierarchical Anatase Pine Tree-like TiO2 Nanotubes.* Advanced Functional Materials, 2014. **24**(3): p. 379-386.

75. Passoni, L., et al., *Hyperbranched Quasi-1D Nanostructures for Solid-State Dye-Sensitized Solar Cells.* ACS Nano, 2013. **7**(11): p. 10023-10031.

76. Ahn, S.H., et al., *Direct Assembly of Preformed Nanoparticles and Graft Copolymer for the Fabrication of Micrometer-thick, Organized TiO2 Films: High Efficiency Solid-state Dye-sensitized Solar Cells.* Advanced Materials, 2012. **24**(4): p. 519-522.

77. Cao, F., G. Oskam, and P.C. Searson, *A Solid State, Dye Sensitized Photoelectrochemical Cell.* The Journal of Physical Chemistry, 1995. **99**(47): p. 17071-17073.

78. Hench, L.L. and J.K. West, *The sol-gel process.* Chemical Reviews, 1990. **90**(1): p. 33-72.

79. Bandara, T.M.W.J., et al., *Quasi solid state polymer electrolyte with binary iodide salts for photo-electrochemical solar cells.* International Journal of Hydrogen Energy, 2014. **39**(6): p. 2997-3004.

80. Sathiya Priya, A.R., et al., *High-Performance Quasi-Solid-State Dye-Sensitized Solar Cell Based on an Electrospun PVdF–HFP Membrane Electrolyte.* Langmuir, 2008. **24**(17): p. 9816-9819.

81. Lee, K.-M., V. Suryanarayanan, and K.-C. Ho, *High efficiency quasi-solid-state dye-sensitized solar cell based on polyvinyidene fluoride-co-hexafluoro propylene containing propylene carbonate and acetonitrile as plasticizers.* Science, 2009. **207**(2-3): p. 224-230.

82. Ileperuma, O.A., et al., *Quasi-solid electrolyte based on polyacrylonitrile for dye-sensitized solar cells.* Journal of Photochemistry and Photobiology A: Chemistry, 2011. **217**(2–3): p. 308-312.

83. Kay, A. and M. Grätzel, *Low cost photovoltaic modules based on dye sensitized nanocrystalline titanium dioxide and carbon powder.* Solar Energy Materials and Solar Cells, 1996. **44**(1): p. 99-117.

84. Pettersson, H., et al., *Manufacturing method for monolithic dye-sensitised solar cells permitting long-term stable low-power modules.* Solar Energy Materials and Solar Cells, 2003. **77**(4): p. 405-413.

85. Liu, G., et al., *A mesoscopic platinized graphite/carbon black counter electrode for a highly efficient monolithic dye-sensitized solar cell.* Electrochimica Acta, 2012. **69**(0): p. 334-339.

86. Bräuer, G., et al., *Magnetron sputtering – Milestones of 30 years.* Vacuum, 2010. **84**(12): p. 1354-1359.

87. Sigmund, P., *Mechanisms and theory of physical sputtering by particle impact.* Nuclear Instruments and Methods in Physics Research Section B: Beam Interactions with Materials and Atoms, 1987. **27**(1): p. 1-20.

88. Sheridan, T.E., M.J. Goeckner, and J. Goree, *Pressure dependence of ionization efficiency in sputtering magnetrons.* Applied Physics Letters, 1990. **57**(20): p. 2080-2082.

89. Kang, S.H., et al., *Columnar rutile TiO2 based dye-sensitized solar cells by radio-frequency magnetron sputtering.* Journal of Power Sources, 2008. **184**(1): p. 331-335.

90. Meng, L., T. Ren, and C. Li, *The control of the diameter of the nanorods prepared by dc reactive magnetron sputtering and the applications for DSSC.* Applied Surface Science, 2010. **256**(11): p. 3676-3682.

91. Gómez, M., et al., *Nanocrystalline Ti-oxide-based solar cells made by sputter deposition and dye sensitization: Efficiency versus film thickness.* Solar Energy Materials and Solar Cells, 2000. **62**(3): p. 259-263.

92. Abdullah, M.H. and M. Rusop, *Improved performance of dye-sensitized solar cell with a specially tailored TiO2 compact layer prepared by RF magnetron sputtering.* Journal of Alloys and Compounds, 2014. **600**(0): p. 60-66.

93. Smith, H.M. and A.F. Turner, *Vacuum Deposited Thin Films Using a Ruby Laser.* Applied Optics, 1965. **4**(1): p. 147-148.

94. Ohnishi, T., et al., *Defects and transport in complex oxide thin films.* Journal of Applied Physics, 2008. **103**(10): p. -.
95. Fonzo, F.D., et al., *Hierarchically organized nanostructured TiO 2 for photocatalysis applications.* Nanotechnology, 2009. **20**(1): p. 015604.
96. Yang, W. and C.A. Wolden, *Plasma-enhanced chemical vapor deposition of TiO2 thin films for dielectric applications.* Thin Solid Films, 2006. **515**(4): p. 1708-1713.
97. Fantz, U., *Basics of plasma spectroscopy.* Plasma Sources Science and Technology, 2006. **15**(4): p. S137.
98. Briganzoli, I., et al., *A Supersonic Plasma Jet Source for Controlled and Efficient Thin Film Deposition.* Journal of Modern Physics, 2012. **3**(10A): p. 1626-1638.
99. Atteberry, J. *How Scanning Electron Microscopes Work*. 2009 [cited 2014 10/08/2014]; Available from: http://science.howstuffworks.com/scanning-electron-microscope.htm.
100. Georgiev, G.T. and J.J. Butler, *Long-term calibration monitoring of Spectralon diffusers BRDF in the air-ultraviolet.* Applied Optics, 2007. **46**(32): p. 7892-7899.
101. Taylor, J.L. *Design Considerations of Small (60 mm) Vs. Large (150 mm) Integrating Spheres*. 2010 11/08/2014]; Available from: www.pe.taylorjl.net/PE_Blog/?p=303.
102. Han, H., et al., *A design for monolithic all-solid-state dye-sensitized solar cells with a platinized carbon counterelectrode.* Applied Physics Letters, 2009. **94**(10): p. -.
103. Pettersson, H., et al., *Parallel-connected monolithic dye-sensitised solar modules.* Progress in Photovoltaics: Research and Applications, 2010. **18**(5): p. 340-345.
104. Tu, W.-K., et al., *A novel nanocomposite TiO2 photo-anode for highly efficient dye-sensitized solar cells.* Journal of Power Sources, 2012. **203**(0): p. 297-301.
105. Yue, G., et al., *Platinum/graphene hybrid film as a counter electrode for dye-sensitized solar cells.* Electrochimica Acta, 2013. **92**(0): p. 64-70.
106. Kerr, T. *Raman Spectroscopy applications in Materials Science Parts II*. 2012 [cited 2014 02/09/2014]; Available from: http://matsci4uwi.wordpress.com/2012/11/06/raman-spectroscopy-applications-in-materials-science-part-ii/.
107. Gupta, S. and A. Saxena, *Nanocarbon materials: probing the curvature and topology effects using phonon spectra.* Journal of Raman Spectroscopy, 2009. **40**(9): p. 1127-1137.
108. Rebollo-Plata, B., et al. *Amorphous Carbon Thin Films Prepared by Electron-Gun Evaporation*. AZojomo, 2005. **1**, DOI: 10.2240/azojomo0157.
109. Hong, S.S., et al., *Ultra-low carrier concentration and surface-dominant transport in antimony-doped Bi2Se3 topological insulator nanoribbons.* Nat Commun, 2012. **3**: p. 757.
110. Edwards, P.P., et al., *Basic materials physics of transparent conducting oxides.* Dalton Transactions, 2004(19): p. 2995-3002.
111. Helmenstine, A.M. *Table of Electrical Resistivity and Conductivity*. [cited 2014 06/09/2014]; Available from: http://chemistry.about.com/od/moleculescompounds/a/Table-Of-Electrical-Resistivity-And-Conductivity.htm.
112. Pettersson, H., et al., *The monolithic multicell: a tool for testing material components in dye-sensitized solar cells.* Prog. Photovolt: Res. Appl., 2007. **15**(2): p. 113-121.